DISSERTATION

APPLICATIONS OF INORGANIC NANOPARTICLES IN BIOLOGICAL ELECTRON MICROSCOPY

Submitted by

Thomas Wentung Ni

Department of Chemistry

In partial fulfillment of the requirements

For the Degree of Doctor of Philosophy

Colorado State University

Fort Collins, Colorado

Spring 2016

Doctoral Committee:

Advisor: Christopher Ackerson

Amy Prieto
Richard Finke
Olve Peersen

ABSTRACT

APPLICATIONS OF INORGANIC NANOPARTICLES IN BIOLOGICAL ELECTRON MICROSCOPY

Electron microscopy is an immensely powerful for imaging at the cellular level. However, many of the macromolecules of interest are difficult to image due to low electron density. There has been an immense body of work in order to visualize these macromolecules. In the past, many of the methods of visualization revolved around staining samples with heavy metals, however these stains are non-specific. In order to develop more specific methods of tagging macromolecules, there are two different methods to consider: the first being a top-down approach, in which electron dense tags, in this case inorganic nanoparticles, are given specific ligands to take advantage of different chemistries to attach these nanoparticles to macromolecules of interest. The second method is through a bottom-up approach where biomolecules are given the specific ability to form inorganic nanoparticles.

Inorganic nanoparticles have been investigated with various ligands in order to enhance binding capability to macromolecules. The chief method of functionalizing these inorganic nanoparticles comes from ligand exchange; much has been studied regarding ligand exchange, but there are still many unanswered questions. Herein, we endeavor to reveal both the mechanism of exchange and the functional unit of exchange.

We also report progress towards understanding an enzyme that is capable of forming inorganic nanoparticles, which could be cloned onto proteins as well. This bottom up style has been studied in several other groups; however, none of the previously reported methods have

seen much use. Herein, we report a potential NADPH-dependent enzyme that forms selenium nanoparticles.

ACKNOWLEDGEMENTS

There are many people I would like to thank for supporting me in the process of my scientific career. The first of which is my family; specifically my mom and dad, who have always supported my career choices as long as I went as far as I could. My brother has also always done as much for me as he could. I also need to thank Hrothgar and Birch for understanding why I couldn't always be home or go on as many long walks.

The second group of people I would like to thank is my undergraduate lab. To Akif Tezcan, who agreed to take me in his lab as an undergraduate researcher despite poor grades and taught me many lessons and with whom I published my first two papers, I am eternally grateful. To the members of the Tezcan lab, Eric Salgado, Dustin Huard, Robert Radford, Lauren Roth, Jeffrey Brodin, Annette Medina-Morales and Sarah Smith who not only taught me techniques and how to be a good lab mate, but how to have fun in the lab.

Third, I would like to express my eternal gratitude to the wonderful scientific community at Colorado State University. To the wonderful professors who took time out of their busy schedules to teach me new things or to meet with me when I had questions, I thank them. To Chris Ackerson, who took a chance on an unproven, first year graduate student with poor grades coming into to graduate school - I will never forget. To our post-doctoral researchers, O. Andrea Wong and Christine Heinecke, who not only taught me much of what I know, but who were also overwhelmingly friendly and always made me feel at home even during rotations. My humblest regards to my lab mates W. Scott Compel, Marcus Tofanelli, Tim Dreier, Christian Collins, Ricky Nemeth, Chris Hosier and Aly Main, I am forever in your debt for not only helpful discussions, the aid in the lab, but also for all of the laughs and your friendship through the years. To the friends

I have made throughout my graduate career, I am grateful for the support, helpful conversations, and for your listening to countless talks through the years; I will never be able to repay this debt.

And finally, to all of our wonderful collaborators and other professors who have helped me along the way: Jay Nix at Advanced Light Source (beamline 4.2.2) for many helpful conversations and for showing up to fix the beamline at 2 AM; Chris Snow and his research group for supplying us with protein crystals and understanding when our gold nanocluster synthesis sometimes took longer than expected; Hannu Häkkinen and Kirsi Salorinne, thank you for the many helpful discussions on theoretical chemistry and crystallography; Olve Peersen for help running SB Grid and always being communicative about when it needed to be down for maintenance; and Karolin Luger, thank you for access to d*Trek and HKL2000.

TABLE OF CONTENTS

CHAPTER 1. INTRODUCTION

Microscopy has been an integral part of understanding biology for the better part of one and a half centuries. Unfortunately, there is a fundamental problem in looking at biological samples under a microscope, and that is that biological samples require contrast in order to visualize the cell or parts of the cell. There are two ways that we can add contrast to a sample. The first is through a top-down method in which we add chemical agents to give a sample contrast. The second is through a bottom-up methodology in which we can give targets of interest specific chemical functionality in which to generate contrast themselves.

There have been multiple methods developed in order to give cells contrast via a top-down method in optical microscopy. In the 1880s it was found that tris((4-dimethylamino)phenyl)methylium chloride could be used to differentiate bacteria that contain a peptidoglycan layer vs. bacteria that do not.[1] There are stains that can be used that stain DNA which localizes in the nucleus.[2,3] Another stain can highlight various portions of the cell as well.[4] Other methods have been developed, such as a clonable technique to give proteins contrast.[5,6] These methods have been utilized with great efficacy.[7–9] However, as optical microscopy has an obvious limit on the size of viewable targets, one must turn to electron microscopy.

Electron microscopy utilizes electrons instead of visible light to illuminate samples. This allows for not just the imaging of large cellular bodies, but of smaller protein complexes as well.[10–15] However, electron microscopy also suffers from the contrast problem, because all biological samples are made of “light” atoms (i.e., C, H, N, O) which are all transparent under an electron microscope. Similar to light microscopy, biologists soon turned to stains which contained heavy

metals. Stains such as uranyl acetate, osmium tetroxide and lead acetate[16] were found to allow microscopists to visualize proteins. In the early 1990s, it was found that gold nanoparticles could be conjugated to targets to allow for more specific placement of targets.[17–20] However, the procedures often called for conjugation procedures that were not entire clear as to how or what was actually connecting the nanoparticle with the target. In 2007, the first crystallographically solved structure for a gold nanoparticle was published.[21] From this structure it became possible to determine new methodologies of conjugating nanoparticles with biological targets of interest.

By understanding the structure of $Au_{102}(pMBA)_{44}$ (Figure 1.1) and how the thiol groups are attached on the surface, it is now possible to use specific chemistries to attach biological targets to gold nanoparticles. Since the early 1990s it has been known that gold nanoparticles can exchange ligands.[22–24] Through this ligand exchange mechanism it is possible to directly attach gold nanoparticles to a protein of interest if there is a solvent-accessible cysteine. If not, there are a variety of common peptide coupling techniques that are available. The first is through linking free primary amines with carboxylic acid moieties on the ligand layer of the nanoparticle using a NHS-EDC crosslinker (Figure 1.2).[25] The second is through using coordination chemistry. By exchanging on a nitrilotriacetic acid (NTA) moiety one can link the nanoparticle[26,27] to the protein expressing a His-tag and with the addition of a nickel salt.[28–30] The third method of conjugating proteins to a nanoparticle is through the use of a maleimido cross-linker which similarly links a free cysteine on the protein to a maleimide group on the nanoparticle.[31] The

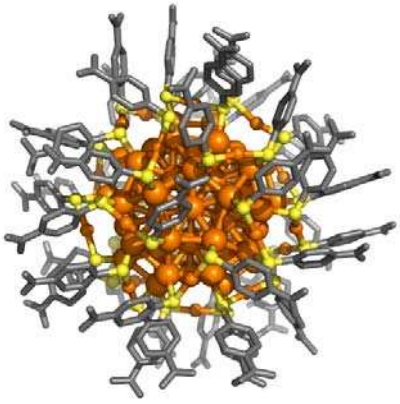

Figure 1.1. Crystal structure of $Au_{102}(p\text{-MBA})_{44}$. Figure reproduced from Jadzinsky *et al*.[21]

maleimide linkage is more robust than a cysteine directly bonded to a nanoparticle because the thiol-maleimide bond is non-reducible, reduction being a concern inside of a cellular environment.[32] The above three methods, are the current most common ways of conjugating proteins to gold nanoparticles. These techniques have the drawback that it is not simple to control how many proteins become conjugated to a single nanoparticle, which may cause imaging issues downstream.

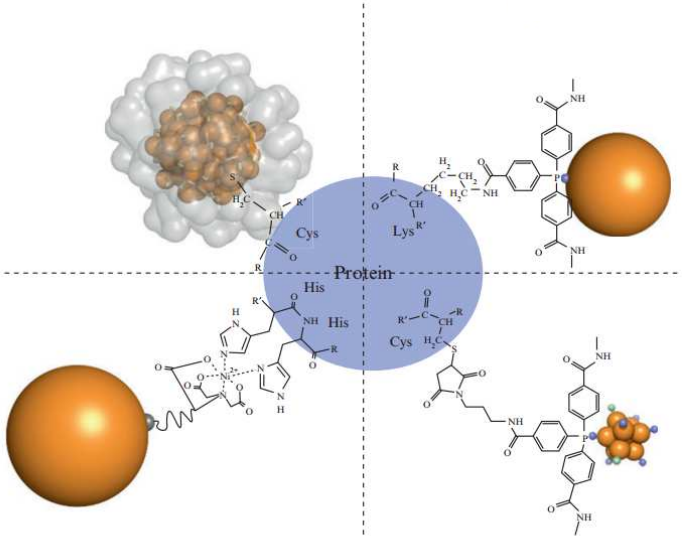

Figure 1.2. Image depicting most common bioconjugation methods between a protein and gold nanoparticle. Image courtesy Ackerson *et al*.[27]

Electron microscopists have also searched for methods of providing their targets with methods of generating contrast themselves. These clonable methods would be analogous to green fluorescent protein (GFP) and would be able to mark proteins of interest with high specificity. There are several requirements to generate a successful clonable inorganic nanoparticle tag. The first is that the tag must be a single polypeptide. This is important because if it is not, the formation of the nanoparticle would recruit proteins from other areas and disrupt cellular function or viability. The second requirement is that the reduction of the ions must be catalytic. This is important as a 5nm AuNP would contain approximately 5000 Au atoms. If the reduction is not catalytic, this means that there would be roughly 5000 residues to reduce all of the ions. In a catalytic reduction the

polypeptide could be much smaller. The third requirement is that the polypeptide must retain the product. This requirement is necessary because if the polypeptide did not retain the product, then the tag would not be very efficient. The final requirement is that there must be a method of controlling the size of the particle. This requirement stems from the fact that the size of the nanoparticle is very important for cellular usage. The ideal size is suggested to be 5 nm in diameter as this size is considered to allow unambiguous identification of particles over cellular background.[27,33,34] Smaller sizes may be useful for more specialized purposes. So far, there is no widely adopted clonable contrast marker in biological electron microscopy.

Naturally occurring proteins have been investigated as candidates for a clonable tag. Naturally occurring proteins investigated include most prominently: ferritin, metallothionein and mini-singlet oxygen generator (mini-SOG). In the case of ferritin, the requirements of catalytic reduction and retention of product are satisfied; however, ferritin is a 24-meric protein which forms a cage. The fact that this is a multimeric protein and is also quite large (0.45 MDa) would likely inhibit its usage as a clonable nanoparticle (Figure 1.3).[35] Metallothionein coordination of Au(I) or Au(III) metal ions is also proposed as a potential method for tagging proteins of interest. While metallothionein is a small polypeptide that is capable of retaining the product, the reduction is stoichiometric which requires a high copy number of the protein in order to visualize. Au(I) salts are also poorly soluble in water, and Au(III) salts are easily reduced by proteins,[36] buffers,[37] and other biomolecules

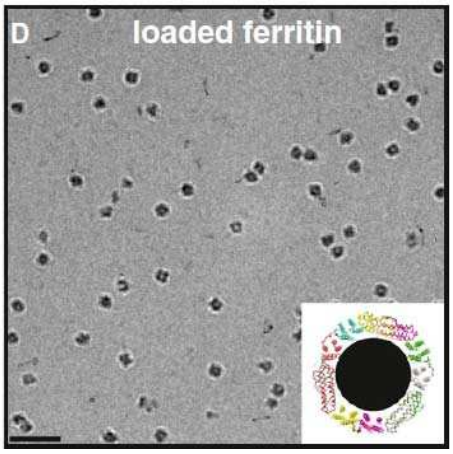

Figure 1.3. Transmission electron micrograph of ferritin loaded with Fe as a potential tag. Image reproduced from Wang *et al*.[35]

encountered in a cellular environment (Figure 1.4).[38–40] Mini-SOG is based off of a small protein that is capable of generating singlet oxygen. The protein has been truncated to form a small polypeptide which is then cloned onto the target protein.[41] Mini-SOG requires diaminobenzidine to form an osmiophilic polymer which is not very well retained by the tag and also has very poor size control (Figure 1.5).[41]

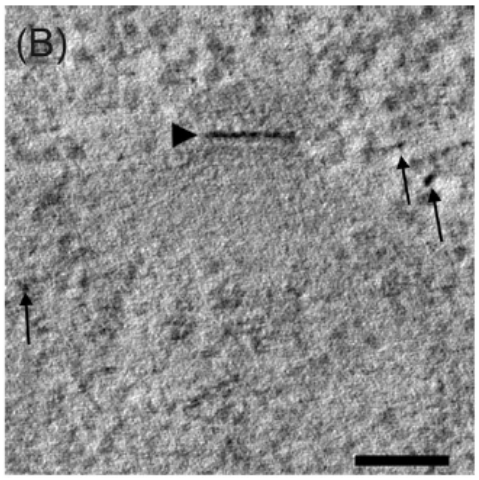

Figure 1.4. Transmission electron micrograph of concatenated metallothionein on SPC42. Arrow in center of micrograph indicates MT-SPC42. Arrows on right hand side of micrograph indicate non-specific reduction of Au^{3+} to nanoparticulate gold. Image reproduced from Morphew *et al*.[36]

In addition to naturally occurring proteins, peptides isolated out of peptide libraries have also been studied for many different properties. These peptides have the ability to make many functional inorganic nanomaterials.[42–44] Peptides isolated out of these libraries have also been capable of forming several non-biogenic inorganic materials such as ZnS, TiO_2, ZnO, CoPt and FePt.[45–50] And while these peptides are extremely small and easily clonable, many of these have issues with controlling the size of the new particle or controlling what is actually causing the reduction step in the nanoparticle formation reaction.[37] While these peptides control sizes of nanoparticles very well and can generally stabilize the nanoparticle well, the reduction is typically done with an external reductant.[37,51,52] Preformed inorganic nanoparticles is another strategy that is used.[42,46]

As can be seen from the work on developing tags for biological electron microscopy, the search for a tag for biological electron microscopy has been investigated thoroughly. Each of the aforementioned systems has pros and cons, so that there is no widely utilized method for tagging

proteins of interest for electron microscopy. A breakthrough in the development of a tag that will allow us to image proteins of interest with electron microscopy will have far reaching consequences in understanding cellular biology.

The work presented here in addresses two chief concerns: 1) understanding the mechanism of exchange, and 2) progress towards a clonable inorganic nanoparticle. These two aspects will help to develop new tags for proteins of interest in the field of biological electron microscopy.

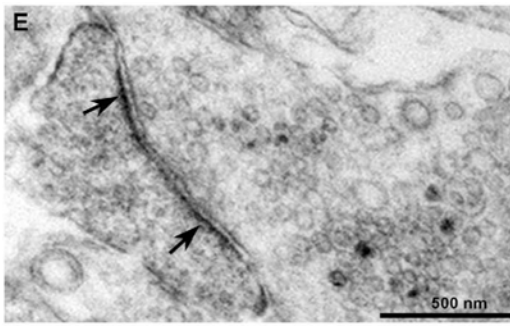

Figure 1.5. Transmission electron micrograph of min-SOG attached to synaptic cell-adhesion molecules (SynCAM). Arrows indicate post-synaptic membrane labeling; note osmiophilic polymer at arrows. Image reproduced from Shu *et al*.[37]

CHAPTER 2. LIGAND EXCHANGE

2.1. INTRODUCTION

Functionalization of gold nanoparticles is a key component in the application of gold nanoparticles. Ligand exchange is the simplest method of functionalizing gold nanoparticles; as such it has been heavily studied by other groups.[23,24,53–60] A majority of these studies were carried out as kinetic studies using NMR to track incoming and outgoing ligands. The NMR studies indicated that there were three distinct regions of exchange (longest rate of exchange is not shown due to time constraints on the plot, days to weeks) (Figure 2.8). This suggests that exchange occurs through an associative mechanism. This makes sense when the theoretical model is compared to the rates of exchange. The theoretical model originally posited that in gold nanoparticles, Au atoms pack into geometric solids (Figure 2.9). This packing model reveals three different Au atom environments which fits well with the kinetic data; however, as was discovered with the structure of Au_{102}(para-mercaptobenzoic acid)$_{44}$ (*p*-MBA)[21], the predicted model and the actual model do not resemble each other. This leaves the question of how to reconcile the experimental NMR data with the structure. It had also been seen earlier that the rate of exchange seems to increase with the addition of the gold-thiol polymer, which is the precursor to nanoparticle formation.[60] With

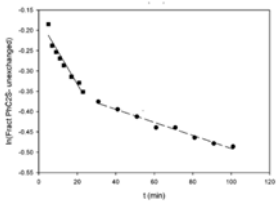

Figure 2.8. Pseudo-first-order rate plot for exchange of phenylethanethiol (PET) for *p*-nitrophenol onto $Au_{144}(SR)_{60}$. Image reproduced with permission from Guo *et al.*[7] and ACS Publications

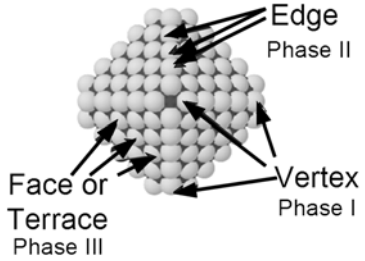

Figure 2.9. Gold nanoparticle idealized as a truncated octahedron, showing three different environments for exchange.

this result, it was unclear what the unit of exchange is; is it a single thiol that is normally used for exchange, or is some portion of the gold-thiol polymer the unit of exchange? These are the two main questions that remained regarding ligand exchange that could be solved with a structural study.

We decided upon utilizing Au_{102}(*p*-MBA)$_{44}$ as our first model system for two reasons, the first being that well established crystallization conditions for Au_{102}(*p*-MBA)$_{44}$ exist, and the second being that while other crystal structures had been solved,[13,61–65] Au_{102}(*p*-MBA)$_{44}$ remains the sole water-soluble gold nanocluster whose structure has been solved and, as such, would likely be a good candidate for future therapeutic work.[66] By determining how ligands exchange we can better understand how nanoparticles are attached to our targets and potentially leverage this information to yield more precise structural information of the target.

Portions of the work presented in this chapter have previously been published in the Journal of the American Chemical Society[67] (Structural and Theoretical Basis Of Ligand Exchange on Thiolate-Monolayer-Protected Gold Nanoclusters) and Inorganic Chemistry (Structural Basis For Ligand Exchange on $Au_{25}(SR)_{18)}$.[68] For CIF files relating to data referred to within this chapter, please refer to the articles.

2.2. STRUCTURAL AND THEORETICAL BASIS FOR LIGAND EXCHANGE ON THIOLATE MONOLAYER PROTECTED GOLD NANOCLUSTERS

We observe ligand place-exchange occurring in two of the 22 symmetrically unique ligand sites (Figure 2.10). As judged by partial Br occupancy in the heterogeneous crystals at position 4 on the phenyl group of each ligand, 48.6% and 60.3% of ligands number 2 and 3 were exchanged. We name the ligands correspondingly as PMBA2 and PMBA3. The same convention was used in

the intial report of the $Au_{102}(p\text{-MBA})_{44}$ crystal structure.[21] The extent of site exchange at these four ligand positions accounts for ~9.1% of the total ligand population on the nanocluster and is consistent with previous studies on $Au_{38}(SR)_{24}$ and $Au_{144}(SR)_{60}$ nanoclusters, namely the finding that the largest rate constant for ligand exchange occurs for 8-25% of the total ligand population.[23,24] Ligand exchange was also done with an approximate feed ration of 2 *p*-BBT ligands per nanocluster. At equilibrium, exactly 1 ligand would be exchanged at this feed ratio; the experimental sum of the occupancies is determined to be 1.08 ligands per nanocluster, suggesting that the exchange reaction reached equilibrium under our experimental conditions, which were a five minute exchange at a concentration of 2:1 incoming thiol:gold.

Conventionally, ligand exchange on AuNPs is thought to take place via an associative mechanism. Such a mechanism necessarily implies accessibility of ligand-binding gold atoms, residing in the ligand shell, to "nucleophilic attack" by the incoming thiol(ate), creating an intermediate that has both incoming and outgoing ligands simultaneously bound to the accessible gold atom. In our system, this implies a transient (*) $[Au_{102}(SR)_{44}SR']^*$ or $[Au_{102}(SR)_{44}HSR']^*$ complex. A solvent accessibility

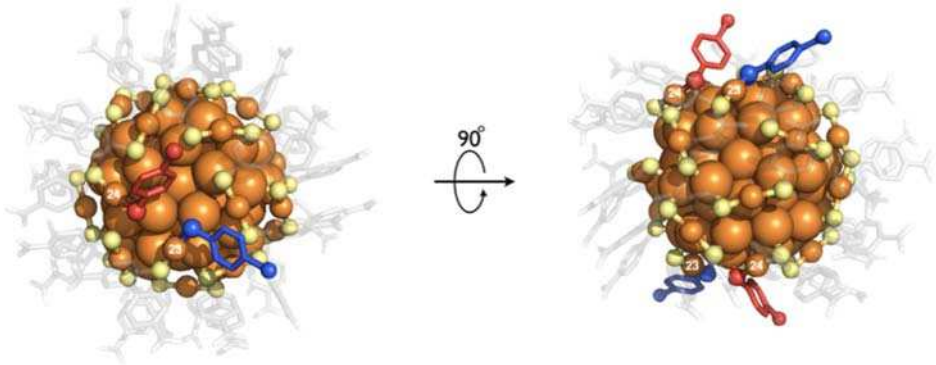

Figure 2.10. Down-axis (left) and face-on (right) views highlighting ligand exchange and associated Au(I) atoms. The exchanged ligands are identified according to previously established convention as PMBA2 and PMBA3[21] and are rendered in red and blue, respectively. The Au(I) atoms associated with these ligands (labeled in white numerals) are important in mechanistic interpretation and are also identified according to the previously established numbering convention.[21] The *p*-MBA ligand layer is rendered semitransparent. Image reproduced with permission from Heinecke *et al.* and ACS Publications.[67]

calculation[69] reveals two solvent accessible gold atoms in the crystallographic asymmetric unit, Au23 and Au24 (Figure 2.11) that are solvent exposed for associative ligand exchange on Au_{102}(*p*-MBA)$_{44}$. Since PMBA2 and PMBA3 are bound to Au23 and Au24 respectively, the ligand-exchanged structure supports a simple associative ligand exchange reaction.

To gain more insight, we used density functional theory (DFT) computations to study details of an associative mechanism for the incoming ligand in both thiol and thiolate form. Each form may be relevant under our experimental (pH and other) conditions; additionally, both thiol and thiolate forms are reported as exchange capable.[59] For computational expediency the calculations were done for a single nanocluster in a finite computational cell, without solvent (water) and with *p*-MBA ligands approximated as simple SH groups. We abbreviate these idealized SH ligands as L, to represent a generic thiolate ligand. In the simplified $Au_{102}L_{44}$ model we considered the associative ligand exchange of ligand position L2 from the staple unit L8-Au23-L2 because Au23 is the most solvent exposed gold atom (Figure 2.11). We considered the "nucleophilic attack" by either $HSCH_3$ (methane thiol) or SCH_3^- (methane thiolate) as the incoming ligand. Because the minimal ligand model used here should not participate in van der Waals interactions, the PBE exchange-functional in appropriate, since it also does not account for van der Waals interactions.

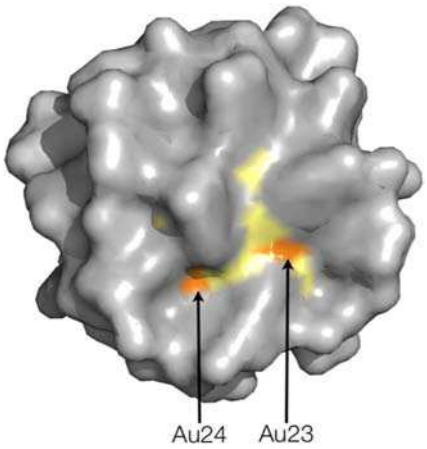

Figure 2.11. Solvent accessibility surface rendering of the crystal structure with carbon, oxygen, sulfur and gold rendered in gray, gray, yellow, and orange, respectively. The two solvent exposed gold atoms in the asymmetric unit are labeled according to convention. The orientation of the structure in this figure is identical to the orientation of the structure in the left panel of Figure 1. Image reproduced with permission from Heinecke *et al.*, and ACS Publications.[28]

Adsorption of an incoming ligand at Au23 is the first step of associative ligand exchange, for which our calculations show a very weak adsorption minimum for methane thiol on Au23 (Figure 2.12a), but a much stronger adsorption minimum for the corresponding thiolate (Figure 2.13, left panel), at -0.05 eV (1 kcal/mol) and about -2.5 eV (59 kcal/mol) respectively. The Au23-$HSCH_3$ and Au23-SCH_3^- bond distances are calculated to be approximately 3.5 and 2.5 Å respectively. The thiolate-Au23 bond distance is similar to other S-Au distances in the nanocluster. Two other locally stable intermediate configurations of methane thiolate-Au23 were also found (Figure 2.13, middle and right panel). In one of the stable configurations (Figure 2.13, middle panel) the L8-Au23-L2 unit is partially desorbed from the gold core to which the excess thiolate is attached. Surprisingly, the total energy of this intermediate configuration is nearly the same as the intermediate in Figure 2.12 in which thiol is the incoming ligand. In the third stable methane thiolate-Au23 configuration (Figure 2.13, right panel) the thiolate does not bind to the core gold atom but forms a disulfide bond. This configuration is clearly endothermic with respect to the others and implies that formation of disulfide bonds is not likely in any part of the reaction.

We were able to complete a plausible reaction path for exchange using methane thiol as an incoming ligand, as summarized in Figure 2.12 (bottom panel). As mentioned previously, the neutral methane thiol has a low adsorption energy, about 1 kcal/mol, to the unit L8-Au23-L2. We find an interesting activation barrier of 15.0 kcal/mol (0.65 eV) to an interesting intermediate configuration (intermediate c in Figure 2.12), in which the incoming methane thiol is inserted into the Au23-L2 bond of the L8-Au23-L2 staple. This intermediate is further illustrated in the top right panel of Figure 2.12. The geometry of this metastable intermediate, L2-H-SCH_3-Au23-L8 is

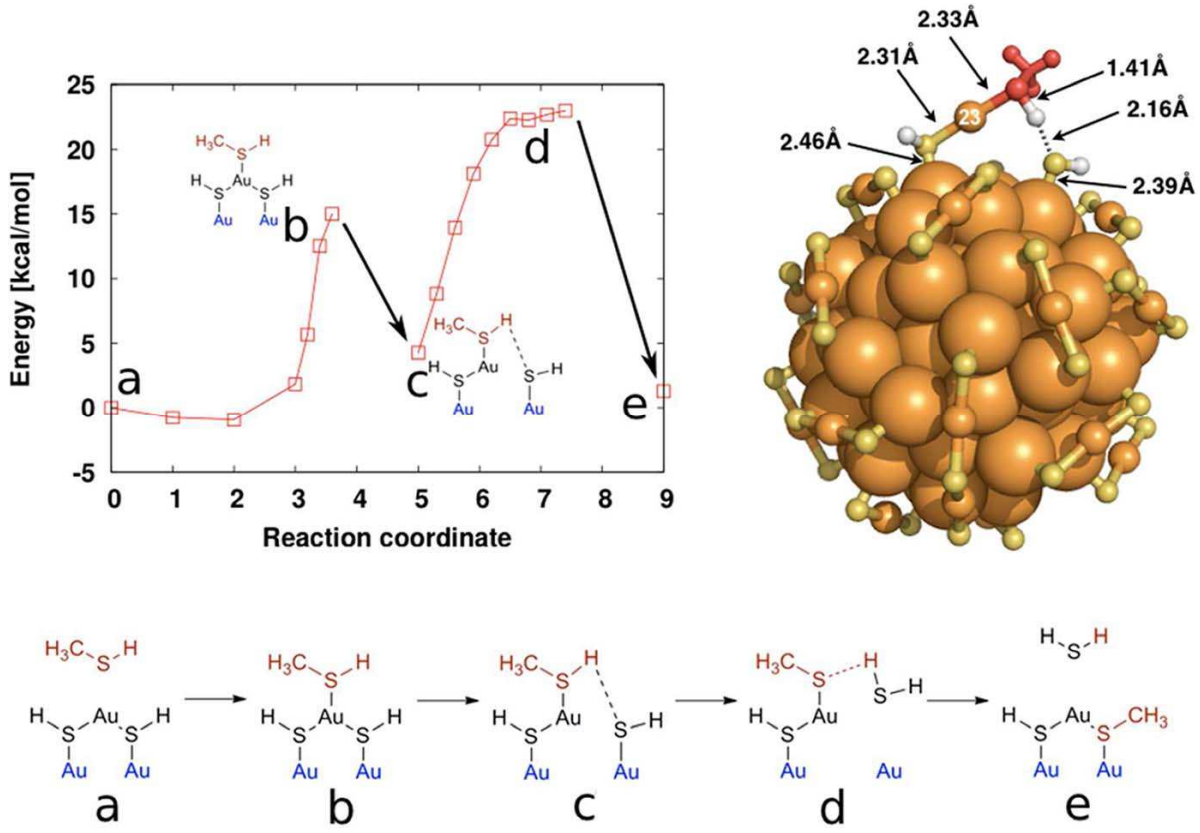

Figure 2.12. Proposed ligand exchange process with methanethiol shown as energy behavior in the top-left panel and depicted as a sketch in the bottom panel. Top-right panel shows a full rendering of the semiring-like transition state c. Configurations close to b and d have been confirmed to be at the local energy maximum by structural relaxations to the intermediate and final states, which are shown here by the arrows from b to c and from d to e respectively. Reaction coordinate is based on the distances from the sulfur of the adsorbed thiol to the Au23 atom from a to b, and from the sulfur of the desorbed thiol to the core Au-atom binding site of the staple from c to d. The structure in the top panel corresponds to reaction intermediate c. Image reproduced with permission from authors and ACS Publications.[28]

strikingly similar to the well-known "semiring" L-Au-L-Au-L unit that is observed in all crystallographically determined, thiolate-protected gold nanoclusters, and is the exclusive protecting unit in all $Au_{25}(SR)_{18}$ nanocluster structures.[61,70] However, in this intermediate, one of the Au atoms in the "semiring" is replaced by an H atom. Depending on the orientation of the residue, the observed bond lengths between the hydrogen of the incoming ligand and the sulfur of L2 vary from 1.9 to 2.2 Å for the longer hydrogen bond to 1.4 to 1.5 Å for the shorter covalent bond. The energy of this intermediate (intermediate c in Figure 2.12) is slightly endothermic (4.3 kcal/mol or 0.19 eV) with respect to the initial state ($Au_{102}L_{44}$ nanocluster and an isolated

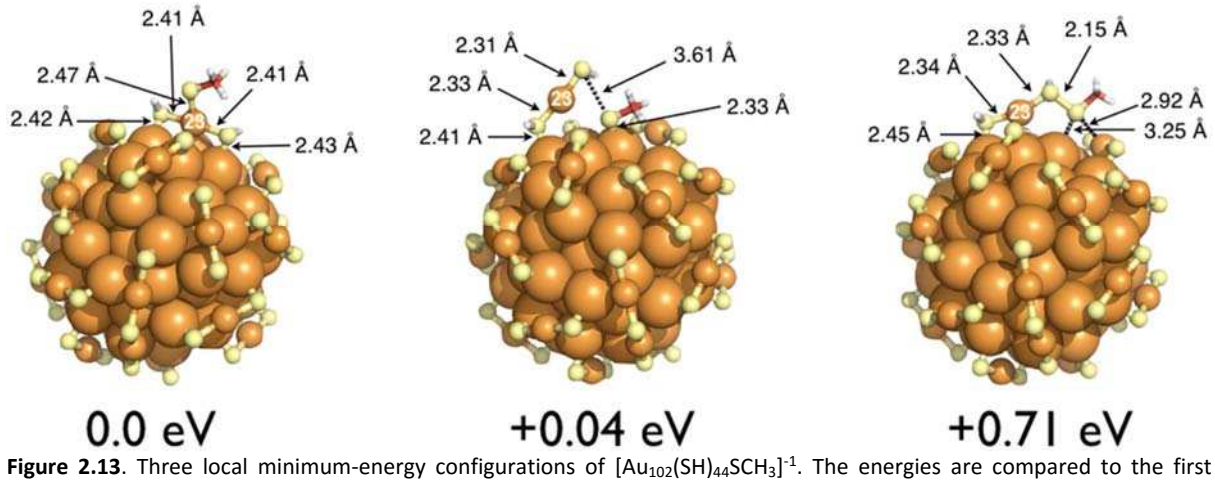

Figure 2.13. Three local minimum-energy configurations of $[Au_{102}(SH)_{44}SCH_3]^{-1}$. The energies are compared to the first configurations on the left, where the methanethiolate is strongly adsorbed on the Au23 atom. Configuration in the middle has an open protecting unit with SCH3- bound to the core separately. The rightmost structure is energetically unfavorable including sulfur-sulfur bonding. Image reproduced with permission of the authors and ACS publications.[28]

methane thiolate). To complete the reaction, the L2 must be released from the structure as SH_2 as described in steps from c to e in Figure 2.12. During desorption, the hydrogen atom of the adsorbed methane thiol is transferred to the ligand L almost immediately. The hydrogen atom selects from either the incoming or outgoing sulfurs (Figure 2.12c) and binds to the one that has a lower coordination number. As the outgoing ligand is being released, (Figure 2.12d), a SCH_3-Au-L8-Au(core) moiety is pointing out from the nanocluster to which the desorbing HSH is (still) weakly bound with a single hydrogen bond between the open-end S of the staple and the H of HSH. The energy barrier for the desorption of HSH is 18.7 kcal/mol (0.81 eV). Following the release of SH_2 from the sulfur of the open end of the active staple and the methane thiolate binds to the core gold atom forming the final configuration (Figure 2.12e). The total effective activation barrier for the ligand exchange process with methane thiol is 23 kcal/mol (1.0 eV). The configuration space of the second transition state is large because of the competing flexibility in energetics due to increase/decrease in the opening angle of the active staple and due to the changes in the weak hydrogen bond. Because of this flexibility, we estimate ±0.1 eV accuracy for

the activation energy at the second transition state around which we did separate calculations to map the configurations and energetics.

We determined the energetics of the net reactions for both methane thiol and methane thiolate reactions and find them both to be essentially thermoneutral (minus and plus signs of the reaction energy denote exothermic and endothermic reactions, respectively):

$Au_{102}(SH)_{44} + SCH3^- \rightarrow Au_{102}(SH)_{43}SCH_3 + SH^-$

$\Delta E \approx$ -4.6 kcal/mol (-0.2 eV)

$Au_{102}(SH)_{44} + HSCH_3 \rightarrow Au_{102}(SH)_{43}SCH_3 + SH_2$

$\Delta E \approx$ +1.2 kcal/mol (+0.05 eV)

Control calculations for the exchange of *p*-MBA to *p*-BBT at PMBA2 and PMBA3 sites in thiol and thiolate forms yield only slightly more exothermic (-4 and -7 kcal/mol) reaction energies which were obtained by structural optimization of the initial (5a) and final (5e) states. Although the van der Waals interactions are not included in the PBE exchange-functional, it can be assumed that the contribution to the energy of the initial and final state would be similar, as the only difference is the replacement of the COOH group with a Br atom. Consequently, in the absence of clear enthalpic contributions, the calculations suggest that this reaction is driven by entropic mixing of the chemical entities in the ligand layer. Finally, our calculated value for dissociative mechanism is quite energetically costly (approximately 1-4 eV) and consequently improbable.[71]

2.2.1 Structural Nature of Exchange

The crystal structure of the exchanged $Au_{102}(SR)_{44}$ was solved from a heterogeneous crystal where the "static substitutional disorder" for each exchanged ligand was quantified in the

crystallographic refinement process. The relative occupancies of *p*-BBT ligands in each exchanging site provide several insights into the structural and chemical kinetic nature of ligand exchange.

Previous studies of ligand exchange, from kinetic, NMR and EPR spectroscopic methods,[23,24,59,60,72,73] generally suggested ligand exchange as an associative mechanism, and at least one previous study suggests that an RS-Au(I)-SR moiety may represent a functional unit of exchange.[60]

While the exchange of PMBA2 and PMBA3 is consistent with the associative exchange mechanisms, this study reveals that the overall picture of ligand exchange is somewhat more complex. For instance, the different Br occupancy values of 48.6% and 60.3% suggest some mechanistic insights not suggested in previous studies. First, while associative mechanisms imply a dominant role for accessibility of the "electrophilic" atom, solvent accessibility of the Au(I) atoms in the ligand layer does not predict absolute reactivity of the Au(I) atom toward ligand exchange. Specifically, the solvent accessibility area for Au23 and Au24 is estimated to be 1.13 and 0.19 $Å^2$, respectively, assuming a probe radius of 1.4 Å, corresponding to a water molecule as the solvent. However, the less exposed Au24 results in ligand exchange with greater exchanged ligand occupancy. Also, a simple associative exchange mechanism would imply that both thiolate ligands bonded to Au23 and Au24 should exchange, perhaps even at equivalent rates, meaning we should also observe substantial exchange of PMBA8 and PMBA9, bonded to Au23 and Au24 respectively.

The differences from the simple ligand exchange picture and the one observed here may be partially explained by noncovalent (i.e., π-stacking) interactions in the ligand layer and

possible selective crystallization of some ligand exchange products. The noncovalent interactions in the ligand layer are a further challenge for modeling as well, as it would require a reliable account of dispersion forces that is missing in the standard DFT computations. Possible ligand-ligand interactions should increase the activation barriers of the ligand-exchange process. Interactions with solvent molecules increase the number of possible reaction paths as well as their complexity. Selective crystallization may also mean that we do not observe exchange of ligands in the crystal structure that in fact exchanged in solution. An analysis of ligands involved in crystal contacts shows that 11 of the 22 ligands in the asymmetric unit mediate some form of crystal contact. Of the ligands attached to solvent accessible Au atoms, PMBA2, PMBA 3 and PMBA 9 are not involved in crystal contacts, while PMBA8 is. This analysis suggests that selective crystallization might have suppressed observation of PMBA8, but not PMBA9. In the context of these experimental complications, a full explanation of ligand exchange at solvent exposed Au(I) atoms may require a more detailed structural study of ligand exchange reactions.

Ensemble measurements of the extent of ligand exchange prior to crystallization could give insight into the extent to which selective crystallization influences our crystallographic observations. We found such measurements to be difficult, as NMR and MALDI-MS are complicated for the $Au_{102}(SR)_{44}$ system and elemental analysis would require grams of material, which is presently an impractical amount, to accurately quantify the small amount of Br in the exchanged product.[74]

A further question unaddressed by this structure is how ligands that are not bonded to solvent accessible Au(I) atoms might exchange. The mechanism of exchange implied by the present X-ray crystal structure can account for exchange of 2 of the 22 symmetry unique ligands

in this nanocluster. Many if not all of the remaining 20 ligands are presumed to be exchangeable, implying the existence of at least one additional mechanism of exchange.

Other structural mechanisms that are suggested as relevant for ligand exchange on MPCs include exchange of entire RS-Au(I)-SR units and translation of ligands from nonexchanging sites into exchanging sites. The ligand exchange structure suggests that RS-Au(I)-SR unit exchange cannot be the only mechanism of ligand exchange, but does not rule it out as a possible secondary mechanism of exchange for other ligands.

The differing ligand occupancies also provide some insight with regard to the kinetics of exchange. From a standpoint of chemical kinetics, previous literature suggests three exchange environments. This literature notes several deviations from ideal behavior. The dramatically different occupancies in the two symmetry unique ligands that exchange in this structure suggest an even more kinetically complicated picture in which potentially each symmetry unique ligand-exchanging site has its own exchange constant. The previously studied compounds in ligand exchange are of higher inorganic core symmetry than Au_{102}; specifically Au_{25}, Au_{28} and Au_{144} conform to distorted O_h, D_3 and *I* point groups, respectively. Both differences may result in an even more kinetically complex exchange environment on $Au_{102}(SR)_{44}$ as compared to $Au_{25}(SR)_{18}$, $Au_{38}(SR)_{24}$, and $Au_{144}(SR)_{60}$.

We notice a parallel between this work and the previous work of Stellacci and colleagues. In Stellacci's previous work, reactivity of larger 10 and 20 nm gold nanoparticles for ligand exchange is shown to be greatest atop the highest symmetry axes (poles) of these nanoparticles.[75] Similarly, we see greatest ligand reactivity for the ligands atop the pseudo-5-fold symmetry axis in Au_{102}(*p*-MBA)$_{44}$. The "hairy ball theorem" may partially explain both results.[76]

The “hairy ball theorem” states that it is not possible to “align hairs” onto a sphere without generating two singularities. These singularities often end at the particle poles. The ligands at these poles are assumed to assume a non-equilibrium tilt; as the ligands are not optimally stabilized by intermolecular interactions with neighboring ligands are expected to be replaced first in ligand exchange reactions.[75]

Finally, we note that just as proteins can be conceptualized as a C_1 symmetric rigid alpha-carbon backbone with chemical functional groups (amino acid side chains) in precise 3-D location/orientation, the $Au_{102}(SR)_{44}$ nanocluster can be similarly viewed as possessing a low symmetry (C_2), rigid inorganic core and chemical functional groups (thiolate ligands) in precise 3-D location and orientation. We show here that these amino acid like groups can be discretely exchanged, with notable occupancy differences among those that are exchanged which may arise from kinetic differences in reactivity. Previous work suggests that most or all of these ligands are exchangeable in more aggressive exchange conditions. Since differences in the reaction kinetics of competing reactions are the foundation for all of synthetic chemistry, kinetic differences in exchange rates of the 22 symmetrically unique ligands in $Au_{102}(p\text{-MBA})_{44}$ might enable the modification of this low symmetry macromolecule to display a very “protein-like” molecular surface, with precisely positioned functional groups displaying desired charge, hydrophobicity or polarity properties.

2.3. STRUCTURAL BASIS FOR LIGAND EXCHANGE ON $Au_{25}(SR)_{18}$

We decided to investigate whether or not the results seen from the $Au_{102}(SR)_{44}$ exchange were universal for other clusters. We decided to look at $Au_{25}(SR)_{18}$ as the ligand environment is significantly different from that of $Au_{102}(SR)_{44}$ and the core displays a much higher symmetry.

$Au_{25}(SR)_{18}$ is also closer in structure to other organosoluble clusters. This would hopefully allow us to build a clearer picture on ligand exchange and further our understanding of using AuNPs as tags.

Recently, it was shown that each of the 18 possible ligand-exchange products can be isolated by column chromatography.[53] Despite the intensive study of this compound for structural, chemical, and catalytic purposes, there are no prior structures of partially ligand-exchanged $Au_{25}(SR)_{18}$ to our knowledge.[77–79]

Here we present the first crystal structure of partially exchanged $Au_{25}(SR)_{18}$. The ligand-exchange reaction was done on a short time scale, roughly seven minutes, isolating ligand sites corresponding to previously identified kinetic "fast exchange" sites. In our crystal structure, we observe the exchange of 1 of 9 symmetry unique ligands (Figure 2.14), in a position that is consistent with an associative mechanism.

Ligand exchange was accomplished by the reaction shown in Scheme 2.4. Briefly, $Au_{25}(SC_2H_2Ph)_{18}^0$, hereafter $Au_{25}(PET)_{18}$, was exposed to a 5-fold molar excess of *p*-BBT for 7 minutes in

$$Au_{25}(PET)_{18} + 2\ p\text{-BBT} \rightleftharpoons Au_{25}(PET)_{16}(p\text{-BBT})_2 + 2\ PET$$

Scheme 2.4. Proposed ligand exchange of $Au_{25}(PET)_{18}$ with *p*-BBT.

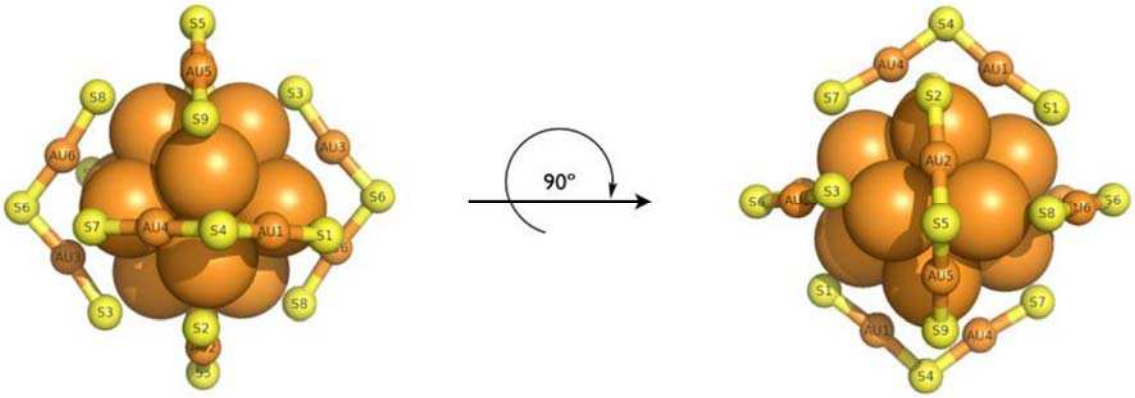

Figure 2.14. Au and S atom numbering convention. Image reproduced with permission from authors and ACS Publications.[38]

CH_2Cl_2, resulting in products corresponding to the fast ligand-exchange environment for this cluster. A full description of the experimental details can be found in the methods section. Single crystals of the crude product were grown by slow cooling from a saturated toluene/ethanol solution.

Diffraction patterns were recorded at the Advanced Light Source (ALS) as described in the methods. The diffraction patterns were indexed to $P\bar{1}$ in XDS[80] and XPREP (version 6.12; Bruker AXS: Madison, WI, 1999). Refinement of the structure of the ligand-exchanged Au_{25} was done in SHELX.[81]

Static substitution refinement in SHELX was used to determine the occupancy of both original (PET) and incoming (*p*-BBT) ligands in each of the nine symmetry-unique ligand positions. We number each symmetry-unique ligand from 1 to 9 according to the observed or expected reactivity for ligand exchange (vide infra), and we numbered each Au atom according to the same convention. In the coordinate file, the numbering of each S headgroup identifies the ligand number.

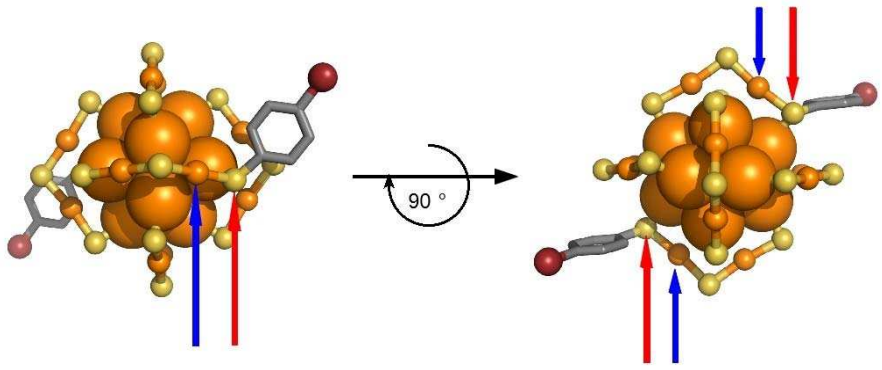

Figure 2.15. Single-crystal X-ray structure of $Au_{25}(PET)_{16}$(*p*-BBT)$_2$. Color code: orange, Au; yellow, S; gray, C; red, Br. Red arrows point to the S headgroup of ligand 1 and blue arrows to Au1. Orientation of the molecules are identical to Figure 2.15. Image reproduced with permission from authors and ACS Publications.[38]

The occupancy by the *p*-BBT ligand was refined to 74.6% for ligand 1. Static substitutional refinement in each of the

other eight ligand positions either failed to refine or refined to zero *p*-BBT occupancy. Figure 2.15 shows a rendering of the crystal structure, highlighting the exchanged ligand.

The exchange of this unique ligand site can be explained by a combination of the solvent accessibility of Au atoms bonded to the ligands and noncovalent interactions of ligands within the ligand shell. Solvent exposure of Au atoms bonded to S ligand headgroups is a requisite for the expected associative ligand exchange because the solvent-exposed area represents a surface capable of bonding to an incoming ligand.[67] Noncovalent ligand interactions in the ligand shell may stabilize certain ligands against exchange, even if they are bonded to solvent-exposed Au atoms.

The solvent-accessible surface area was calculated with PyMOL[82] (Schrödinger, LLC). A total of 3 of the 13 Au atoms in the asymmetric unit have some degree of solvent exposure. Each of these Au atoms is in a semiring; each of the six semirings of the Au_{25} cluster contains one solvent-exposed Au(I) atom. According to our numbering convention, the solvent-exposed Au(I) atoms in the asymmetric unit are Au1, Au2 and Au3 (Figure 2.16). The calculated solvent exposure (assuming a solvent probe radius of 1.76 Å, corresponding to CH_2Cl_2 to approximate the effective size of the CH_2Cl_2 molecule) of Au1 is 3.53 $Å^2$, followed by Au2 and Au3 with 1.8 $Å^2$ and 1.94 $Å^2$, respectively. In the present crystal structure, ligand exchange occurs only for the ligand bonded to Au1, the most solvent-exposed Au atom. This is structurally consistent with an associative mechanism, It is also consistent with our results for structural ligand exchange on $Au_{102}(SR)_{44}$.[67]

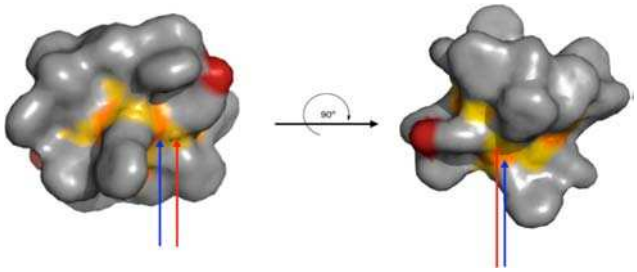

Figure 2.16. Solvent-exposed surface area of $Au_{25}(PET)_{16}(p\text{-BBT})_2$. The orientation of the molecules and color schemes are identical with those in Figure 2.15. Probe radius used is 1.76 Å. Red arrows point to the S headgroup of ligand 1 and blue arrows to Au1.

There are five other ligands attached to solvent-accessible Au atoms in the asymmetric unit: ligands 2-6. Ligand 4 is the apex ligand of Au1. Ligands 2 and 5 are core and apex ligands of Au2. Ligands 3 and 6 are core and apex ligands of Au3.

Ligand 4, like ligand 1, is bonded to Au1. We rationalize the nonexchange of the apex-positioned ligand 4, in part, by comparing the bond lengths as a proxy for bond strength. Ligand 4 Au-SR-Au bond lengths are 2.284 and 2.309 Å, while ligand 1 bond lengths are 2.280 Å and 2.390 Å. These bond lengths suggest that the ligand we observed to exchange is more weakly bonded.

The nonexchange of ligands 2-6, despite their bonding to solvent-accessible Au atoms, is puzzling, especially in the cases of ligands 2 and 3. That nearly 80% of ligand 1 is exchanged and there is no evidence of ligands 2 or 3 is inconsistent with the typical observation of ligand exchange, resulting in a distribution of products.[53]

To rationalize the exchange of only 1 of the 9 symmetry unique ligands, we analyzed the crystal contacts of the ligands in Mercury[83] (CCDC). This analysis reveals the interactions summarized in Table 2.1.

Table 2.1. List of Inter-and Intramolecular interactions observed in the crystal structure.

		contacts	
Au atom	ligand	intramolecular	intermolecular
1	1 (core)	ligand 3	ligand 8 (substantial)
1	4 (apex)		toluene
2	2 (core)		ligand 2
2	5 (apex)		
3	6 (apex)		ligand 9-phenyl-phenyl
3	3 (core)	ligand 1	

Ligand 4 (apex of Au1) interacts with a toluene as well as intramolecularly with its own ethyl group. Ligand 1 (Au1, exchange, edge) shares a great

deal more intermolecular contact with S8 (meaning that C30 and C31 are close enough to share many potential points of contact (C30-C60 2.639 Å, C30-C61 3.261 Å, C30-C59 2.748 Å, C31-C59 2.951 Å, C31-C60 3.236 Å, C31-C58 3.043 Å) and intramolecularly S3's C7 (as noted above). In the absence of 4-BBT at the S1 position, C153 and 154 (phenyl ring of PET at S1) has an intramolecular interaction with S9's C54 (3.142 Å and 3.076 Å, respectively) as well as an intermolecular interaction from C156 (S1 PET's phenyl ring) to C156 (3.019 Å). Ligand 5 (Au2, apex) has no intermolecular interactions, but has intramolecular interactions between the phenyl ring (C32) and Ligand 5 itself, as well as having some interactions to its own ethyl group (C71). Ligand 2 (Au2, core) has an intermolecular interaction with another cluster's S2 (3.284 Å) as well as intramolecular interactions with its own ethyl group. Ligand 6 (Au3, apex) bonds intermolecularly to an adjacent cluster's Ligand 9 (3.319 Å) which stabilizes the ligand layer. Ligand 3 (Au3, core), which does not have any intermolecular interactions, does have intramolecular interactions with C28 of Ligand 1 (*p*-BBT) at 3.399 Å, and the phenyl ring interacts with S3 (its own) C75 (first carbon of the ethyl group). These interactions potentially help to explain why only one of the positions that is solvent accessible exchanges. We do note, however, that the exchange of p-BBT into ligand position 1 generates several crystal contacts, possibly reinforced by π-interactions, compared to the native PET ligand. This substantial set of contacts is shown in Figure 2.17. Thus, it is possible that the ligand exchange that we solved crystallographically results from selective crystallization of one of several product s of the ligand-exchange reaction.

In summary, presented here is the first structure of $Au_{25}(SR)_{18}$ after non-complete ligand exchange. We observe ligand exchange for ligands bonded to only the most solvent-accessible Au atoms in the structure. Crystal contact analysis suggests that we may have crystallized a subset

of the possible ligand-exchange products. The exchange occurring only for ligands bonded to solvent-exposed Au atoms is consistent with previous kinetic and structural studies of ligand exchange on $Au_n(SR)_m$ nanoclusters.

2.4. EFFECTS OF LIGAND LAYER ON CLUSTER CHIRALITY

Upon observing non-complete exchange of $Au_{25}(SR)_{18}$ we decided to further investigate ligand exchange. Instead of using *p*-BBT, we decided to investigate different ligands to better understand structure of these nanoclusters. Again we decided to use $Au_{25}(SR)_{18}$ as our model system as it is a simpler system to work with as the synthesis is more robust and the crystallization is more dependable. We decided to probe if there is a structural difference in $Au_{25}(SR)_{18}$ that is optically active vs $Au_{25}(SR)_{18}$ that is not; and if there was a critical number of ligands that would need to be exchanged before the cluster becomes chiral.

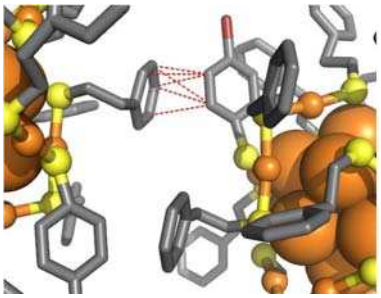

Figure 2.17. Crystal contacts between ligand 1 and ligand 8 of an adjacent cluster in the crystal, as identified by Mercury. Image reproduced with permission from authors and ACS Publications.[38]

It is known from $Au_{25}(SR)_{18}$ synthesized with 1-PET that the ligand layer can impart chirality to the nanocluster.[84] $Au_{25}(2\text{-PET})_{18}$ is theorized to be unlikely to exhibit chirality.[85] The origin of chirality is thought to arise from the ligands and surface gold atoms.[84] We were interested in determining, how many ligands would need to be exchanged in order to cause an achiral structure to turn chiral, which should be easily captured through crystallographic methods.

The ligand we chose to synthesize for our experiment was camphorthiol.[86] We chose this ligand instead of the more commonly used 1-PET due to odor concerns. We also opted for camphorthiol over another more commonly used chiral ligand, S-BINAS, due to synthetic

considerations. In order to maintain core similarities to our previously solved structures, we chose $Au_{25}(PET)_{18}^{0}$ as the Au_{25} we would look at rather than the -1 or +1 charge state as we had already previously shown a method of exchanging ligands onto $Au_{25}(PET)_{18}^{0}$.[87] The synthesis of camphorthiol was accomplished following previously reported methods.[86] A similar ligand exchange procedure was followed as with our previous work. However, after following similar crystallization conditions as previously was seen to form high quality crystals of $Au_{25}(PET)_{18}^{0}$, no crystals formed with the new camphorthiol ligand exchanged on. It is known that the $Au_{25}(PET)_{18}^{0}$ is less stable than the $Au_{25}(PET)_{18}^{-1}$ cluster[87] which was also seen during ligand exchange reactions involving longer exchanges utilizing *p*-BBT as well as standard conditions utilizing camphorthiol which resulted in the exchange solution becoming clear and colorless which indicated that the clusters were being etched. Due to the difficulties involved with exchanging ligands on $Au_{25}(PET)_{18}^{0}$, we switched to $Au_{25}(PET)_{18}^{-1}$, which is a more stable cluster. Clusters were solubilized in toluene along with camphorthiol then washed with ethanol and centrifuged. The pellet was resolubilized in toluene and then layered with ethanol and allowed to crystallize in a -20 °C freezer. While no crystals had formed, UV-vis spectroscopy suggests that the $Au_{25}(PET)_{18}^{-1}$ cluster remains intact during exchange as none of the peaks are degraded (Figure 2.18).

2.5. EFFECTS OF A BIDENTATE LIGAND ON THIOLATE-MONOLAYER-PROTECTED GOLD NANOCLUSTERS

Another avenue we were interested in pursuing is that it is known that monodentate ligands can exchange, but that does not exclude that exchange may also occur through multidentate ligands. As had been seen previously when Au-S staples are added to an exchange reaction, the exchange seems to occur at a faster rate.[60] In order to probe this, we attempted to

exchange on ligands that would roughly correspond to the entire cluster in order to probe whether or not it would be possible to exchange off two different positions on the same cluster or if we would instead see crosslinking across nanoclusters. In order to aid in crystallization, we chose a ligand with two different properties. The first property was to include a π-acceptor to aid in crystallization of the cluster as we had seen previously.[68] The second desired property was that the ligand be rigid; this would aid in visualizing the electron density.

We synthesized the ligand 3,3'-(ethyne-1,2-diyl)dibenzenthiol (L1) as it afforded us all of our prerequisites. Ligand synthesis followed previously reported methods.[88] As before, a similar exchange was carried out on $Au_{25}(PET)_{18}^{0}$ again, as this would allow us to avoid complications between counterions. Ligand exchange was performed as with our previous work. Again, the solution was allowed to slowly evaporate in a -20° C environment, which has yielded high quality crystals in the past, however, again no crystals formed. Similar to the case with camphorthiol, when ligand exchange was undertaken with $Au_{25}(PET)_{18}^{0}$, the clusters were seemingly destroyed.

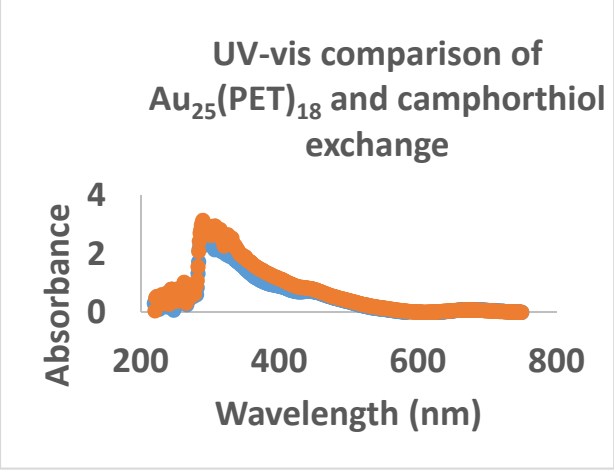

Figure 2.18. UV-Vis comparison of $Au_{25}(PET)_{18}^{-1}$ after one day of exchange with camphorthiol. Blue represents $Au_{25}(PET)_{18}^{-1}$ after purification. Orange indicates $Au_{25}(PET)_{18-x}(camphorthiol)_x$.

Again, when exchanged with $Au_{25}(PET)_{18}^{-1}$, the UV-vis spectrum revealed that the cluster had not degraded (Figure 2.19).

2.6. EFFICACY OF GOLD NANOPARTICLE BINDING TO A PROTEIN CRYSTAL SCAFFOLD

In order to test the effectiveness of our ligand exchanged AuNPs as tags, we required a test system. This test system

would need to yield high quantities of protein, be easily crystallizable, have large enough solvent channels to easily load gold nanoparticles into and finally be periodic enough to aid in electron microscopy studies of the model system.

Our model system to test ligand exchanged clusters was a periplasmic protein isolated out of Campylobacter jejuni (RCSB ID 2FGS, CJ1) (Figure 2.20).[89] The crystal structure revealed that large solvent channels with a diameter of 16 nm would be formed. The structure is formed out of a single monomer which allows for N-terminal tagging with a six fold histadine tag. As the structure is highly symmetric this model system allows for determining how efficient our gold nanoparticle labeling would be, as electron microscopy should show very periodic positioning of the gold nanoparticle tags.

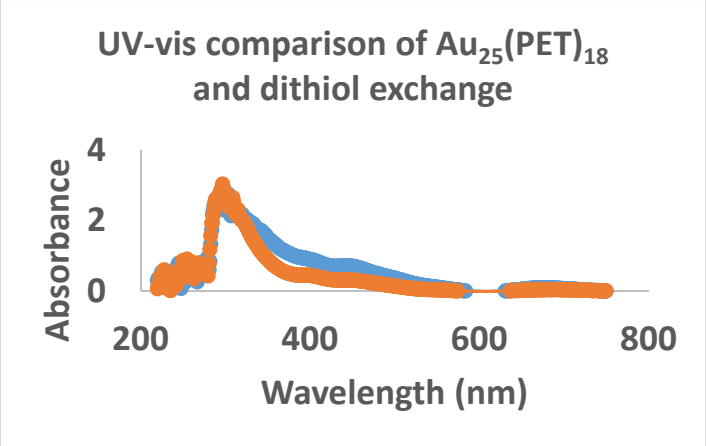

Figure 2.19. UV-Vis comparison of $Au_{25}(PET)_{18}^{-1}$ after one day of exchange with L1. The blue trace is the spectrum for $Au_{25}(PET)_{18}^{-1}$. The orange trace is the spectrum for $Au_{25}(PET)_{18-x}(L1)_x^{-1}$.

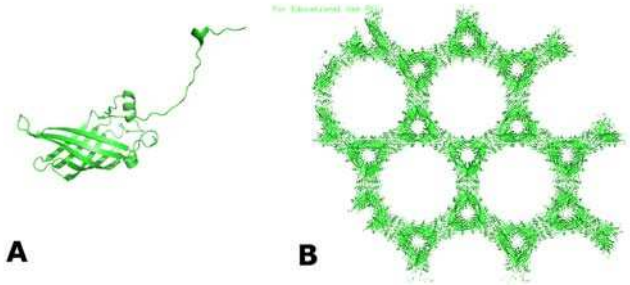

Figure 2.20. Structure of 2FGS. Image in A represents a single monomer of the protein. B represents the packing of 2FGS in crystalline form. The large pores seen in panel B are ~16 nm in diameter and the smaller pores are ~3 nm in diameter.

In order to take advantage of the protein engineering of CJ1 accomplished by our collaborators in the Snow group, it was important to determine nanoparticles that would be utilized for the labeling

experiments. The first cluster decided upon was $Au_{25}(SG)_{18}$ as it has natural fluorescence[90] which would aid in monitoring the loading of nanoclusters into the protein crystal. The second nanoparticle synthesized was a 10 nm gold nanoparticle. This size was chosen as it would easily fit into the solvent accessible channels and be visible by transmission electron microscopy (TEM). In order to take advantage of the 6x histadine tag (His-Tag) on CJ1 it was necessary to attach a ligand onto the nanoparticles capable of binding nickel ions which are bound to the His-Tag. This was accomplished by synthesizing (1S)-N-[5-[(4-mercaptobutanoyl)amino]-1-carboxypentyl]iminodiacetic acid (HS-NTA).[26]

$Au_{25}(SG)_{18}$ was synthesized using a modified procedure that was previously published.[90–92] The clusters were purified via polyacrylamide gel electrophoresis (PAGE) (Figure 2.21), following previous studies using ESI-MS to determine the correct cluster.[93,94] Clusters were washed and dried then redissolved in DI H_2O and mixed with 5 mol equivalents of HS-NTA and allowed to react for seven and a half minutes following our previous studies on ligand exchange of similar sized clusters.[68] The exchange reaction was then washed in EtOH and pelleted and dried to yield a reaction mixture of $Au_{25}(SG)_x(S\text{-}NTA)_{18-x}$. Exchange was confirmed by PAGE, in Figure 2.21, B shows the original product in lane 1 while post exchange is seen in lane 2. The reason for mobility shift is that by exchanging on S-NTA, the electronics of the ligand layer have changed, which increases the charge which changes the gel mobility.

The 10 nm gold nanoparticles were synthesized using a previously published procedure,[95] which yielded a red solution (Figure 2.22, A). Following synthesis of the clusters, oleylamine was exchanged off for 3-mercaptopropionic acid (3-MPA) which yielded a clear blue solution which initially might indicate larger clusters than 10 nm; however under TEM, it was revealed that due

to the short ligand length, clusters were aggregating together causing a plasmon shift (Figure 2.22, B).[96–98] The oleylamine coated AuNPs were calculated to have a diameter of 8.2 ± 2.2 nm. The 3-MPA coated AuNPs were not reliably able to be characterized due to aggregation.

Upon addition of tetramethylammonium hydroxide (TMA) the solution turned a dark red and upon TEM analysis it was shown that the particles had deaggregated (Figure 2.22, C). The addition of TMA effectively changes the counterion bound to the AuNP which affects the ability of nanoparticles to aggregate together (Figure 2.22, C).[99–101] 3-MPA coated AuNPs were calculated to have a diameter of 7 ± 3 nm. The dispersity is likely due to the small size of the ligand exchanged onto the particle allowing for more particle growth due to inefficient capping.[102]

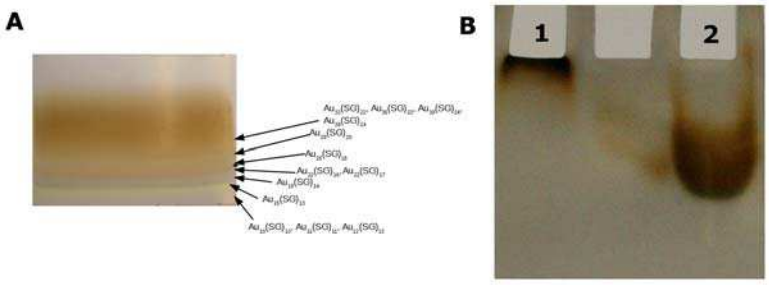

Figure 2.21. (A) 24% polyacrylamide gel showing purification of $Au_{25}(SG)_{18}$ from synthesis. (B) 24% polyacrylamide gel with $Au_{25}(SG)_{18}$ in lane 1 and $Au_{25}(SG)_{18-x}(S\text{-}NTA)_x$ in lane 2.

Ligand exchange methods were first tested on commercially available 10 nm AuNP coated in tannic acid. The nanoparticles were revealed to be 9.97 ± 1.04 nm in diameter by TEM, using ImageJ.[103] Upon ligand exchange, the inorganic core remains the same size, 10 ± 1

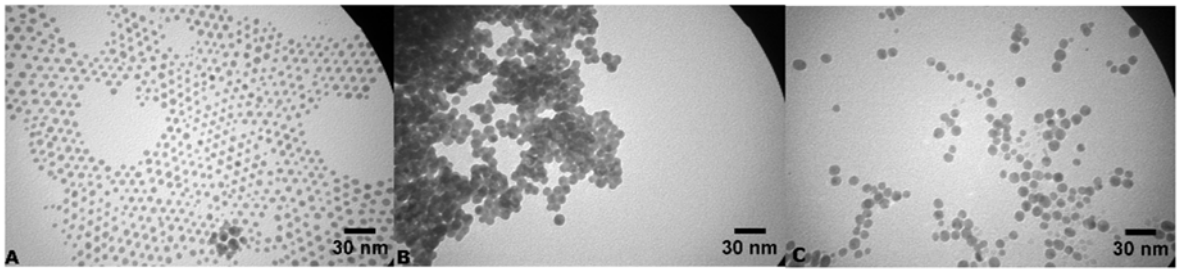

Figure 2.22. Transmission electron micrographs showing the aggregation by exchanging ligand layer. A) oleylamine coated B) 3-MPA coated C) 3-MPA coated with TMA added to solution.

nm, however dynamic light scattering (DLS) reveals that the ligand layer has become perturbed (Figure 2.23). DLS reveals that the ligand layer becomes slightly smaller and a small portion of the clusters had begun to form larger clusters.[55,102] The contraction of hydrodynamic diameter is likely due to a combination of introduction of a smaller ligand layer but also the effect the counterion has on hydrodynamic diameter.[101,104] The gold nanoparticles were soaked into preformed CJ1 crystals by our collaborators, Thaddeus Huber, Ann Kowalski and Chris Snow. It was found by inductively coupled plasma mass spectrometry (ICP-MS) that $Au_{25}(SG)_{18}$ could be successfully loaded and unloaded and the amount of gold found correlated well with time allowed to soak (Figure 4.1). As is seen in Figure 2.24, a maximum loading is reached at eight hours, and as time increases none of the gold is seen to leech out. However, in the presence of EDTA all of the gold is found to be unloaded. Nonetheless, these experiments do not allow us to probe whether or not the gold is in fact inside of the pores or attached to the outside of the protein crystal.

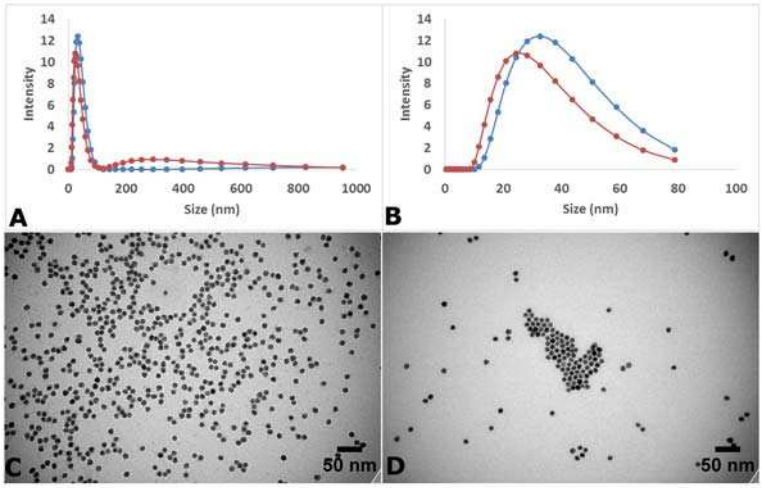

Figure 2.23. Panel A shows the full size range from DLS experiments. Panel B is zoomed in on the size range where particles are observed. In each panel, blue represents data from 10 nm AuNPs; red represents data from 10 nm AuNPs post ligand exchange. Panel C is a transmission electron micrograph of 10 nm AuNP without ligand exchange. Panel D is a transmission electron micrograph of 10 nm AuNP post ligand exchange.

In order to gain a clearer image of what is happening inside of the crystal, protein crystals were soaked with 10 nm AuNPs with HS-NTA and placed onto 200 mesh Cu grids coated in carbon, which had been previously glow discharged in ambient atmosphere. Upon imaging, the crystals were deemed to be too thick to image through using a JEOL JEM-1400 Transmission Electron Microscope operating at 100 kV (Figure 2.25). Two different approaches were then attempted to circumvent this issue. The first approach is through traditional biological electron microscopy techniques for imaging cells. As cells are often too thick to image through, often cells are embedded in resin and then sliced into thin sections around 100-200 nm thick. These sections should allow for direct imaging of the channels loaded with gold nanoparticles and still be thin enough to image. The gold nanoparticles seem to permeate throughout the crystal (Figure 2.26). As micrographs are a 2D representation of a 3D object it is often difficult to ascertain if the nanoparticles are spatially related. A crystal that is not perfectly flat inside of the embedding resin will make this even more difficult. To gain a better understanding of how the gold nanoparticles are oriented in 3D, electron tomography was utilized (Figure 2.27). The tomogram reveals a little bit more

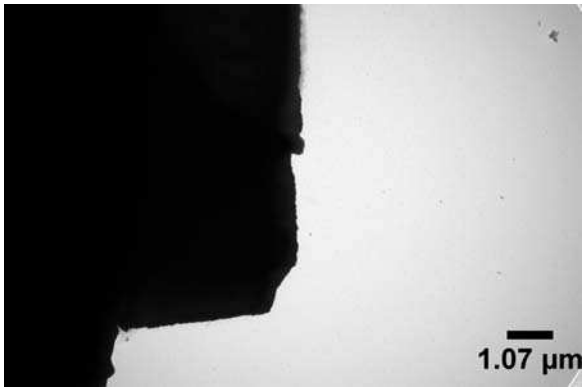

Figure 2.25. Representative micrograph of 2FGS crystal loaded with 10 nm AuNPs. These crystals tend to be too thick for electron microscopy.

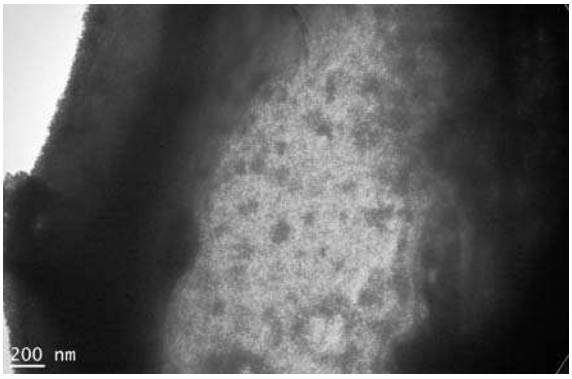

Figure 2.26. Representative micrograph of a sectioned 2FGS crystal loaded with 10 nm AuNPs.

information and provides some slight evidence that there may be gold nanoparticles stacking on top of each other inside the channels (Figure 20, panel B). However, the inherent electrostatic interaction of the ligands may be interfering with loading as well. There were, however, some issues of periodicity and electron density where there should not be any. This is seen in Figure 2.27, panel C, where it appears that there is a large amount of electron density that is linked together and does not appear to be a discrete particle. The second approach for imaging crystals that are too thick is simply to make the crystals smaller. This can be achieved through several methods; the first was to simply take crystals and shatter them so that the crystals would be thin enough to image; this was done by utilizing a method similar to Stevenson et al.[105], by vortexing crystals with 0.5 mm glass beads. While this method was successful in making the crushing the crystals to become small enough to image, the loss of predictable structure based on how the crystals are formed made it difficult to determine if the gold nanoparticles were in fact inside protein crystals or if the nanoparticles just tended to agglomerate together (Figure 2.28).

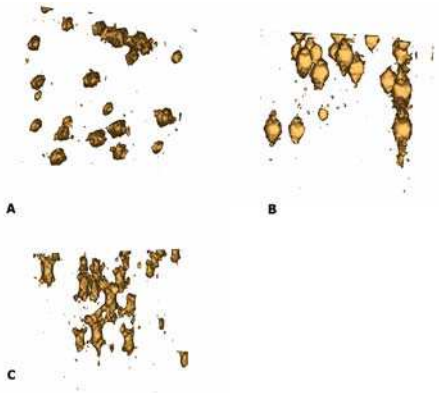

Figure 2.27. Tomogram reconstruction of data from sectioned 2FGS. (A) tomogram orientation down the face of the crystal, (B) tomogram rotated by 90° to reveal the electron density through the side of the crystal, (C) tomogram rotated 90° from (B) to reveal networking of electron density.

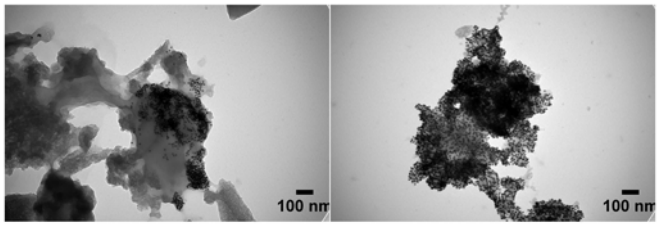

Figure 2.28. Representative transmission electron micrographs of 2FGS crystals loaded with 10 nm AuNPs that have been crushed by glass beads. The lack of structure as would be seen in a well ordered crystal renders it difficult to determine periodicity.

Our collaborators were able to control crystal size quite well and managed to grow microcrystals. The microcrystals still had a large issue with the nanoparticles coating the

entire surface of the crystal. In order to determine if the crystals grown were in fact thin enough to image through, unloaded crystals were placed onto TEM grids and imaged. This allowed imaging of the crystal to determine if they were thin enough for direct imaging. The crystals revealed that they were thin enough to image through and perhaps something more interesting. That inside of the crystals were very periodic electron dense spots (Figure 2.29). The electron dense spots appear 14-18 nm apart, which is close to what we would expect in a perfectly preserved crystal. However, the distances do not seem to be periodic, this may be caused by the high vacuum environment in the TEM warping the crystal. The spots are suspected to be large amounts of nickel ions concentrated around the His-Tags facing into the solvent channels. In order to have a clearer image of how these electron dense spots stack together, electron tomography was once again performed. Unfortunately, IMOD[106] had a difficult time aligning the image stack without any fiducial markers; regardless, aligning the image stack was attempted through other means. The alignment worked well enough to reveal that there appeared to be electron dense material inside a channel like structure (Figure 2.30). It was not possible, however, to gleam any information regarding the periodicity from the tomogram as the presumed channels are not electron dense enough and the alignment is not well

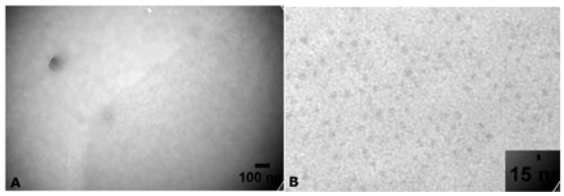

Figure 2.29. Transmission electron micrograph of a micro 2FGS crystal grown on a glow discharged C coated Au grid. Panel B is a magnified image of panel A and more clearly shows the periodic electron dense spots found in the crystal.

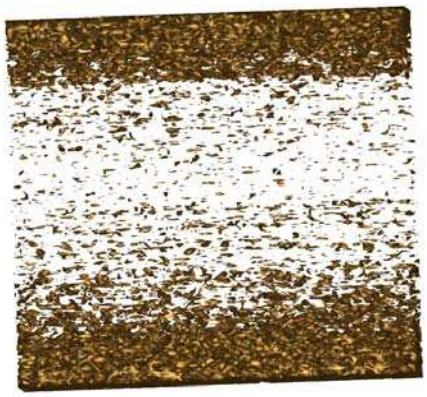

Figure 2.30. Tomogram reconstruction of tilt series from 2FGS microcrystal. Surfaces rendered at top and bottom are the crystal surface.

aligned enough. The problem with the alignment may be solved by utilizing a more electron dense substance than nickel or by further removing surface bound gold nanoparticles.

2.7. CONCLUSION

We have shown here the first structural evidence of incomplete exchange. By examining incomplete exchange, we gain a structural understanding of how exchange may occur. Our data suggests, as previous works do, that exchange occurs through an associative mechanism.[22,24,59,60] Our data also seem to suggest that the previously shown rates of exchange point to different Au atoms with differing environments. There is still a separate mechanism of exchange that needs to be teased out. It does, however, appear that only a single ligand is exchanged rather than an entire staple. From the work shown here, we hope to better understand the basics of how ligand exchange occurs and from that to leverage this understanding to better design tags and impart additional functionality. By understanding where ligands exchange on thiolate-monolater-protected gold nanoclusters, we can better understand the symmetry elements that might be present in single particle analysis which may aid in solving protein structures.

2.8. METHODS

2.8.1. STRUCTURAL AND THEORETICAL BASIS OF LIGAND EXCHANGE ON THIOLATE-MONOLAYER-PROTECTED GOLD NANOCLUSTERS

Materials. Unless specified, reagents were sourced from Fisher Scientific or Sigma-Aldrich and used without further purification. Tetrachloroauric (III) acid trihydrate ($HAuCl_4 \cdot 3H_2O$, 99.99%) was received from Alfa Aesar and Sigma-Aldrich and *p*-mercaptobenzoic acid (*p*-MBA)

(>95%) from TCI America. Nanopure H_2O was purified to a resistivity of 18.2 MΩ-cm using a Barnstead NANOpure water system.

Au_{102}(*p*-MBA)$_{44}$ synthesis. The AuMPCs used in this study were synthesized by modifications of a previously published method.[21] $HAuCl_4 \cdot 3H_2O$ (0.209g, 0.50 mmol, a nonmetal spatula should be used to weigh out $HAuCl_4 \cdot 3H_2O$) was dissolved in nanopure H_2O (19.0 mL, 0.028 M based on Au) in a 50 mL centrifuge tube. In a separate 50 mL centrifuge tube, *p*-mercaptobenzoic acid (0.292g, 1.89 mmol) was dissolved in a solution of nanopure H_2O (18.43 mL) and 10 M NaOH (0.57 mL, 5.70 mmol). The resulting *p*-mercaptobenzoic acid/NaOH solution should be 0.10 M based on *p*-mercaptobenzoic acid and 0.30 M based on NaOH. A 250 mL Erlenmeyer flask was equipped with a stir bar and nanopure H_2O (51.5 mL). In three separate beakers the following solutions were prepared: (a) 0.028 M $HAuCl_4$ solution (17.8 mL, 0.5 mmol, 1.0 equiv), (b) 0.10 M *p*-mercaptobenzoic acid/0.3 M NaOH (15.5 mL, 1.5 mmol, 3.0 equiv of *p*-mercaptobenzoic acid and 5.7 mmol, 11.4 equiv of NaOH) solution, and (c) MeOH (75 mL). Under stirring, the $HAuCl_4$ solution was poured into the 250 mL Erlenmeyer flask containing H_2O, immediately followed by the addition of the *p*-mercaptobenzoic acid/NaOH solution, the solution then turned from yellow to orange. MeOH was then added immediately afterward and the reactants were allowed to stir at room temperature for 1 h. During this time, the reaction turned from dark orange to light orange. After 1 h, pulverized solid $NaBH_4$ (20.8 mg, 0.55 mmol, 1.1 equiv) was added to the reaction which was allowed to stir at room temperature for 17 h. The reaction turned black upon the addition of the solid $NaBH_4$. The reaction was then transferred to a 1000 mL Erlenmeyer flask and precipitated with the addition of MeOH (750-850 mL) and 5 M NH_4OAc (35-45 mL). The reaction was then split into twenty 50 mL centrifuge tubes and

centrifuged at 4 °C for 10 min at 4000 rpm. The supernatants were decanted and the centrifuge tubes were inverted on a paper towel to drain the remaining liquid, then the pellets were then allowed to air-dry for 1 h. The precipitate in each conical was then dissolved in 50-150 μL of 2 M NH_4OAc and the black solution was combined into four 50 mL centrifuge tubes. The residual material in the centrifuge tubes was washed with 100-300 μL H_2O and then combined with the previously dissolved nanoclusters. MeOH was then added until the total volume in each conical was 40-48 mL and the centrifuge tubes were centrifuged again at 4 °C, 4000 rpm for 10 min. The resulting supernatant was removed and the precipitates were dried *in vacuo* at room temperature for at least 2 h. The nanoclusters were stored as a solid at -20 °C or resuspended in nanopure H_2O. Gel electrophoresis visualization was done with a 20% polyacrylamide gel (19:1 acrylamide/bisacrylamide) at 110 V for 2 h.

Ligand Exchange. The ligand site exchange reaction was carried out as follows: *p*-bromobenzene thiol (*p*-BBT) was dissolved in THF to prepare a stock concentration of 1.34 mg/mL (7.09 mM). Au_{102}(*p*-MBA)$_{44}$ (10 μL, 849 μM, 1.02 x 10^{-2} μmol) was transferred to a 1.5 mL tube, then 5 μL of the *p*-BBT stock solution (2:1 feed ratio of incoming thiol/gold = 2:44 feed ratio of incoming thiol/outgoing thiol) was added and the solution was vortexed for exactly 5 min before being quenched with 100 μL of isopropanol and 5 μL of 5 M NH_4OAc. (The solution pH was not explicitly controlled or measured in this reaction due to the impracticality of measuring pH for the small volume of reaction, and the desire to minimize the number of components in the reaction, knowing that both thiol and thiolate forms of sulfur are capable of exchange.) The 1.5 mL tube was then centrifuged at 14000 rpm for 10 min at rt. The supernatant was removed and the pellet was resuspended and washed in 10 μL of a 1:1 solution of nanopure H_2O and THF to

remove any remaining free thiol from solution. The solution was then precipitated again with the addition of 100 μL of isopropanol and 5 μL of 5 M NH_4OAc, then centrifuged at 14000 rpm for 10 min. The supernatant was removed and the pellet was dried *in vacuo*. The pellet was then resuspended in 10 μL nanopure H_2O and allowed to crystallize in hanging-drop well plates with the original mother liquor solution in which $Au_{102}(p\text{-MBA})_{44}$ was crystallized[21] (0.3 M NaCl, 0.1 M NaOAc, 40% MeOH, pH 2.5) over a period of 3-7 days. Once X-ray quality single crystals had formed, they were mounted onto nylon loops in a working mounting solution of 40 μL MeOH, 40 μL mother liquor and 15 μL 2-methyl-1,3-propanediol (MPD) as a cryoprotectant. Crystals were flash frozen and stored in liquid nitrogen prior to data collection.

Single Crystal Data Collection. Crystallographic data was collected on Beamline 4.2.2 at the Lawrence Berkeley National Lab Advanced Light Source. Typical wavelength was 0.827 Å. Data was collected to at least 1.5 Å (usually 1.2 Å) resolution for both ligand exchanged and control crystals. Approximately 250 ligand exchanged crystals were screened for initial diffraction. Of these, 10 were screened and 7 crystals could be confirmed by X-ray fluorescence measurements to contain Br. A total of 10 crystals resulting from ligand exchanged products were judged sufficient for complete data collection. Of those 10 crystals, 2 were confirmed to have both Br fluorescence and suitable diffraction quality to complete crystallographic refinement to locate the positions of Br.

Single Crystal Data Processing. The two crystals with adequate data for processing gave quantitatively similar results where we observed Br density attributed to ligand exchange in the PMBA2 and PMBA3 positions. For comparison, four crystals, which were not exchanged, were subjected to the same refinement strategy, where Br failed to refine at any position. The difficulty

Table 2.2. Summary of crystallographic data for $Au_{102}(p\text{-MBA})_{40}(p\text{-BBT})_4$ single crystals. [a]Number in parentheses represents the value for highest resolution shell. [b]Rsym = ΣΣ|Ij − ⟨I⟩|ΣΣj|Ij|. [c]R = (Σ||Fobs| − |Fcalc||)/(Σ|Fobs|). [d]Free R calculated from 5% of reflections chosen at random.

	ligand exchange	wild type
location for data collection	ALS BL 4.2.2	SSRL BL 11-1
symmetry group	C2/c	C2/c
unit cell dimension	30.33 Å x 57.05 Å x 38.18 Å	30.40 Å x 58.18 Å x 37.91 Å
resolution	1.5 Å	1.5 Å
wavelength	0.827 Å	0.979 Å
no. of unique reflections	9334	9234
completeness	95.8% (92.9%)	95.5% (94.1%)
<I/σI>	9.3 (2.55)	21.34 (12.49)
R_{sym} [b]	11.9% (50.0%)	7.28% (16.89%)
R [c]	8.40% (14.72%)	8.01% (9.14%)
free R [d]	18.30% (24.59%)	9.98% (11.22%)
GooF	1.08	1.037

heterogeneous crystals comprised of large, ligated metal nanoclusters is reminiscent of the experiences reported by others.[107] Data was reduced with XDS[80] and XPREP (version 6.12; Bruker AXS: Madison, WI, 1999). Static substitutional refinement was carried out by attempting refinement of Br atoms in place of COOH groups for all 22 ligand positions in both control and experimental crystals. This was followed by anisotropic refinement of Br in four of the ligand positions to fully eliminate all but two locations in the exchange position and none in the wild-type crystals (Table 2.1). Final refinement statistics from SHELX[81] for the best ligand exchange crystals were R_1 = 0.0840, R_1 (free) = 0.1830 for 5512 reflections, R_1 = 0.1420 and R_1 (free) = 0.2459 for all 9650 reflections.

Computational Methods. For the computational modeling of ligand exchange in the $Au_{102}(SR)_{44}$ nanocluster, we used the density functional theory (DFT) as implemented in the real-space code-package GPAW[108,109] and PBE[110] as the exchange-correlation functional. To minimize

the number of calculations in the computational study, we replaced the *p*-MBA ligands with simple SH groups in most of our calculations and used methane thiolate as the model for the incoming ligand. For completeness, reaction energies were also estimated using the actual *p*-BBT/*p*-MBA ligands. In the structure optimization we used 0.2 Å grid spacing and 0.05 eV/Å convergence criterion for the maximum forces acting on atoms in nanoclusters with SCH_3/SH ligands, and a 0.1 eV/Å criterion for the nanoclusters with *p*-BBT/*p*-MBA ligands.

Reaction paths for the ligand-exchange (shown in Figure 5) were solved using constrained structural optimization with a fully dynamic system, that is, with no fixed atoms. The GPAW setups for Au include scalar-relativistic corrections. The starting configuration for each step was taken from the optimized geometry of the previous step. As a reaction coordinate we used, in the first step of the proposed reaction coordinate, the distance from the sulfur atom of the incoming thiol/thiolate to the gold atom of the active staple, and in the second step, we employed the distance from the sulfur atom of the outgoing thiol/thiolate to the core Au-atom binding site of the staple. The above-mentioned S-Au distances were gradually varied and were then fixed for the structural optimization of each step of the reaction. Additional calculations on plausible reaction paths were done where atoms beyond 6 Å from the active exchange site were fixed.

2.8.2. STRUCTURAL BASIS OF LIGAND EXCHANGE ON $Au_{25}(SR)_{18}$

Chemicals. Tetrachloroaurate trihydrate (Sigma-Aldrich, ACS Reagent ≥49.0% Au basis), Phenylethanethiol (Sigma-Aldrich, ≥99%), 4-bromobenzenethiol (Sigma-Aldrich, 95%), ethanol (Pharmco-aaper, 200 proof), tetraoctylammonium bromide (Fluka, ≥99.0%), tetrahydrofuran

(Fisher, HPLC grade ≥99.9%), toluene (Fisher, HPLC grade ≥99.9%), sodium borohydride (Sigma-Aldrich, ≥98%), dichloromethane (Fisher, ≥99.9%), and hexanes (Fisher, ≥99.9%) were purchased commercially and used as is.

Synthesis of $Au_{25}(SC_2H_4Ph)_{18}$ (PET). $Au_{25}(PET)_{18}$ was synthesized by following pre-established procedures as described briefly here.[61] $HAuCl_4 \cdot 3H_2O$ (1.01 mmol, 400 mg) and tetra-n-octylammonium (1.14 mmol, 624 mg) bromide (TOAB) were codissolved in 28 mL tetrahydrofuran (THF) in an Erlenmeyer flask with stirring. After 15 minutes, phenylethanethiol (PET) (5.36 mmol, 0.718 mL) was added to the solution. The solution was allowed to stir for a minimum of 12 hours, until the solution became colorless. In a separate flask, $NaBH_4$ (10.24 mmol, 386 mg) was dissolved in 10 mL Nanopure water (18.2 MΩ-cm) and stirred for 1 hour at 0° C before addition into the solution containing $HAuCl_4 \cdot 3H_2O$, PET and TOAB. Upon the addition of $NaBH_4$, the solution was allowed to stir for an additional 48 hours. The solution was filtered and dried. The product was redissolved in toluene and transferred to a separatory funnel and extracted with nanopure water five times. The toluene layer was collected and dried under reduced pressure, then thoroughly washed with methanol to give $Au_{25}(PET)_{18}^-$. This product was then run down a silica column in 1:1 DCM:hexanes to give $Au_{25}(PET)_{18}^0$.

Ligand Exchange on $Au_{25}(PET)_{18}$. Exchange was performed by dissolving five equivalents of *p*-BBT with one equivalent of $Au_{25}(PET)_{18}^0$ in DCM. This mixture was allowed to shake for seven minutes. Ethanol was added to the mixture to precipitate out the exchanged clusters while allowing the excess *p*-BBT to remain in solution. The solution was decanted to remove excess *p*-BBT and clusters that were over exchanged. Finally, the precipitate was collected and dried at 560 mbar at 25 °C.

Crystallization of Exchange Products. Crystals were formed by dissolving exchanged $Au_{25}(PET)_{18}^0$ in toluene with ethanol added as the anti-solvent then allowed to slowly crystallize at -20°C. Dark square crystals formed after approximately seven days.

Data Collection. Data were collected at the ALS beamline 4.2.2 with the NOIR-1 MBC detector at a distance of 100nm at 13499.998eV (0.918 Å). Data was taken for 180° at 1°/s. Data were integrated and corrected through XDS.[80] Data were refined through XPREP (v. 6.12; Bruker AXS: Madison, WI, 1999.) and run through SHELXS[81] which output the $Au_{25}S_{18}$ core. The ligands were built through q peak analysis in XSHELL.[81] The space group was determined to be P$\bar{1}$ which is different than the Pccn space group reported for the neutral charge state of $Au_{25}(PET)_{18}$.[111] This is due to the presence of the toluene that can be seen in the asymmetric unit.

2.8.3. EFFECT OF A CHIRAL LIGAND LAYER ON CLUSTER CHIRALITY[86]

Synthesis of camphor-10-thiol. (1R)-(-)-10-camphorsulfonic acid (10.00g, 43 mmol) was placed in a round-bottomed flask with a reflux condenser and stir bar. 3.5 equivalents of thionyl chloride (11.00 mL, 151 mmol) were added. The reaction was stirred for 10 minutes at room temperature then, refluxed for 2 h. After cooling to room temperature, excess thionyl chloride was removed in vacuo at 20 °C for 20 minutes. 5 mL of toluene were added then removed in vacuo followed by washing with another 5 mL of

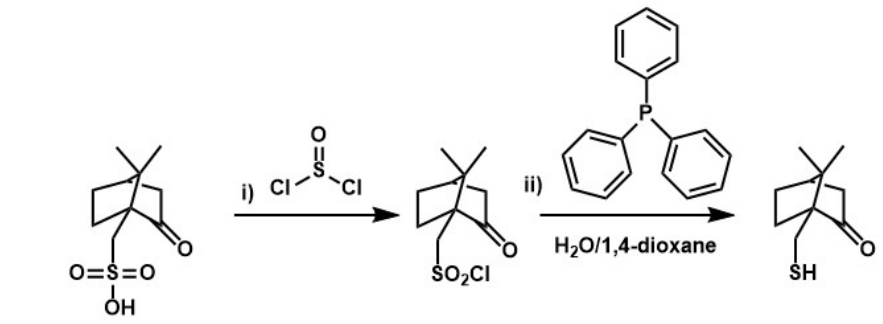

Scheme 2.1. Reaction scheme to form camphorthiol

toluene and removal in vacuo. The product was then dried in vacuo at 30 °C for 15 minutes (571.5 mmHg) to give a yellow solid. (6.753 g)

^{1}H NMR ($CDCl_3$, 300 MHz): δ = 0.97 (s, 3H), 1.18 (s, 3H), 1.48-1.57 (m, 1H), 1.77-1.86 (m, 1H), 1.98-2.08 (d, 1H), 2.09-2.24 (m, 2H), 2.38-2.57 (m, 2H), 3.72-4.41 (dd, 2H) ppm.

Synthesis of camphorthiol. (1R)-(-)-camphorsulfonic acid chloride (4.871 g) was placed in a round-bottomed flask with a reflux condenser and stir bar. Next, 3 equivalents of triphenylphosphine (amount) and water/1,4-dioxane (10:40 mL) were added. The solution was refluxed for 2 h. After cooling to room temperature, the reaction mixture was extracted with cyclohexane (3 times). The combined organic extracts were washed with water and dried over Na_2SO_4. The solvent was removed in vacuo (571.5 mmHg) at 25 °C for 20 minutes to yield a slightly yellow solid. Further purification was achieved by column chromatography (cyclohexane:EtOAc 40:1) over silica gel (25 mm x 25 mm x 350 mm column volumn (l x w x h)) with 2.5 g SiliaFlash 40-63 µm (230-460 mesh) 60 Å Irregular Silica to give a white solid (0.2042 g).

^{1}H NMR ($CDCl_3$, 300 MHz): δ = 0.907 (s, 3H), 1.107 (s, 3H), 1.359-2.094 (m, 7H), 2.318-2.404 (m, 2H), 2.835-2.904 (pq, 1H)

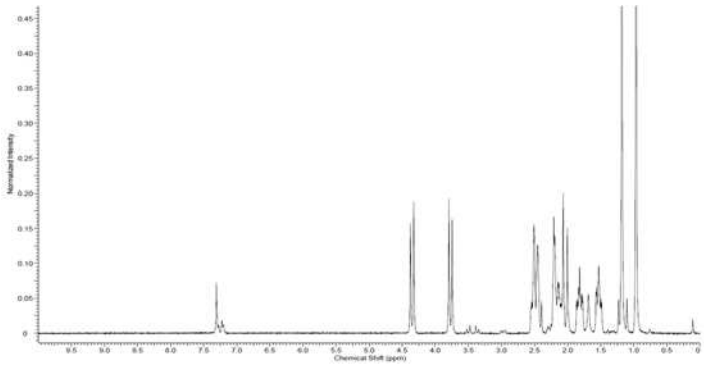

Figure 2.31. NMR of camhor-10-thiol.

Ligand Exchange on $Au_{25}(PET)_{18}$. Exchange was performed by dissolving five equivalents of camphorthiol with one equivalent of $Au_{25}(PET)_{18}^0$ in CH_2Cl_2. This mixture was

allowed to mix for seven minutes on a VWR 40000-300 Rocking Platform at a tilt angle of 8° and 20 tilts/minute. Ethanol was then added to the mixture to precipitate out the exchanged clusters while allowing the excess camphorthiol to remain in solution. The precipitate was collected and dried.

Crystallization of Exchange Products. Crystals were formed by dissolving 4 mg of exchanged $Au_{25}(PET)_{18}^{0}$ in 1 mL of toluene with 3 mL of ethanol layered carefully layered onto the toluene layer then allowed to slowly crystallize at -20°C for three days.

2.8.4. EFFECTS OF A BIDENTATE LIGAND ON THIOLATE-MONOLAYER-PROTECTED GOLD NANOCLUSTERS[88]

Synthesis of 1. An acetonitrile solution (25 mL) of 3-bromobenzenethiol (3.702 g), diisopropyletylamine (4.07 mL) and 1-chloromethyl methyl ether (MOM-Cl) (2.22 mL) was stirred at 0 °C for 3 h. The solution was extracted with 50 mL ethyl acetate twice, washed with 10 mL of brine and then evaporated under

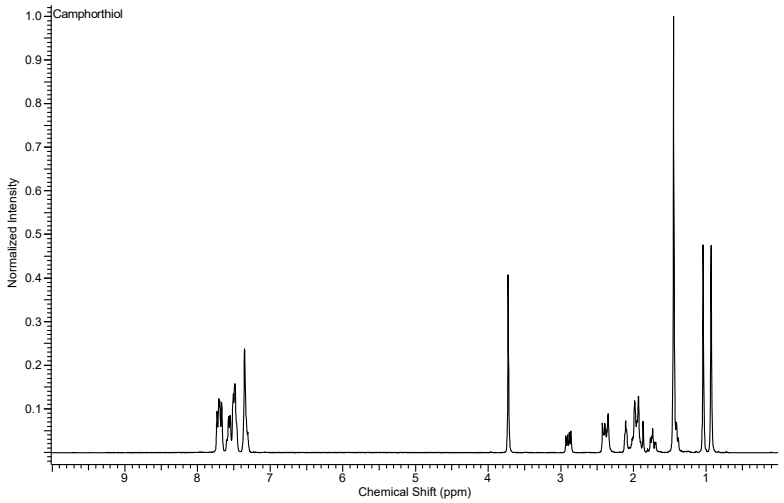

Figure 2.32. NMR of camphorthiol

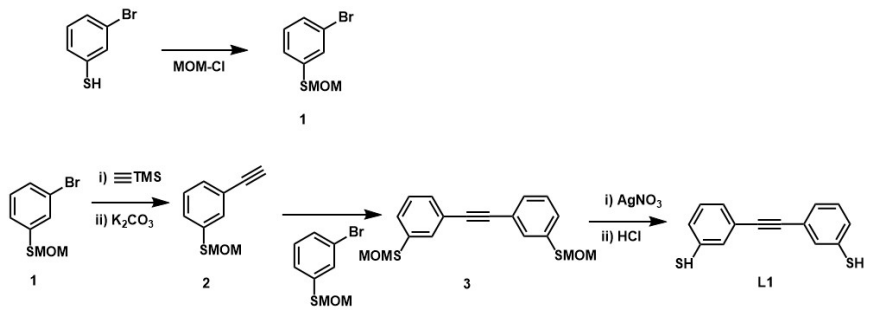

Scheme 2.2. Reaction scheme for L1.

reduced pressure (571.5 mmHg) for 30 minutes to obtain a yellow oil (1.723 g)

Synthesis of 2. A mixture of **1** (0.75 g), trimethylsilylacetylene (0.75 mL), CuI (0.5 mol %), $Pd(PPh_3)_2Cl_2$ (1 mol %), PPh_3 (1 mol %) and triethylamine (TEA) (20 mL) was degassed in an 100 mL round-bottomed flask by bubbling with N_2 for 30 min. The solution was stirred overnight at 90 °C under a N_2 atmosphere and then extracted with 25 mL ethyl acetate twice, then washed with 30 mL of brine once, and the organic phase was dried with ~0.5 g Na_2SO_4 and evaporated under reduced pressure (571.5 mmHg) for 30 minutes. The residue was purified by silica column chromatography, using hexane/ethyl acetate (99:1) as an eluent, to yield **2** as a pale yellow solution (0.7033 g). **2** was further purified by dissolving **2** into a THF/MeOH suspension (1:1) (3 mL) of K_2CO_3 (80 mg), stirred O.N. and washed with brine and dried with ~0.7 g Na_2SO_4 to yield 0.4893 g of product.

Synthesis of 3. A TEA solution (20 mL) of **2** (0.14 g) and **1** (0.27 g), CuI (0.5 mol % **2**), $Pd(PPh_3)_2Cl_2$ (1 mol % **2**) and PPh_3 (1 mol% **2**) was degassed in a 50 mL round-bottomed flask by bubbling with N_2 for 30 min. The solution was stirred overnight at 90 °C under a N_2 atmosphere and was extracted with ethyl acetate, washed with brine, dried by Na_2SO_4 and evaporated under reduced pressure. The residue was purified by silica column chromatography using a column

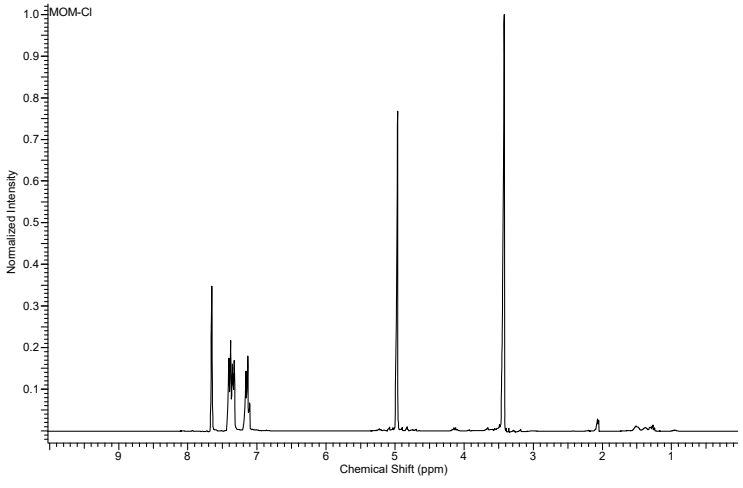

Figure 2.33. NMR of **3**.

with dimensions 25 mm x 25 mm x 350 mm (l x w x h), filled with 2.5 g SiliaFlash 40-63 µm (230-460 mesh) 60 Å Irregular Silica, using hexane/ethyl acetate (9:1) as an eluent to afford **3** as a pale yellow oil (0.0752 g).

^{1}H NMR ($CDCl_3$, 300 MHz): δ = 3.46 (s, 6H), 4.99 (s, 3H), 7.23-7.64 (m, 8H)

Synthesis of L1. The protected precursor **3** (0.3 g) was suspended in a CH_2Cl_2/methanol (1:1) solution (50 mL) of $AgNO_3$ (0.34 g) and stirred vigorously overnight. A yellow precipitate formed, which was isolated by gravity filtration using Whatman Grade 413 filter paper. Next, 20 mL 6 M HCl was added to the filtrate along with 20 mL CH_2Cl_2. The filtrate, 20 mL 6 M HCl and 20 mL CH_2Cl_2 solution was stirred for three hours in the dark. The CH_2Cl_2 layer was separated, washed with water and brine, dried over Na_2SO_4, and evaporated to yield **L1** as a pale yellow solid (0.074 g).

^{1}H NMR ($CDCl_3$, 300 MHz): δ = 3.48 (s, 2H), 7.17-7.43 (m, 8H)

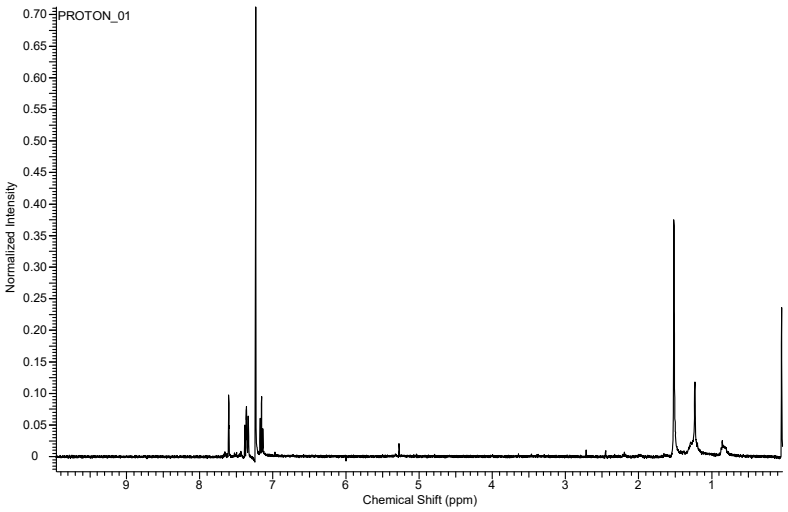

Figure 2.34. NMR of L1.

2.9.5. EFFICACY OF GOLD NANOPARTICLE BINDING TO A PROTEIN CRYSTAL SCAFFOLD

Synthesis of $Au_{25}(SG)_{18}$. $Au_{25}(GS)_{18}$ was synthesized via a modified procedure as briefly described here.[28] Glutathione (308.1 mg, $1x10^{-3}$ mol) was added to a solution of $HAuCl_4$ (98.7 mg, $2.5x10^{-4}$ mol) in 50 mL methanol. The solution was stirred until the solution formed a cloudy, yellow suspension, but after approximately five minutes of magnetic stirring the solution turned

to clear and colorless. This solution was cooled at 0° C while stirring for 30 minutes. To this 0° C solution, a solution of $NaBH_4$ (94.3 mg, $2.5x10^{-3}$ mol) in 12.5 mL 5 ° C H_2O was added rapidly with stirring. The reaction was removed from the ice bath and allowed to stir for one hour at room temperature before the precipitate was spun down in 200 µL 5M NH_4OAc and 49 mL MeOH at 4000 rpm. The supernatant was discarded and the precipitate was washed twice more with 200 µL 5M NH_4OAc and 49 mL MeOH and then dried. Gel purification was performed on $Au_{25}(GS)_{18}$ on a 24% polyacrylamide gel.[93,94] $Au_{25}(GS)_{18}$ was extracted from the gel in H_2O and precipitated in 49 mL MeOH and 200 µL 5M NH_4OAc and dried using a lyophilizer set at -49 °C and 0.070 mbar (0.05 mmHg).

Synthesis of 9 nm Gold Nanoparticles. AuNPs were synthesized using a modified procedure.[95] A total of 1 mmol of $HAuCl_4 \cdot 3H_2O$ and 5 mL (10 mmol) of oleylamine (>70%) were mixed with 50 mL toluene in a 100 mL round-bottomed flask. Under an argon atmosphere, the solution was heated to 65 °C and stirred for 6 h. The solution was cooled to room temperature then 50 mL of ethanol were added immediately. This solution was then centrifuged at 4000 rpm for 10 minutes. The supernatant was discarded and the pellet was redispersed in 10 mL of heptanes. Next, 2 mL of the heptane dispersion of the AuNPs were mixed with 10 mL of heptane, and 5 mL 3-mercaptopropionic acid (3-MPA) in an open 50 mL round-bottomed flask. This solution was stirred overnight at room temperature. The solution was centrifuged at 4000 rpm for 10 minutes. The precipitate was then washed with 50 mL

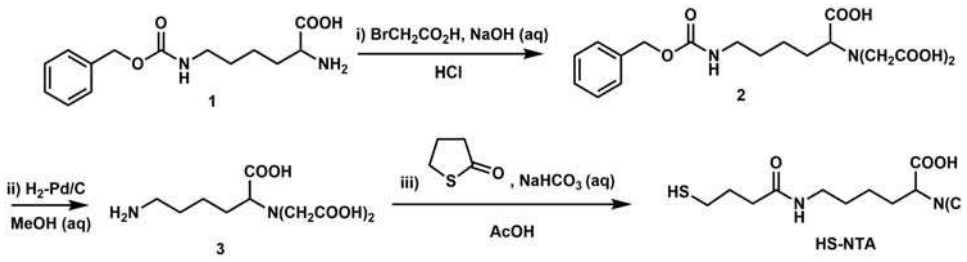

Scheme 2.3. Reaction scheme of HS-NTA

acetone, centrifuged at 4000 rpm at 25 °C for 5 minutes. The washing procedure was done for a total of three times. The final pellet was dissolved in 10 mL deionized H_2O.

Synthesis of HS-NTA[26]

(1S)-N-(5-Carbobenzyloxyamino-1-carboxypentyl) iminodiacetic Acid (2). This ligand was synthesized using the previously published synthesis[26] as briefly described here. Bromoacetic acid (4.17 g, 0.03 mol) was dissolved in 15 mL 2 M NaOH. This solution was cooled to 0° C. To this a solution of N^{ε}-Cbz-L-lysine (4.2g, 0.015 mol) in 22.5 mL 2 M NaOH was added drop-by-drop and stirred for two hours at 0° C. Stirring was continued overnight at room temperature. This solution was then heated to 50 °C for two hours, after which, 1 N HCl (45 mL) was added to the cooled solution. The precipitate was gravity filtered using Whatman Grade 413 filter paper and dried in a lyophilizer at -49 °C and 0.070 mbar (0.05 mmHg), to afford 1.5776 g of a crude white solid (**2, triacid**). ^{1}H NMR (DMSO-d_6, 300 MHz): δ = 1.38-1.59 (2m, 6H), 2.96 (m, 2H), 3.44 (m, 5H), 5.00 (s, 2H), 7.34 (m, 5H)

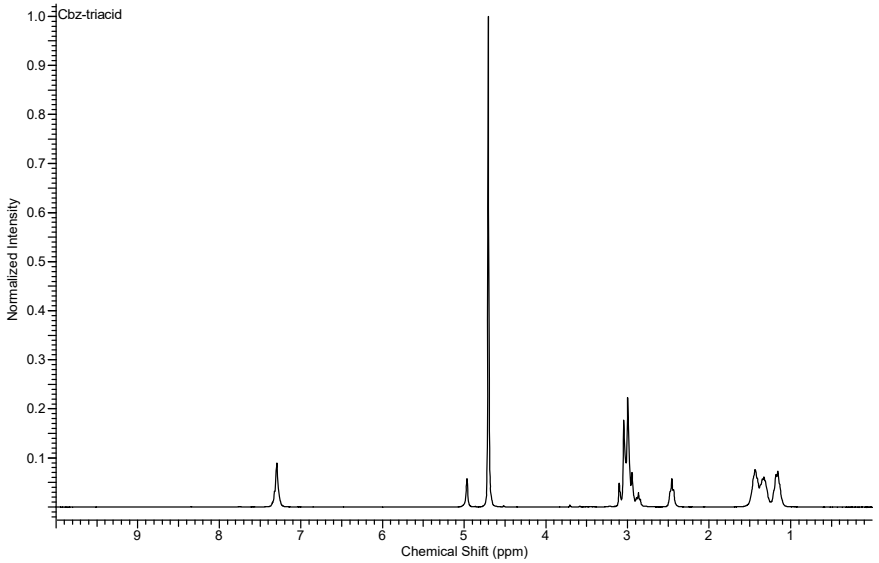

Figure 2.35. NMR of (1S)-N-(5-carbobenzyloxyamino-1-carboxypentyl)iminodiacetic acid

(1S)-N-(5-Amino-1-carboxypentyl)iminodiacetic Acid (3). A solution of **2** (6.8 g, 0.017 mol) in 95 mL MeOH/5 mL H_2O and a spatula tip full of 5% Pd/C catalyst was in a 500 mL round-bottomed flask stirred with H_2 (100 kPa) bubbling into the 500 mL round-bottomed flask with a

septa stopper at 25° C for 24 hours. Product was filtered through ~1g of celite to remove the catalyst. The solvents were evaporated to give a colorless white paste (2.486 g).

^{1}H NMR (D_2O, 300 MHz): δ = 1.54-1.76 (2m, 6H), 2.85 (t, 2H), 3.77 (m, 5H)

(1S)-N-[5-[(4-Mercaptobutanoyl)amino]-1-carboxypentyl]iminodiacetic Acid (HS-NTA). The amino derivative (**3,** 1g, 0.0038 mol) was dissolved in 10 mL H_2O with $NaHCO_3$ (1g, 0.0119

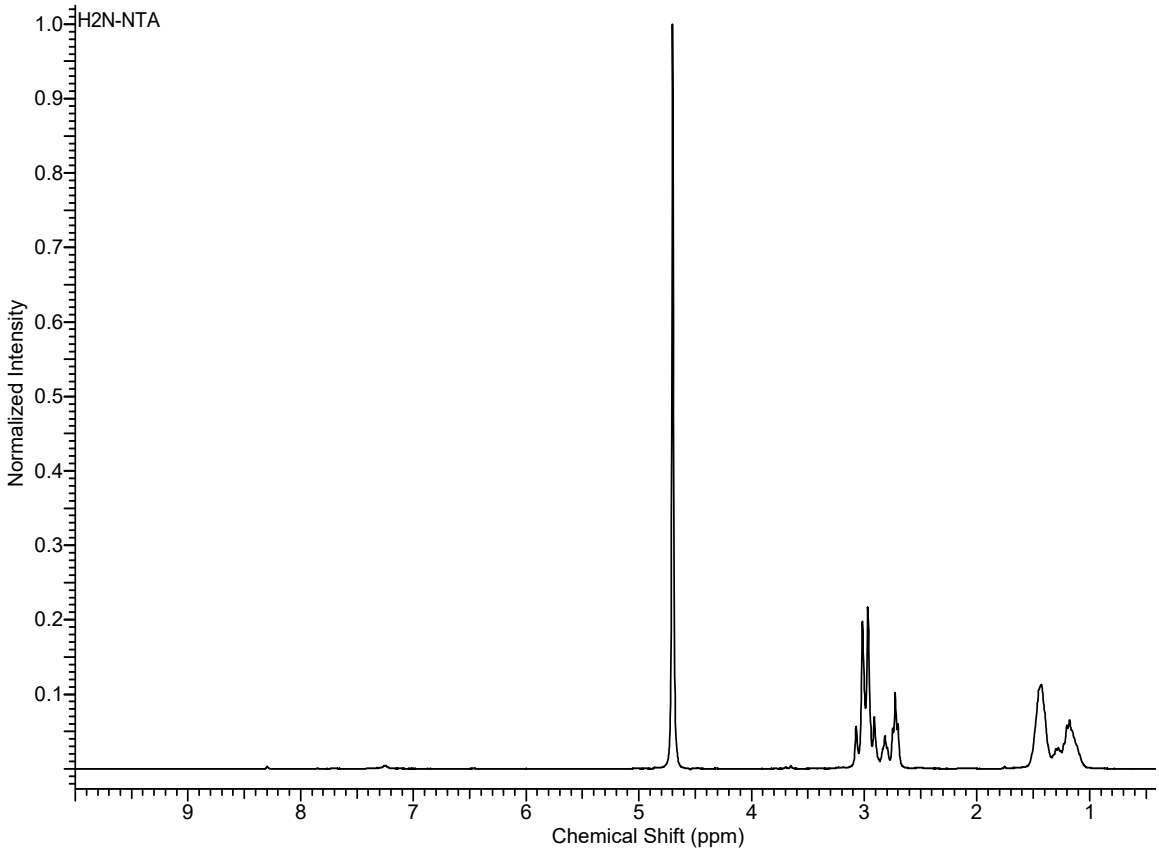

Figure 2.36. NMR of (1S)-N-(5-amino-1-carboxypentyl)iminodiacetic acid.

mol) and 4-butyrothiolactone (0.6g, 0.0059 mol) in a 100 mL round-bottomed flask and stirred for 15 h at 72 °C. The resultant mixture was acidified to pH 3 with glacial acetic acid and concentrated under reduced pressure (571.5 mmHg) at 35 °F. The crude product was crystallized in 50 mL absolute ethanol, gravity filtered through Whatman Grade 413 filter paper and washed

with 10 mL absolute ethanol followed by 10 mL pentanes, and dried under vacuum to give a light beige solid (0.122 g) (Scheme 3).

^{1}H NMR (D_2O, 300 MHz): δ = 1.42-1.74 (2m, 8H), 2.21 (t, 2H), 2.4 (t, 2H), 3.06 (t, 2H), 3.62 (m, 5H)

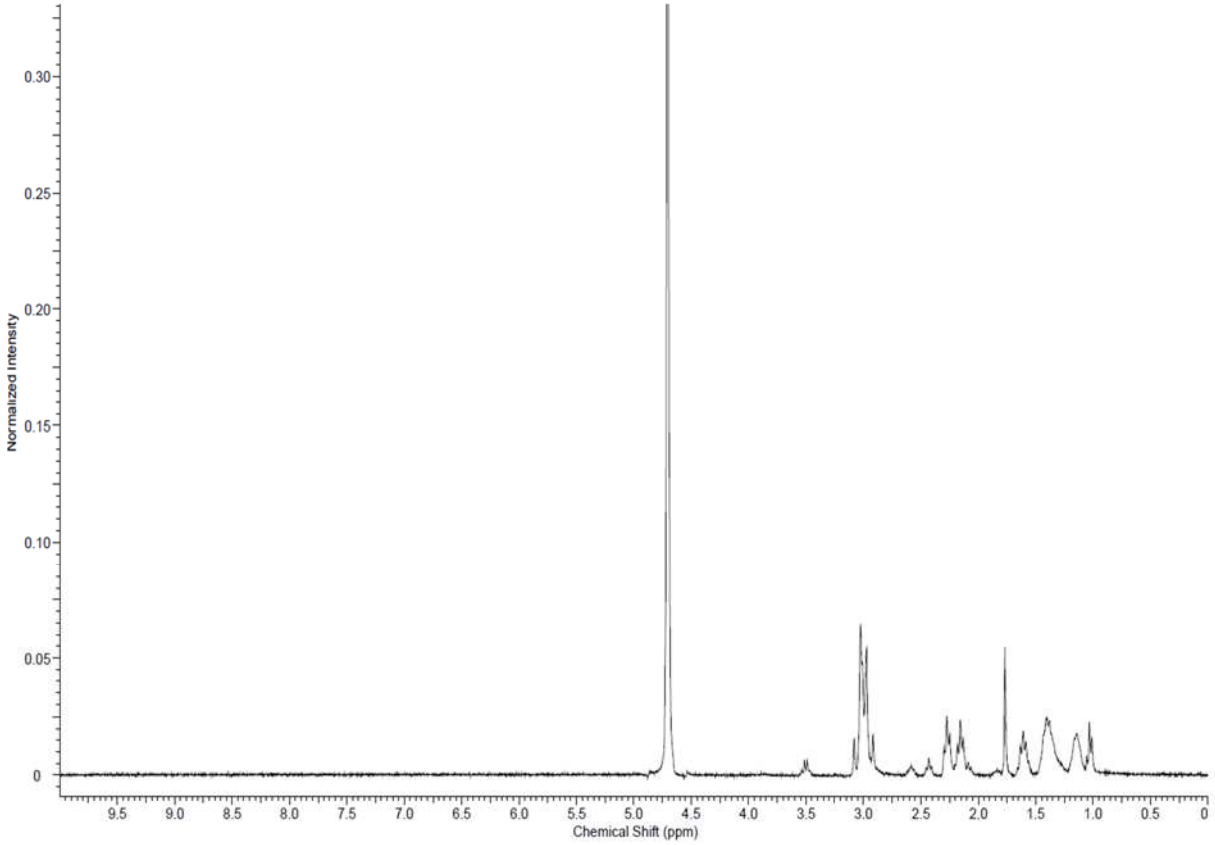

Figure 2.37. NMR of HS-NTA

Ligand Exchange. The exchange reaction consisted of 5 mL of a solution of 3-MPA coated AuNPs containing 3 mg of dried particles resuspended in 10 mL deionized water and 50 mg of tetramethylammonium hydroxide (TMA) and 50 mg of HS-NTA. The ligand exchange was allowed gently rocked for 5 minutes at a 5° tilt at 20 tilts/minute. After five minutes, the reaction was quenched with 50 mL ethanol. The solution was centrifuged for 30 minutes at 4000 rpm. The resulting precipitate was redispersed in deionized H_2O and washed again with ethanol. The precipitate was then dried and stored.

Sectioning. 2FGS crystals were placed into liquid Epon resin then solidified by staff at the Boulder Laboratory for 3-D Electron Microscopy of Cells. A brief procedure is listed here. Crystals were placed into 20 mL of a solution of Epon:acetone at a ratio of 1:4 (v/v) overnight. This was then placed into 20 mL of a solution of Epon:acetone at a ratio of 1:2 (v/v) for eight hours. This was then transferred into 20 mL of a solution of Epon:acetone at a ratio of 3:4 (v/v) overnight. The crystals were then transferred to 20 mL of 100% Epon for eight hours. Then transferred again into 20 mL of 100% Epon overnight. Finally this was transferred to 20 mL of Epon with a 1:1 mix of 2,4,6-Tris(dimethylaminomethyl)phenol (DMP-30) for six hours. This was then transferred to 20 mL of fresh Epon with DMP-30 and placed into a BEEM capsule and placed into a 60 °C oven. Epon samples were sectioned on a Leica Ultracut UCT. Electron tomography data was taken on a FEI Tecnai F-30 operating at 300 kV.

Electron Tomography. Crystals of CJ1 were incubated in a solution of 5 mM $NiCl_2$ for 5 minutes. The crystal was then moved into water to remove excess nickel, then into a solution containing 1 mg/ml 10 nm AuNP with S-NTA exchanged on and allowed to soak for 5 minutes. The crystals were then moved back into water to remove excess 10 nm AuNP. The CJ1 crystals was then pipetted onto glow discharged (ambient atmosphere) 200 mesh carbon coated Cu grids. Grids were loaded into a JEOL JEM-1400 operating at 100 kV in a high tilt holder. Grids were screened for crystals or fragments of crystals thin enough to image through. Serial tilt image stacks were taken using SerialEM[112] from +60° to -60°. Serial tilt image stacks were processed through IMOD[10,106] to process image stacks into 3D reconstructions. Reconstructions were then visualized in IMOD to reveal 3D orientation of AuNPs in crystals.

CHAPTER 3. BIOGENIC INORGANIC NANOPARTICLES

3.1. INTRODUCTION

A *grand challenge* in biogenic inorganic nanoparticle synthesis is a clonable nanoparticle. Specifically, the goal here is a *single* clonable polypeptide sequence that mediates the self-contained-biogenic- formation of an inorganic nanoparticle from inorganic salt precursors. Just as the clonable fluorophore, green fluorescent protein (GFP), is widely used for clonable contrast in biological optical microscopies,[113] a clonable inorganic and electron-dense nanoparticle is expected to find widespread use for cellular contrast in biological electron microscopy. In each case facile genetic methods for concatenating DNA encoding a protein sequence to the DNA sequence of a native cellular protein underlie the utility of clonable microscopy contrast. Expression of the resulting chimeric protein places a contrast marker alongside every instance of the native protein, enabling localization of the protein chimera in micrographs.

A clonable nanoparticle requires a polypeptide that integrates three distinct chemical activities. One activity is inorganic ion reduction or oxidation, converting soluble (ideally bioavailable and nontoxic) inorganic ions to insoluble (nanoparticulate) species. Second, the resulting inorganic nanoparticle must be retained by the polypeptide. Third, the size of the resulting nanoparticle must be large enough to identify unambiguously in a micrograph that includes biological structure, while also being small enough to minimize perturbation of cell biology and to reduce the shadow-casting that obscures biological information. An ideal size is suggested as 5 nm diameter. So far, there is no widely adopted clonable contrast marker in biological electron microscopy.

Both naturally occurring proteins as well as peptides isolated from libraries are investigated as candidate clonable nanoparticles. Naturally occurring proteins investigated include most prominently ferritin and metallothionein. In the case of the iron-storage capsule protein ferritin,[35] the requirement of 24 subunits with a total mass of nearly 0.45 MDa[114] may limit its use. Metallothionein coordination of Au(I) or Au(III) based ions is also proposed,[38,115,116] but these methods are not widely adopted in biological electron microscopy. This is perhaps because the Au(I) precursors are sparingly soluble in water and Au(III)-based coordination compound precursors are easily reduced by proteins,[117–119] buffers,[120,121] and other biomolecules encountered in a cellular environment.[122–125]

Proteins associated with magnetosomes such as mms6 are also initially attractive for forming clonable iron oxides.[126] However, a recent study shows that cloning of a minimal set of magnetosome-associated genes into a new host cell results in undesired, membrane-encapsulated iron oxide nanoparticles.[127] Such a membrane would clearly disrupt the function of a clonable nanoparticle, by adding size and possibly membrane sequestering proteins tagged for study.

Another investigated source of a polypeptide satisfying the clonable nanoparticle criteria is directed evolution. Directed evolution methods have already identified several DNAs,[128–130] RNAs,[131,132] and peptides[42,45,133] that mediate inorganic nanoparticle formation. In fact, early reports suggested that some library-derived peptides possessed the three desired activities of reduction, retention and size control.[45,134] Subsequent studies revealed that the buffers such as HEPES[121] or other Good's Buffers,[120] in which the selections were executed, reduced the inorganic precursors.[135] The role of the evolved biomolecules is to cap the nanoparticles resulting

from buffer reduction of metal ions, enforcing size and shape control. One of the best studied systems, the A3 peptide,[51,134,136–138] shows a preference for a size where the radius of curvature of the nanoparticle matches the curvature naturally adopted by the peptide.[136] Thus, while inorganic nanoparticle binding (retention) and size control are now well-established for peptides and polynucleotides, there are no well-established examples of peptides that catalytically or stoichiometrically reduce metal ions for the production of particles large enough to find use in biological electron microscopy.

Enzymes that reduce or oxidize metal ions into insoluble forms represent another class of biomolecule candidate for a clonable nanoparticle, and are the least extensively investigated. Such enzymes include silicateins,[139,140] silicatein homologous proteases,[141] and metal[142,143] and metalloid[144–146] reductases implicated in detoxification processes. Resulting nanoparticle size is regulated when the product is retained, by encapsulating proteins such as DPS[147] or ferritin.[147] Alternatively, enzymes release or turn over their products, allowing them to diffuse from the site of synthesis.[141,148] Notably, there are no well-established examples of intracellular particles wherein the inorganic portion of the particle is exposed to cytosol. [149] The research found within this chapter attempts to better understand this phenomenon and to utilize these inorganic nanoparticles as a means to give proteins of interest more electron constrast.

Portions of the work presented in the following chapter have been previously published in the journal Nanoscale (Progress Toward Clonable Inorganic Nanoparticles.)[149] A movie showing the full reconstruction can be found as a supplementary file in the reference provided. The full reconstructed dataset can be found on the Electron Microscopy Data Bank (EMDB)'s website (ID. 2939).

3.2. A NOVEL PEPTIDE CAPABLE OF FORMING IRON-OXIDE NANOPARTICLES

Our first attempt at designing a potential tag was to explore a large sequence space through the usage of commercially available phage display kits. We first synthesized water insoluble nanoscale magnetic iron oxides (MIO) as a substrate for phage selection. A previously established synthetic approach was used.[150] The synthetic product possessed bulk magnetic properties (i.e., migration in solution toward a permanent magnet) and powder x-ray diffraction produces a diffraction pattern consistent with magnetite (Fe_3O_4) and maghemite (Fe_2O_3) (Figure 3.1). Powder X-Ray diffraction cannot reliably differentiate between magnetite (Fe_3O_4) and maghemite (γ-Fe_2O_3)[151]; thus, there is ambiguity in the assignment of the phase of the material.

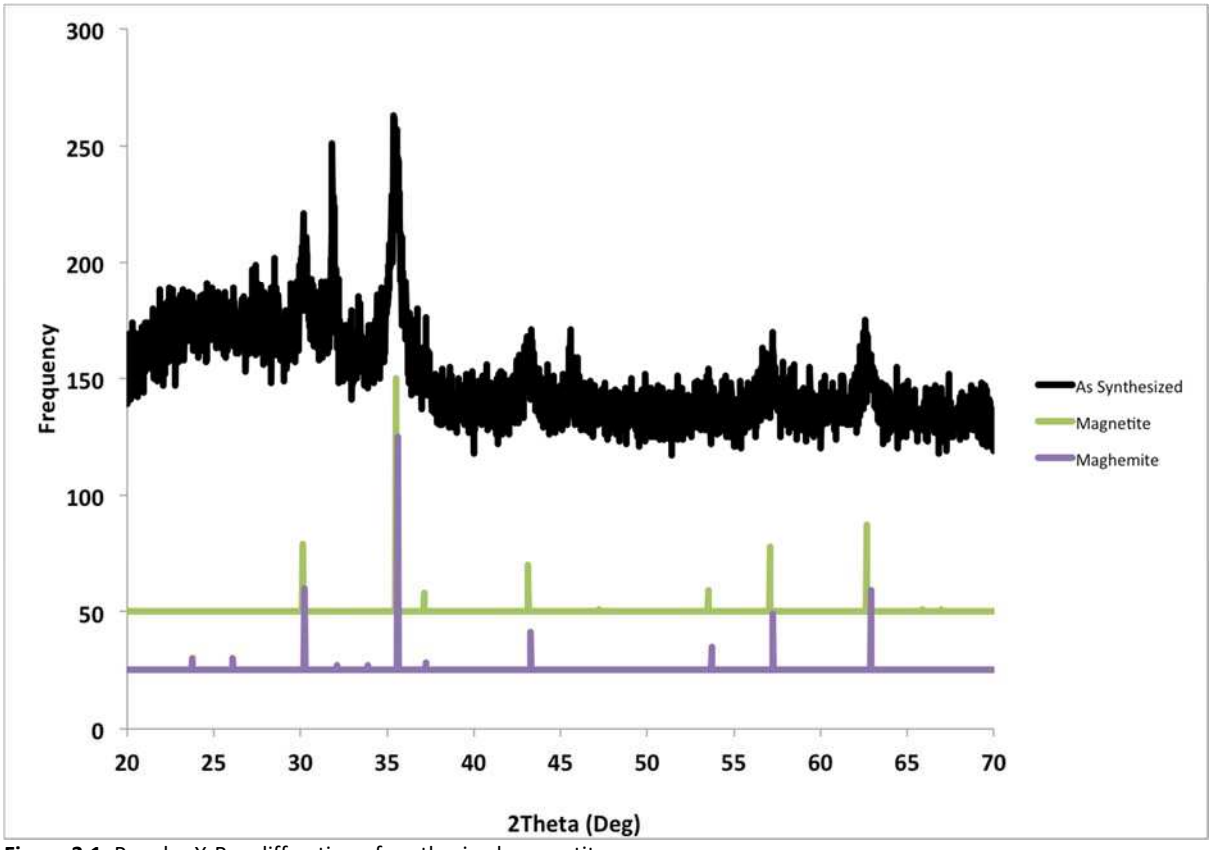

Figure 3.1. Powder X-Ray diffraction of synthesized magnetite.

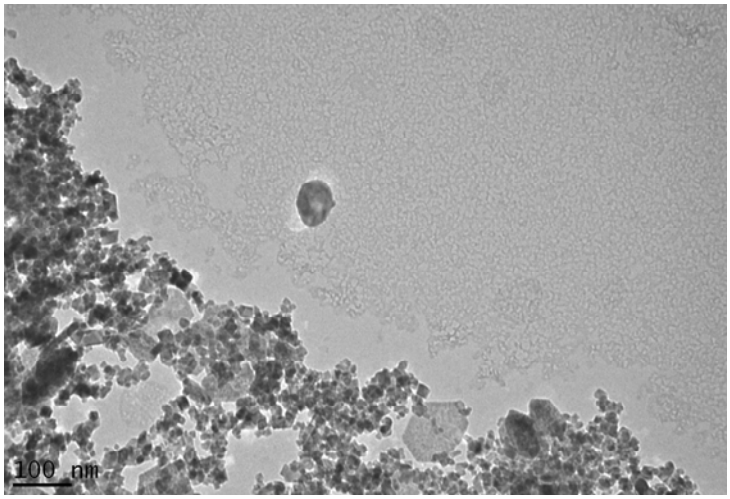

Figure 3.2. Transmission electron micrograph of synthesized magnetite nanoparticles. The nanoparticles are polydisperse in both size and shape.

Transmission electron microscopy reveals that the as synthesized product is polydisperse in size and shape (Figure 3.2).

The synthetic MIO was used as a selection substrate to isolate MIO binders from a commercially sourced New England Biolabs (Ipswich, MA, USA) PhD-12 phage library. Briefly, the phage display library was mixed with the MIO. A permanent magnet was placed on the outside of the reaction vessel and the MIO (and any associated phage) were held in place by the magnetic field while non-binding phage were discarded. Phage bound to the MIO were eluted with 0.2 M glycine (pH 2.2) and used to re-infect *E. coli* K12 ER2738. Phage sequences that were selected were amplified in bacterial culture according to standard protocol and then purified and subject to a subsequent round of magnetic selection. This magnetic selection differs from a typical selection which is usually against a target coated surface. The phage is then allowed to interact with the target coated surface which then allows binding to occur followed by elution of phage. Magnetic selection allows for less sample to be used and as surface coating requires being held on the surface by nonspecific hydrophobic and electrostatic interactions which are more common in biological targets.

After the three selection cycles—which typically results in a sequence convergence for this commercial phage library, 10 phage were taken for commercial sequencing of the library oligonucleotide, using the -96 gIII sequencing primer primer. Each isolate returned a unique

sequence, indicating no consensus on sequences. After an additional MIO selection cycle, ten isolates were sequenced. Of those ten sequences, seven different sequences were represented. One sequence (Table 3.1, Entry 'FeO1') was represented three times, the remaining sequences had unitary representation. After a 5th round of magnetic selection, sequencing of the library oligonucleotide region returned the sequence noted as FeO2 in Table 1. During chemical characterization (see below) of this sequence, we noted that the sequence is not the library oligonucleotide, but rather the 15 amino acids of the pIII (M13 phage protein) following the site to which the library was fused. Because we already observed notable and unique activities for this sequence with $FeCl_2$ (Figure 3.3) we continued with the possibly artifactual FeO2 sequence and continued characterization of the FeO products produced in the presence of the FeO2 peptide.

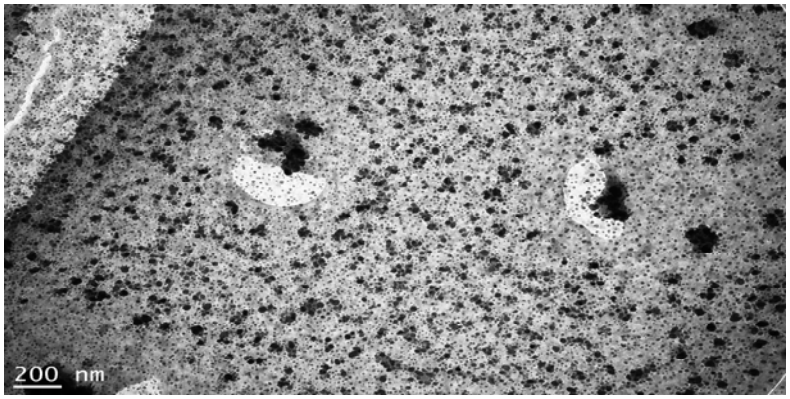

Figure 3.3. Reaction between FeO2, FeCl2 and NaOH.

	Sequence	Length	MW (Da)	pI	Hydrophobicity
FeO1	GTLDPFRTYVPS	12	1352.5	5.84	-0.358
FeO2	AETVESCLAKSHTEN	15	1618.7	4.75	-0.667
C1	HYHYHYHYHYHY	12	1819.9	7.20	-2.250
C2	AYSSG	5	483.4	5.57	-0.300

Table 3.1. Peptide sequence and biochemical properties of control peptides and two peptides isolated out of Ph. D.™-12 kit.

Peptide Sequence Activity. To determine if the peptides isolated from the phage display library can mediate the

synthesis of iron oxide nanoparticles, we tested each of the peptides given in Table 1 in the presence of Fe^{2+}, Fe^{3+} and NaOH.

These sequences are GTLDPFRTYVPS (FeO1) and AETVESCLAKSHTEN (FeO2) (Table 1); these two peptides were compared for their ability to mediate the formation of iron oxide nanoparticles, with the following set of control peptides used for comparison: $(HY)_6$ which was designed to bind and reduce $HAuCl_4$.[152] AYSSG, which was proposed to be the active portion of the A3 peptide,[153] as well as a buffer control (Figure 3.4).

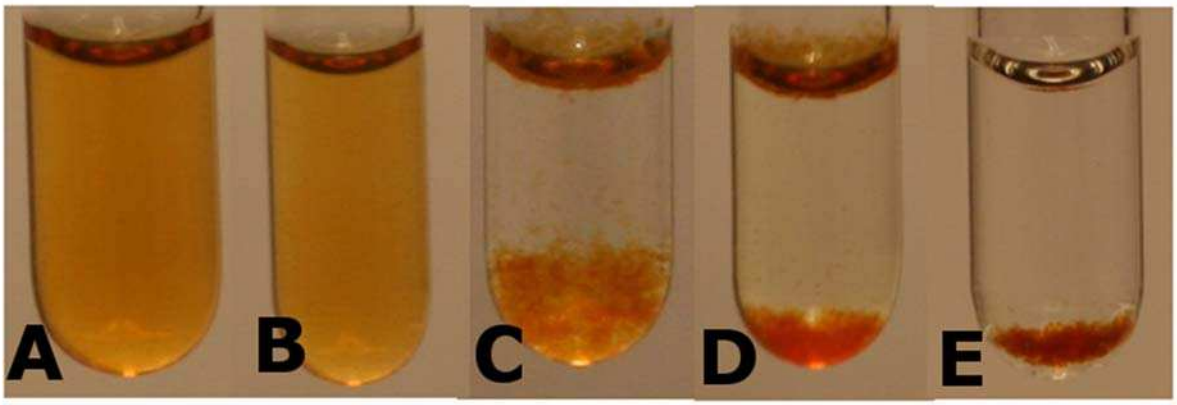

Figure 3.4. Visual representation of (A) FeO1 (B) FeO2 (C) Tris Buffer control (D) $(HY)_6$ (E) AYSSG

FeO1 was found to mediate the formation of micron sized electron dense particles when added to 20 mM Tris (pH 6.8), 30 mM $FeCl_3$, 15 mM $FeCl_2$ and 50 mM NaOH. FeO2 was found to form nanoparticles with a diameter of 4.35 ± 1.27 nm. Compared to the buffer control which formed reddish brown precipitate immediately that were extremely magnetic, but formed large structures that did not seem to be either size or shape controlled, which is in line with current understanding of the role of peptides in nanoparticle formation.[154,155] $(HY)_6$ which seemed to form reddish-brown particles. Which under the TEM seemed to form chains of particles. When held next to a magnet, particles were slow to move towards the magnet. AYSSG formed large non-uniform electron dense particles. We performed electron diffraction on our samples to

better identify the identity of the electron dense particles (Figure 3.5). Electron diffraction revealed that the particles were unlikely to be hematite, goethite, lepidocrocite, or akaganeite, but more likely to be maghemite (γ-Fe_2O_3) or magnetite (Fe_3O_4) (2.82 Å/(220), 2.53 Å/(311), and 2.436 Å/(222)). Electron diffraction of the network of electron dense material made from the buffer control also revealed crystalline material determined to likely be maghemite or magnetite (2.815 Å/(220), 1.95 Å/(400), 1.24 Å (539), 0.99 Å (826)). (Figure 3.6)

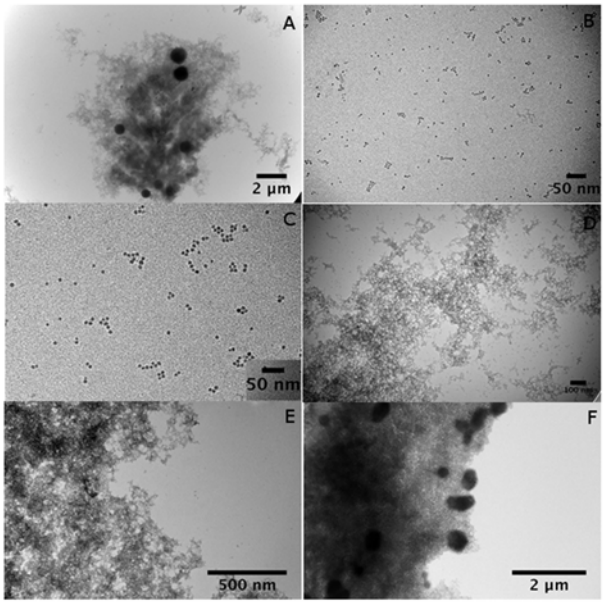

Figure 3.5. Transmission electron micrographs of (A) FeO1 (B) FeO2 (C) magnification of FeO2 (D) Tris buffer control (E) $(HY)_6$ (F) AYSSG

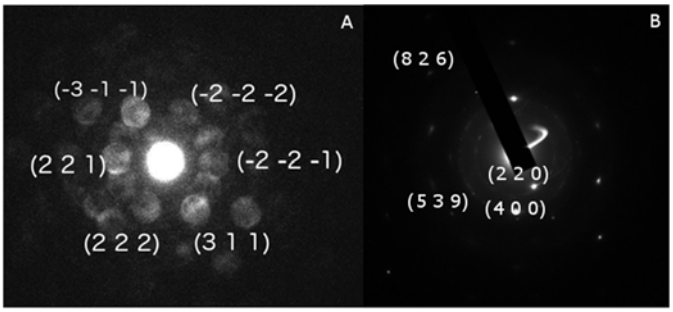

Figure 3.6. Electron diffraction of FeO2 synthesized particles (A), and buffer control particles (B).

In order to make sense of these results it is important to consider the solution phase chemistry. In the formation of any solid metal oxide or hydroxide phase, there first must be a monomeric complexed species.[156]

$$FeCl_3 + 6\,H_2O \rightleftharpoons [Fe(H_2O)_6]^{3+} + 3\,Cl^- \quad (3.1)$$

The hydrolysis of the hexa-aquo complex is often achieved through the addition of base; above pH 7, the hexa-aquo complex undergoes hydrolysis to yield $[Fe(H_2O)_3(OH)_3]^0$, which ultimately

converts to $Fe(OH)_2$ (s). The OH ligand is a nucleophile that can participate in substitution reactions involving any of the remaining hexa-aquo ions. This reaction is referred to as olation:

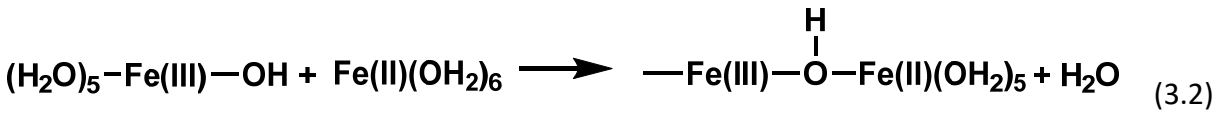

(3.2)

Hydrolysis of these complexes eventually yields iron oxide through the formation of an oxo bridge (oxolation).

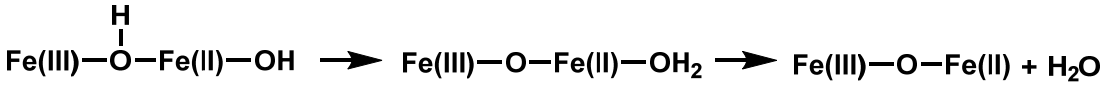

(3.3)

The formation of solid iron oxides requires the hydrolysis of the $[Fe(H_2O)_6]^{3+}$ ion, however, the resultant phase and rate in which these form are highly dependent on rate at which iron can be delivered to the growing iron oxide. Other directing factors are pH, temperature and ionic strength of the solution. At pH > 9, for instance, the coprecipitation of Fe^{3+}/Fe^{2+} favors the formation of magnetite. At room temperature and slightly acidic pH as in this experiment, the conditions of this experiment should favor the formation of ferrihydrite, which can convert to hematite.[157] The electron diffraction does not match with known diffraction patterns of hematite or other common iron oxide nanoparticles.

Based on the color and solubility of the buffer control, it is unlikely that the product formed is a ferrihydrite polymer;[156] however, the fact that much of the product is noncrystalline (Figure 3.7B) suggests that the sequence and length of FeO2 is important in both the shape and formation of nanoparticles.[152,154,155] In the presence of FeO2 peptides, the iron ions input into the incubation solutions appears to be converted to crystalline spherical particles of a consistent

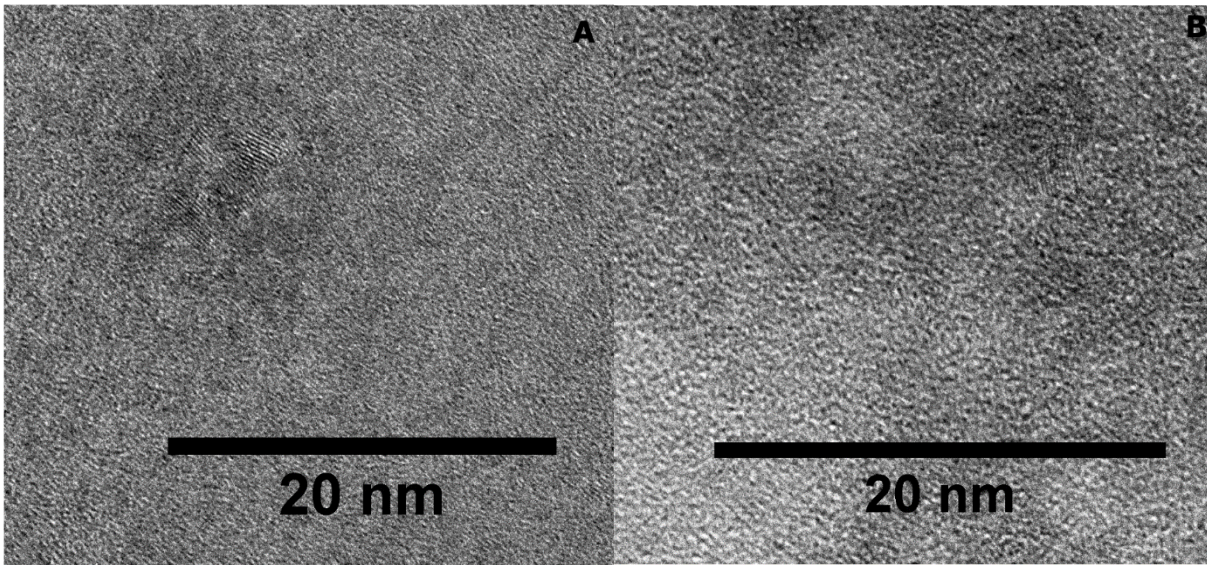

Figure 3.7. High resolution transmission electron micrographs of (A) FeO2 mediated particles (B) Tris mediated particles. There is a much more pronounced electron dense non-crystalline area around particles in B than can be seen in A.

size (4.3±1.4 nm) (Figure 3.7). The actions of FeO2 are reminiscent of previous work by Arakaki *et al.*,[158] where short peptides were synthesized based off of the acidic C-terminus of mms6. Although perhaps most strikingly, peptides derived from mms6 form approximately 20-25 nm particles.[158] The synthesis utilizing mms6 derived peptides also requires two 90 °C heating steps and that the reaction occur under an inert environment; which FeO2 does not. These two 90 °C heating steps would render tagging difficult for biological purposes.

3.3. USAGE OF FTSZ AS A MODEL SYSTEM FOR PEPTIDE FORMATION OF IRON OXIDE NANOPARTICLES

In order to test whether or not this potential tag might be clonable we needed a model system that would react predictably. Our model system to test our peptide clonable nanoparticle system was Filament temperature-sensitive mutant Z (FtsZ). FtsZ is the prokaryotic homologue of tubulin. FtsZ has been heavily studied due to its importance in bacterial cell division. There are several known conformations that FtsZ can take which will help us to further identify our targets.

By utilizing FtsZ as a model system we can attach nanoparticle forming tags to the N-terminus in order to determine directionality and location of the protein. This can then be translated to determining location and directionality of a target protein in a cell.

After isolating which of the peptides would be useful as a potential clonable nanoparticle tag it was cloned onto the N-terminus of the gene of FtsZ. The plasmid containing mms6[159] (a positive control peptide) attached to FtsZ was transformed into C43 *E. Coli* and grown at 30° C. It was found that at 37 ° C, which is E. coli's optimal growth temperature, the gene insert would be excised and only wild type bacteria could be sequenced. The C43 E. Coli is a mutant of the BL21 (DE3) strain of *E. Coli*, which is found to be more tolerant of toxic recombinant proteins as well as offering a higher stability of plasmids.[160] The bacteria was grown to OD_{600} = 0.3 AU and induced with 1 mM IPTG. After induction, bacteria was spun down and collected, then frozen at -20 °C. The pellet was then resuspended in lysis buffer and allowed to thaw. Lysozyme was added to the thawed bacterial pellet followed by sonication. The lysate was run down a nickel column in order to purify recombinant protein, however, we were unable to verify that our protein was being induced. CSU's Protein Expression Facility was however able to express and purify FtsZ (Figure 3.8). While we were unable to achieve very good imaging with the FtsZ, we were able to make out outlines of what may be FtsZ filaments (Figure 3.9). When we attempted to utilize the mms6 peptide to form magnetite, we were unable to utilize mms6 to form magnetite. This is likely due

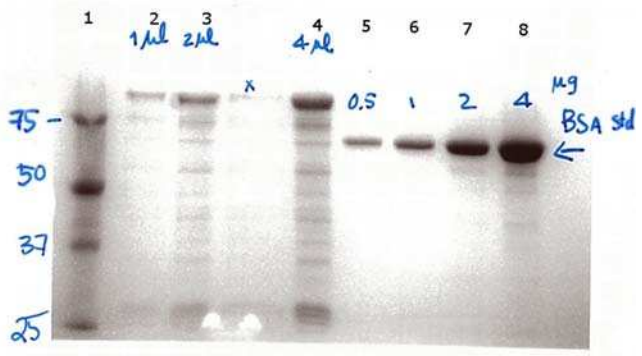

Figure 3.8. Polyacrylamide gel of FtsZ post purification. Lane 1 is a protein standard. Lanes 2 through 4 are the protein purified from expression. Lanes 5-8 are a BSA standard. Protein concentrations were estimated from BSA standards. Photo courtesy of CSU Protein Expression Faciliy.

to two copies of bacteroferritin being attached at the C-terminus of FtsZ. This was discovered after the sequence had been placed into a plasmid and was a carryover from the lab we received the sequence from.

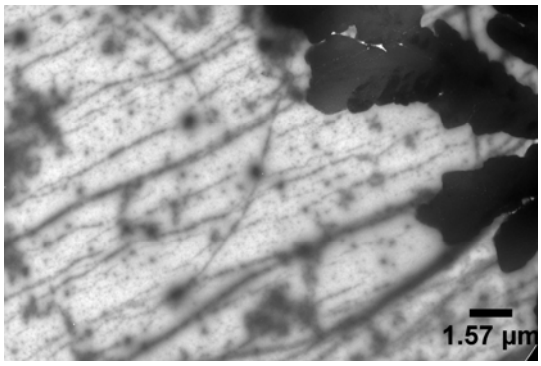

Figure 3.9. Potential FtsZ filaments stained in 1% $U(OAc)_2$.

3.4. PROGRESS TOWARDS CLONABLE INORGANIC NANOPARTICLES

In order to further investigate other clonable biomolecules that may be capable of forming inorganic nanoparticles we turned to an endophyte brought to our attention by a visiting scholar, Lucian Staicu. *Pseudomonas moraviensis* stanleyae was isolated from the roots of *Stanleya pinnata*, a Se hyperaccumulator plant native to western USA,[161] and observed to tolerate unusually high concentrations of SeO_3^{2-}. When grown in Luria Broth supplemented with 10 mM Na_2SeO_3, the cultures become notably pink in color during early log-phase. This color change (Figure 3.10) is associated with the formation of zerovalent (red) Se. The conversion of selenite oxyanions to zerovalent Se is a common detoxification process for bacteria that tolerate high concentrations of Se oxyanions.[162]

Initial characterization of the SeNPs produced by *P. moraviensis* stanleyae was performed by transmission electron microscopy (TEM), scanning electron microscopy (SEM) with energy dispersive X-ray spectroscopy (EDS) elemental mapping, and 3-D cellular electron tomography.

An initial TEM examination of glutaraldehyde-fixed concentrated cell culture of *P. moraviensis* stanleyae, dry mounted on a carbon-coated TEM grid (Figure 3.11, panel A) revealed relatively uniform (107 ± 35 nm) high-contrast circular morphology spots both inside (or superimposed on) and outside of the bacterial cells. Scanning transmission electron microscopy

of the same sampled allowed EDS mapping of elemental composition. The EDS mapping confirms that the high-contrast spots are Se-rich. (Figure 11, panel B) This suggests that the high-contrast spots are Se nanoparticles that account for the red color of the bacterial cultures. Similar spots were not observed in control cultures that were not supplemented with SeO_3^{2-}. At least 50 were examined in the control observation, high density spots were observed only with one cell, and in that instance the morphology was notably irregular compared to the putative SeNPs (Figure 3.12).

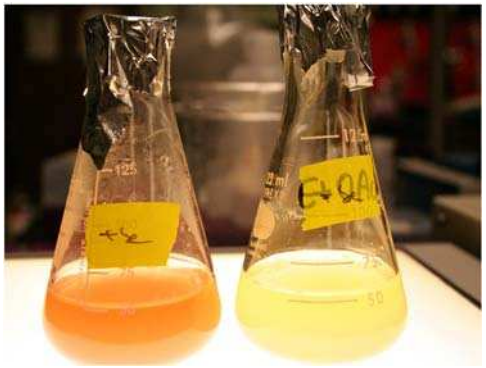

Figure 3.10. Photographs of P. moraviensis stanleyae liquid LB cultures. The culture on the left is supplemented with 10 mM SeO32-. Upon initial growth, both cultures appear as the no-selenite control culture shown at right. We attribute the red color of the culture to which selenite is added to the reduction of selenite to zerovalent red selenium. Photo reproduced with permission from authors and RSC Publishing.[42]

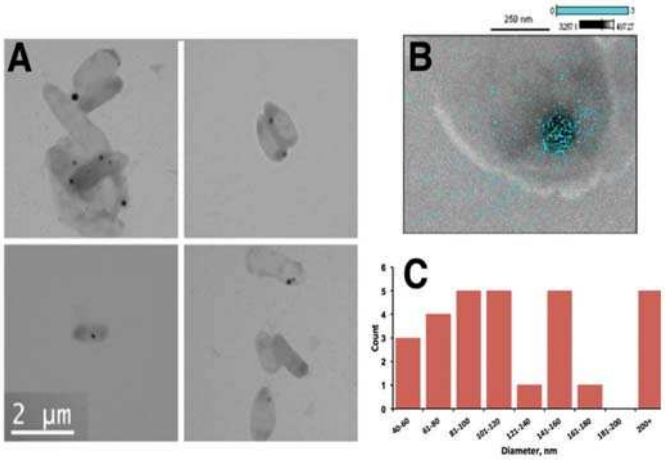

Figure 3.11. Transmission electron micrographs of glutaraldehyde-fixed dry mounted cells are shown in panel A. Electron-dense (dark) inclusions are present in many of the cells in panel A, as well as outside the cells. Panel B shows a scanning transmission micrograph of a selected area of one of the cells that includes a dark inclusion; overlaid on this inclusion is an EDS map of Se in the sample, indicating that the inclusion is Se-rich. Panel C shows a histogram of observed particle sizes. Photo reproduced with permission from authors and RSC Publishing.[42]

Dry mount electron microscopy provides comparatively limited information compared to more sophisticated preservation and imaging methods, such as cellular electron tomogrpahy.[163,164] With appropriate preservation,[165–167] these methods allow high fidelity 3D resolution of cellular ultrastructure such as membranes and major cytoskeletal filaments, organelles and ribosomes.[168]

Herein we used electron tomography to definitively reveal whether the observed nanoparticles are inside the cells (as opposed to superimposed), reveal membranes, and reveal major cellular ultrastructure. *P. moraviensis* Stanleyae cells were grown as described in the methods section, both with and without 10 mM SeO_3^{2-} supplementation into the stationary phase where particles are easily discernable. Concentrated cultures were subjected to freeze substitution,[165] which provides the highest fidelity preservation of cellular ultrastructure aside from vitrification.[169] Vitrification was not used here because the size of the cells would require cryo-sectioning, which is technically difficult and not routinely successful.

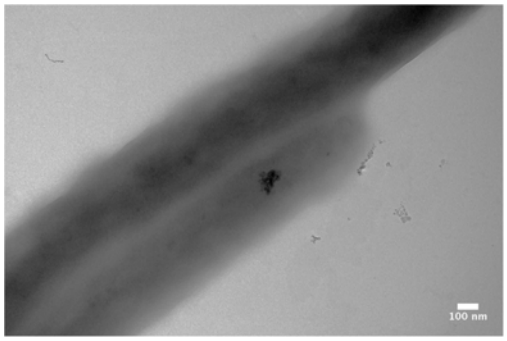

Figure 3.12. Representative micrograph showing irregular electron dense object.

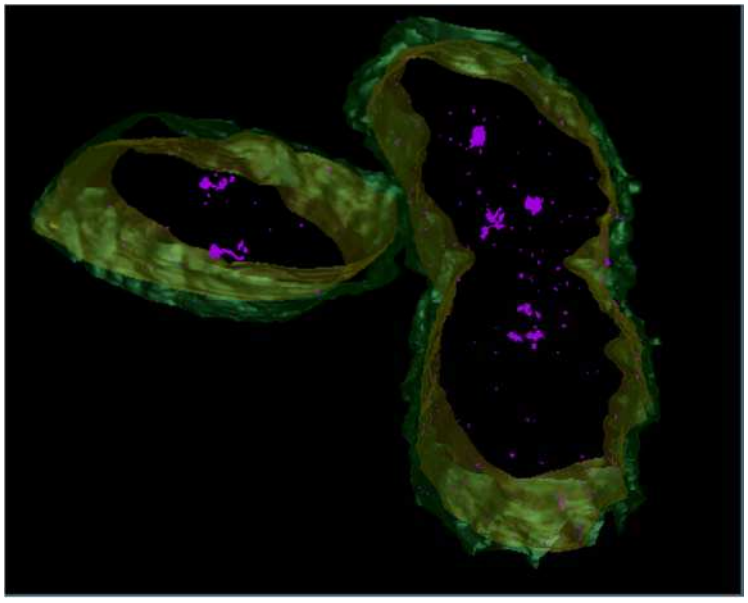

Figure 3.13. Electron tomographic reconstruction of P. moraviensis stanleyae with osmium staining. The outer membrane (green), inner membrane (yellow) and putative SeNP (pink) densities are segmented. Due to the presence of stain, the particle segmentation is ambiguous. Photo reproduced with permission from authors and RSC Publishing.[42]

3D reconstructions of both unstained and osmium stained 200 nm sections revealed large inclusions inside the cells. In the case of metal-stained cells, it was unclear whether the inclusions could be attributed to the staining of biological material or to SeNPs, although other ultrastructures (such as both inner and outer membranes) were clearly revealed (Figure 3.13).

The reconstructions of unstained cells were more informative. Figure 3.14 shows a segmented reconstruction of a single cell; the outer membrane was segmented by hand, as is current standard practice with IMOD, while the SeNPs were sufficiently electron dense that segmentation could be accomplished automatically with a simple thresholding operation. Imodauto was set at a threshold of 1 (out of 255), which generated a model. This clearly auto-segments out high-density inclusions that we attributed to SeNPs. In each of three 3D reconstructions of cells grown with SeO_3^{2-} supplementation we observed high-contrast inclusions of 58.66 ± 2.47 nm diameter (from a total of 3 particles observed).

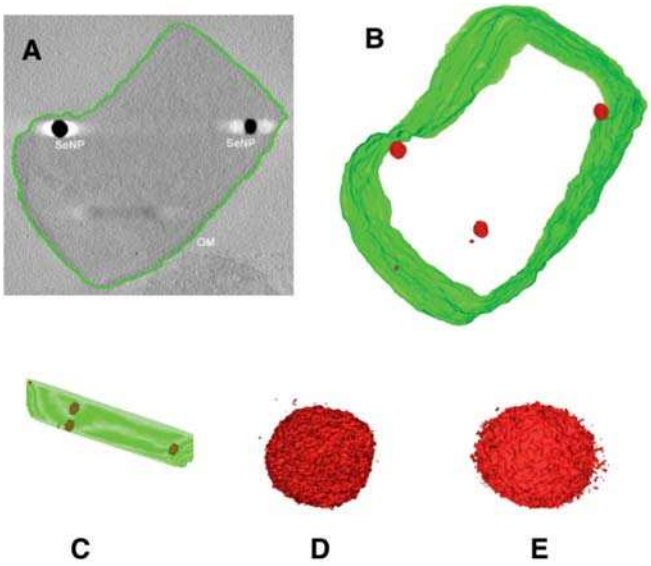

Figure 3.14. Electron tomographic reconstruction of *P. moraviensis* stanleyae. The reconstruction was segmented to reveal the outer membrane and SeNP nanoparticles (panels A-C). Magnified views of two SeNPs are show in panels D and E; panel D shows the large SeNP in the middle of the cell in panel B. Panel E shows the large SeNP in the upper left part of the cell in panel B. Photo reproduced with permission from authors and RSC Publishing.[42]

Figure 3.14 shows a 3D segmentation of one of the cells, with a XY view shown in panel B and an YZ view shown in panel C. These two views reveal unambiguously for the first time that large SeNPs can be intracellularly contained, where previous studies were 2D microscopy and could not rule out that particles and cells are superimposed. Notably, there is no evidence that these particles are membrane-encapsulated, as is observed for other inorganic inclusions such as magnetosomes.[170]

Panels D and E of Figure 3.14 show the three larger intracellular particles at greater magnification. From these images it appears that, while the particles are "approximately

spherical", they are not perfectly spherical and in fact are symmetrically irregular. Some of the irregularity in these images is artifact. The "spikiness / texture" of the surface is also observed for the 10 nm diameter gold nanoparticles used as fiducial markers for alignment.[167] The anisotropic 'speckling' halo that surrounds some of the particles likely arises from the 'missing wedge' artifact in electron tomography.[12] Even accounting for these sources of artifact, however, the nanoparticles appear symmetrically irregular.

To derive greater insight into the mechanism of formation of these SeNPs, we identified proteins implicated in the reduction of SeO_3^{2-} to Se(0) by *P. moraviensis* stanleyae. Briefly we fractionated the soluble proteins from cell lysate on a nondenaturing polyacrylamide gel, and then stained the gel with metalloid oxyanions and electron donating cofactors. Any resulting bands indicating the presence of NADPH-dependent selenite reductase activity were excised and further analyzed by proteomic mass spectrometry.

To obtain better resolution, cell lysate of *P. moraviensis* Stanleyae grown in SeO_3^{2-}-supplemented media was further fractionated on a hydrophobic interaction column (HIC) that was eluted with different concentrations of $(NH_4)_2SO_4$. Proteins in each fraction from the HIC column were separated on a non-denaturing polyacrylamide gel. To develop bands corresponding to selenite reductases, gels were placed into nitrogen-filled zip-lock bags filled with a buffer supplemented with metalloid oxyanions and NADPH or NADH. The entire protocol was adapted from previous work by Hunter.[145]

Figure 15 shows the results of this experiment for the reduction of SeO_3^{2-} in the presence of NADPH. Clearly there are proteins with selenite reductase activity present in some of the HIC fractions. Tellurite (TeO_3^{2-}) reductase activity was observed with similar gel mobility, although

the bands were less intense. No notable reduction of selenate or tellurate (TeO_4^{2-}) to elemental form was noted, and the reduction of SeO_3^{2-} and TeO_3^{2-} was notably weaker when NADH instead of NADPH was used as an electron donor. No bands developed in the absence of NADH or NADPH.

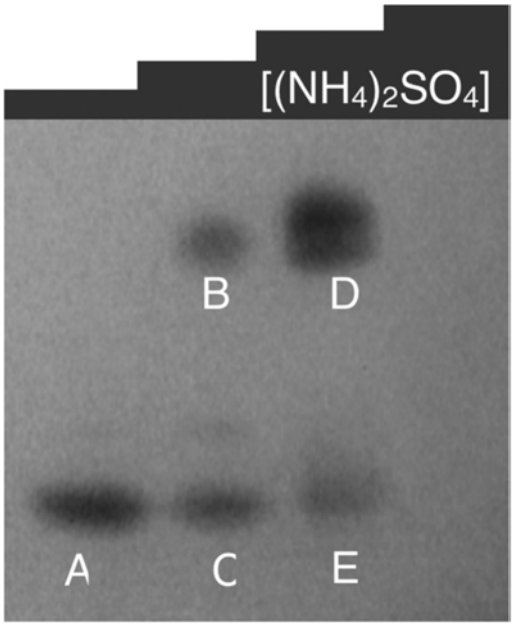

Figure 3.15. Native gel of HIC column fractions, stained with SeO32- and NADPH to reveal bands containing enzymatic SeO32- reductase activity. Lanes in the gel correspond to step fractions taken from a HIC column to process crude cell lysate. Lanes correspond to 0.1 M, 0.5 M, 1.0 M, 1.5 M and 2.0 M elutions of the HIC column with $(NH_4)_2SO_4$. Photo reproduced with permission from authors and RSC Publishing.[42]

Figure 3.15 shows that two bands develop in the anaerobic SeO_3^{2-} + NADPH incubation condition, one that is associated with lower salt elutions from the HIC column and a second associated with higher salt elutions.

To identify the proteins involved in the observed reduction, we excised the bands and identified associated proteins by protein mass spectrometry. From a total of 5 activity bands excised and analyzed for protein content, 122 proteins were identified (Table 4.1). Of these proteins 7 are known to be NADPH or $NADP^+$ dependent. This set of NADPH-dependent proteins (Table 3.1) comprises a set of candidate proteins for specific NADPH-dependent SeO_3^{2-} reduction to Se(0).

Of these proteins, we were especially interested in glutathione reductase (GSHR) and nitrite reductase, as each was previously implicated in selenite reduction.[145,171–173] To validate the specificity and investigate the enzymatic mechanism, we obtained baker's yeast (*Saccharomyces cerevisiae*) GSHR from Sigma-Aldrich (G3664) and the NADPH-dependent

cytochrome C reductase (C3381) and *Aspergillus niger* nitrate reductase (N7265) as comparison control enzymes. Each enzyme was tested for competence to reduce SeO_4^{2-}, SeO_3^{2-}, TeO_4^{2-}, and TeO_3^{2-} to zerovalent forms of Se and Te, respectively, as judged by a color change of the solution from clear to turbid red (Se) or gray (Te) upon inclusion of either NADH or NADPH as electron donors. In this initial screening of enzymes and substrate specificity, we found that GSHR with NADPH as an electron donor could reduce SeO_3^{2-} and TeO_3^{2-}, while no other combination resulted in notable metalloid oxyanion reduction.

Table 3.1. NADPH-dependent enzymes identified in mass spectrometry. Table reproduced with permission from authors and RSC Publishing.[42]

Oxyreductase	Accension number	MW (Da)	Cofactor/Rxn	Band association
Nitrite and sulfite reductase	gi|77459334	62 262	NADPH	B
Isocitrate dehydrogenase [*Pseudomonas fluorescens* SBW25]	gi|229591243	66 003	$NADP^+$/ATP	B, C, D
Glutathione reductase [*Pseudomonas fluorescens* Pf0-1]	gi|77459153	49 244	$NADP^+$/FAD	B, D
5,10-Methylenetetrahydrofolate reductase [*Pseudomonas fluorescens* Pf0-1]	gi|77461502	31 515	$NADP^+$/FAD	B, D
3-Ketoacyl-ACP reductase [*Pseudomonas fluorescens* Pf0-1]	gi|77460378	25 500	NADPH	A
Thiol peroxidase [*Pseudomonas fluorescens* Pf0-1]	gi|77458745	17 586	NADPH/H_2O_2	B, D
4-Aminobutyrate aminotransferase [*Pseudomonas fluorescens* Pf0-1]	gi|77456416	44 837	NADPH	A, B, C, D, E

In order to understand the mechanism by which GSHR converts these metalloid oxyanions, we first characterized basic enzymatic properties for both SeO_3^{2-} and TeO_3^{2-} substrates. K_m and V_{max} were determined by observing the rate of consumption of NADPH, which has an easily observable spectroscopic signature (Figure 3.16). We found a K_M of 31 mM for SeO_3^{2-} and a K_M of 0.54 mM for TeO_3^{2-} (Figure 3.17). The reported K_m value of GSHR for GS-SG is ~50μM[174] suggesting that the GSHR-like enzyme has a substantially higher substrate affinity for GS-SG than for SeO_3^2.

After dialysis to remove small molecules, the products of GSHR reduction of TeO_3^{2-} and SeO_3^{2-} were examined by TEM. Reduction of TeO_3^{2-} to Te(0) by GSHR produced networks of sub 5 nm particles, where the diameters are difficult to discern, similar to the previously reported

enzymatic reduction of Ti^{3+} (as TiBALD) by cysteine and serine proteases.[141] Reduction of SeO_3^{2-} to Se(0) in otherwise identical conditions resulted in larger, discrete 61 ± 37 nm diameter SeNPs. Figure 3.18 shows electron micrographs of each product and a histogram of size distribution for the SeNP.

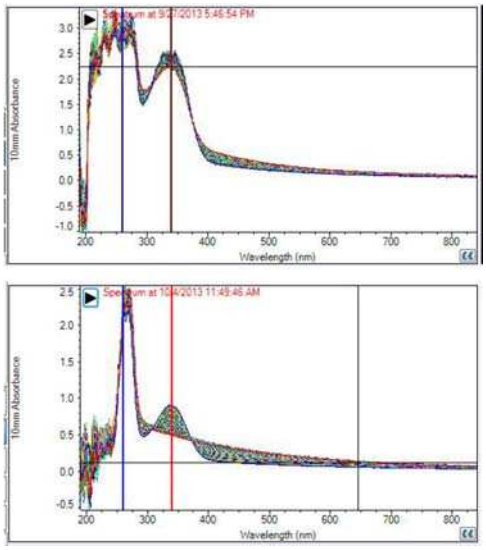

Figure 3.16. Example spectroscopic data showing enzymatic consumption of NADPH as judged by diminishment over time of the peak at 340 nm that arises from NADPH. Monitoring of this consumption (or lack thereof) allowed claims of substrate specificity and the Lineweaver-Burk plots show in Figure 16. Photo reproduced with permission from authors and RSC Publishing.[42]

In the enzymatic assays, we observed that the steady-state phase of product production was remarkably short-lived (Figure 3.17). We subsequently observed that the enzyme itself was consumed in the *in vitro* reaction, as determined by a Bradford assay for total protein (Figure 3.19, circles). This suggested that the enzyme is associated with the particles it synthesizes, perhaps even entombed in the particle.

To test this hypothesis of association or entombment, we separated by centrifugation the enzymatically formed SeNPs from soluble enzyme. The insoluble protein fraction corresponded to 18% of the total enzyme in the assay. SeNPs are known to be dissolvable in solvents such as ethylenediamine and benzene.[175] We found that enzymatically produced SeNPs are also soluble in Bradford protein assay. In fact, we could recover nearly quantitatively the protein that disappears from the enzymatic assay in a Bradford assay of the enzymatically produced SeNPs. This data is shown in Figure 19, left panel. There is evidence that the soluble fraction of GSHR is also associated with smaller SeNPs. In an SDS-PAGE of the soluble fraction of GSHR, a difference

in electrophoretic mobility coupled to a 'smearing of the band', consistent with the enzyme being bound to polydisperse particles, is observed in comparison to a control reaction. Overall, we suggest that some fraction of the enzyme is associated with or entombed in the nanoparticles that the enzyme creates. When NADPH cofactor is omitted from the reaction, the enzymatic process does not proceed, and the observed enzyme concentration remains constant (Figure 3.20, diamonds).

The size of the enzymatically synthesized SeNPs is controllable through modulation of enzyme substrate concentrations. By varying the [NADPH] in an *in vivo* reaction, we observed that we could vary the size of the resulting particles from 2.5nm to more than 50nm diameter. The effect of [NADPH] on particle size is shown in Figure 3.21.

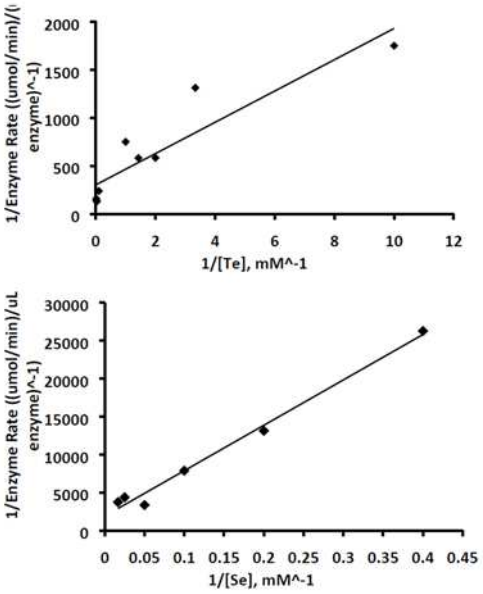

Figure 3.17. Lineweaver-Burk plots for TeO_3^{2-} and SeO_3^{2-} reduction by GSHR. Photo reproduced with permission from authors and RSC Publishing.[42]

We identify the first polypeptide capable of soluble precursor reduction, retention of reduced product at the site of reduction, and size control of the reduced product. This represents a

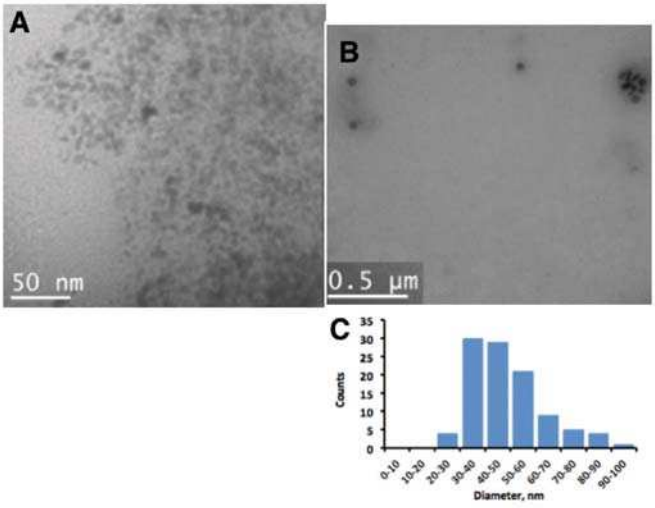

Figure 3.18. Transmission electron micrographs of the characterization of *in vitro* products of GSHR reduction of TeO_3^{2-} (panel A) and SeO_3^{2-} (panel B). Panel C shows the size distribution histogram observed for GSHR produced SeNPs. Photo reproduced with permission from authors and RSC Publishing.[42]

notable step in progress toward a clonable nanoparticle, which is fundamentally different from other proposed strategies for clonable nanoparticles. First, other strategies rely on stoichiometric binding of metal ions,[38,115] or on oxidation events,[35] while this approach uses enzymes and NADPH as an electron donor to reduce inorganic precursors. We infer that the products of reduction are often retained by the enzyme that creates them, possibly by an entombing mechanism. This rare combination of three activities in biogenic nanoparticle production was previously suggested for reduction of Au(III) precursors by the same enzyme.[142] In that work, however, the resulting particles are quite small and, as noted above, Au reduction is quite promiscuous by biomolecules[118] while the selenite and tellurite reductions reported here appear specific to just a handful of enzymes, as evidenced by Figure 3.15. We observe notable differences in the resulting size of particles, depending on the growth condition. We cultured *P. moraviensis* Stanleyae cells for up to 36 hours

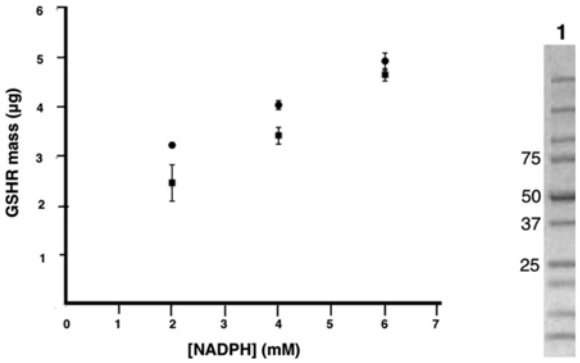

Figure 3.19. Left panel shows the amount of GSHR lost from the assay at different NADPH cofactor concentrations in circles. In squares is depicted the amount of protein measured from the insoluble selenium particles created during the assay. The agreement between protein lost from the assay and protein recovered from the particles suggests that the enzyme is associated or entombed in the particles it creates. The right pane shows an SDS-PAGE of the soluble fraction of GSHR after an assay. The small shift in electrophoretic mobility and large smear about the band can be attributed to association between the enzyme and smaller SeNPs. Photo reproduced with permission from authors and RSC Publishing.[42]

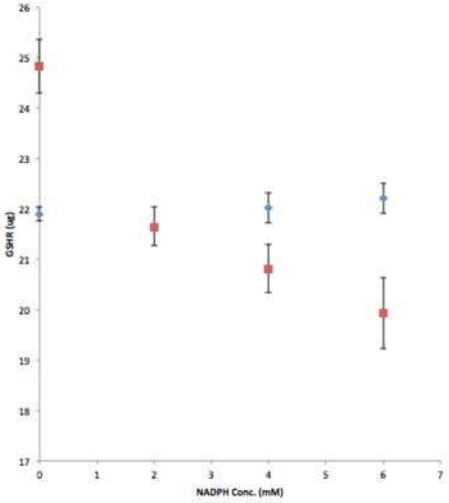

Figure 3.20. The results of a Bradford assay of a fixed amount of GSHR exposed to varying amounts of NADPH, with SeO3-2 either present at 10 mM concentration (red squares) or absent (blue diamonds). When SeO32- is present (red squares) the enzyme vanishes from the assay in an NADPH dependent manner. Photo reproduced with permission from authors and RSC Publishing.[42]

in the presence of SeO_3^{2-} supplementation, to ensure an abundance of SeNPs in subsequent microscopic examination. We grew cells for this extended time both with and without replacement of media. When the media was not replaced, it is likely that it is depleted of necessary nutrients at the 36 hour time point, and the cells are starving. The starvation condition of cells in Figures 3.11 and 3.12 may partially explain the difference in average particle size observed between the intracellular particles in Figure 3.11 (107 nm diameter) and Figure 3.14 (58 nm diameter). Notably, in Figure 3.13 the membranes are quite distorted, consistent with starving cells that are having difficulty maintaining homeostasis. The starvation condition was avoided for cells reconstructed for Figure 3.14 by replacing the growth media every 12 hours. Note that particle diameters measured for SeNPs in 'healthy' cells (58 nm diameter average diameter) and SeNPs produced *in vitro* by GSHR (61 nm average diameter) are within measurement error. This concurrence in particle size suggests that the *in vitro* and *in vivo* mechanisms that underlie the formation of these SeNPs are similar.

Key for future application is minimizing the mass of the biological components of clonable nanoparticles. For instance, the mass of GFP is 27 kDa, yet some studies have demonstrated that GFP concatemers can interrupt the native function of the protein fused to GFP.[175,176] This stands in contrast to the well-established intracellular inorganic nanoparticles, which are coated either by a membrane or by a structured protein capsule.

We hypothesize that the particles are naked, with the Se(0) exposed to the cytosol, from a combination of structural and chemical evidence. From the tomographic reconstructions, we observe no evidence for a membrane around the SeNPs, while membranes are easily observed for naturally occurring magnetite nanoparticles.[170] The low symmetry of the particles, dispersity,

and differences in average size that depend on growth conditions suggest that there is no structured protein coat, such as that found with ferritin and DPS-coated nanoparticles.

Chemically, we note that nearly all clusters and nanoparticles require a ligand shell to quench the chemical reactivity associated with the open valence electron shells of most pure elements. A handful of elements, however, including Se and Te as well as As, Bi, and Sb are known to form stable naked cluster compounds.[177]

This is in many cases because the element can achieve noble gas-like electron counts by catenation, often resulting in ring structures in the solid state, such as the well-known S_n, Se_n, and Te_n ring compounds where $6 \leq n \leq 8$. Indeed, a recent report suggests that while the surface of SeNPs is more complex than an approximately scaled giant naked Se cluster, the surfaces are stable without formal ligation.[178] Furthermore, protein mass spectrometry on purified SeNPs fails to identify candidate proteins that are known to interact with inorganic ions or surfaces.[144] Thus, the combination of irregular symmetry, absence of a membrane, and plausibility of a ligand-free surface suggests that SeNPs may represent the first described class of cytosol exposed inorganic nanoparticle surfaces.

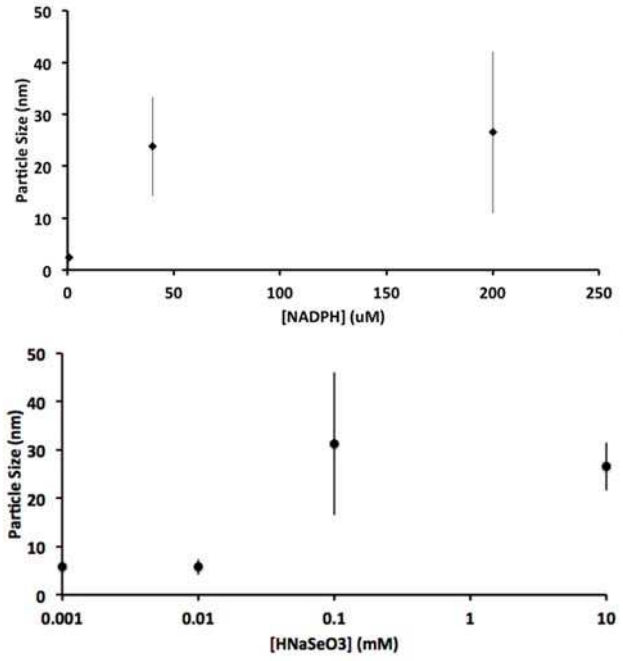

Figure 3.21. Top panel shows how particle size changes as [NADPH] cofactor is varied. Bottom panel shows distribution of particle sizes (y-axis) as a function of [SeO_3^{2-}] concentration in the assay (x-axis).

The commercially sourced GSHR and GSHR or GSHR-like enzymes identified in *P. moraviensis* Stanleyae are not immediately useful as a clonable label in cellular EM. First, the resulting SeNPs are substantially larger than practical; second, other GSHRs, nitrite reductases, and thioredoxin[179] may also produce background particles. While these enzymes are not characterized *in vitro* as producing SeNPs, they are characterized as using SeO_3^{2-} as a substrate. We have not yet evaluated the portability of this clonable nanoparticle for use in other cell lines. The concentrations of SeO_3^{2-} we used in both the *in vitro* and *in vivo* work herein are in the range where toxicity is expected for most cells and organisms. The K_M of the baker's yeast enzyme is low, especially compared to oxidized GS-SG and GS-Se-SG substrates investigated historically for this enzyme.[174,180] Due to the measured K_M, the baker's yeast GSHR will always require typically toxic concentrations of SeO_3^{2-} for nanoparticle formation. Furthermore, specialized selenium transporters that may be present in the selenium hyperaccumulator studied here may also enable the large intracellular particles observed in Figures 3.11 and 3.14. Thus, we anticipate cloning the GSHR-like enzyme from *P. moraviensis* Stanleyae, under the hypothesis that this selenium-specialized enzyme will have a much more favorable K_M, and that the enzyme may function well with physiologically normal concentrations of SeO_3^{2-} while simulatenously conferring resistance to Se toxicity to cells in which it is expressed. An enzyme optimized for selenite or tellurite reduction may allow superior labeling specificity by kinetically outrunning any competing reactions.

While additional work is required to complete the adaptation of this clonable nanoparticle approach for general cellular use, this approach may find more immediate use in labeling purified macromolecular complexes. Presently labeling with *ex situ* synthesized gold

nanoparticles is state-of-the-art for this purpose, with applications in molecular EM, X-ray free-electron laser, and SAXS studies of macromolecular complexes.[27] A clonable approach to this contrast problem may make this sort of tagging much more facile.

For instance, Se (and Te) oxyanions have notable advantages as precursors over previously investigated Au and Fe-based systems. The Au(I) and Au(III) coordination compounds are broadly cross-reactive (i.e., easily reduced into background particulate material) by a wide swath of biomolecules and buffers.[118,120,121] This broad cross-reactivity may explain the dearth of followup to reports of metallothionein / Au combinations as molecular and cellular EM labels. In contrast, the present work and some preceding work suggest that the palette of proteins that possess notable reactivity against the metalloid oxyanions TeO_3^{2-} and SeO_3^{2-} is comparatively limited in number.

Improved size control may be imposed by concatenated or co-expressed peptides. Several dodecapeptides are now known to impose size control[136] on a number of *in vitro* synthesized metal nanoparticles.[181] Similar peptides may be isolated to impose size control on SeNPs or TeNPs.

3.5. CONCLUSION

In conclusion, we identify the first polypeptide that appears capable of synthesizing, retaining and size-controlling an inorganic nanoparticle. By virtue of their metalloid composition, the particles may be naked and exposed to free cytosol. We also find that metalloid oxyanions are comparatively selective in their cross-reactivity against biological molecules. Overall, we suggest that metalloid reductases, including the GSHR-like reductase characterized here,

comprise a class of enzymes that may find use in imaging applications needing a clonable nanoparticle.

Further we also present a small 15 amino acid peptide that may also potentially be useful as a tag. While the size of the nanoparticle formed is in the ideal range of 3-5 nm, it may be difficult to utilize iron inside of a cell as iron ions are carefully corralled inside of a cell[182] due to concerns of forming free radicals.[183,184] While this peptide may be ineffective as a potential tag due to difficulties in controlling both iron concentration and iron species formation inside of a cell, it does still however display interesting properties towards controlling shape and size of an iron oxide nanoparticle.

3.6. METHODS

3.6.1. NOVEL PEPTIDE CAPABLE OF FORMATION OF IRON OXIDE NANOPARTICLES

Fe_3O_4 synthesis. $FeCl_3$ (0.073 g, 0.00045 mol) was dissolved in 15 mL of nanopure H_2O. In a separate 15 mL centrifuge tube, $FeCl_2$ (0.028 g, 0.00022 mol) was dissolved in 15 mL of nanopure H_2O. Both solutions were sonicated to fully dissolve. Once dissolved the two solutions were combined in a 100 mL round-bottomed flask with stir bar. The solution was then stirred and 10 mL 3 M NaOH was added to the round-bottomed flask. The solution and precipitate were placed into a 50 mL centrifuge tube and centrifuged at 4000 rpm for 10 minutes. The precipitate was collected and the supernatant discarded. The precipitate was then washed by resuspending the precipitate in 30 mL nanopure H_2O and centrifuged again at 4000 rpm for 10 minutes. This washing procedure was used three times in order to remove the excess iron (III) chloride, iron (II) chloride and salt from the synthesis. The precipitate was then dried using a lyophilizer set to -49 °C and 0.070 mbar.

Powder X-Ray Diffraction. Dried precipitate was placed on a glass slide and data was recorded on a Scintag X-2 Powder X-Ray Diffractometer. Data was collected from 2θ = 20° to 70° at steps of 0.2°.

Phage Display. 50 uL of magnetic iron-oxide nanoparticles were placed in a 1.7 mL Eppendorf tube; to this 1 mL Tris-buffered saline (TBS) (50 mM Tris-HCl (pH 7.5), 150 mM NaCl) was added. This solution was mixed by gentle inversion of the capped Eppendorf tube. The MIOs were then separated magnetically and the TBS was removed via pipette. In a separate 1.7 mL Eppendorf tube, the phage library was diluted 20x (10 μL phage library into 190 μL TBS). This phage solution was added to the MIO pellet and incubated at room temperature for 15 minutes. The MIOs were pelleted with a 30 s spin at 800 rpm. The supernatant was removed and washed with 1 mL TBS; this was vortexed gently and then pelleted at 800 rpm for 30 s. This washing procedure was performed 10 times. The phage and MIO were incubated in 0.2 M glycine-HCl (pH 2.2) for 10 minutes at room temperature. The mixture was centrifuged for 1 min at 800 rpm. The Eppendorf tube was placed in a magnetic rack for 1 min and the supernatant was transferred to a new Eppendorf tube. Then, 150 µL of 1 M Tris-HCl (pH 9.1) was added immediately to the supernatant to neutralize the glycine solution. This was important to do as the acidic pH could denature the peptides and phage proteins.

Next, 10 µL of the unamplified phage was saved for titering. The remaining volume was added to a previously inoculated 20 mL culture of ER2738 (OD_{600} = 0. 1-0.5). The 20 mL culture was shaken at 37 °C, 200 rpm for 4-4.5 hours in a Fisher Scientific MaxQ 4000 incubating shaker. The culture was transferred to a 50 mL centrifuge tube and centrifuged at 4,000 rpm for 10 min. The top 80% of the supernatant was transferred to a new 50 mL conical and PEG-NaCl (20% (w/v)

PEG-8000, 2.5 M NaCl) was added to equal 1/6 of the supernatant's volume. This solution was cooled at 4 °C overnight.

Next, the solution was spun for 15 min at 4 °C for 10 min. The supernatant was removed and then centrifuged again briefly to remove excess supernatant. The pellet was then resuspended in 1 mL TBS by vortexing for 1 min. The suspension was transferred to a 1.7 mL Eppendorf tube and spun at 14,000 rpm for 5 min at 4 °C. The supernatant was transferred to a new 1.7 mL Eppendorf tube and PEG-NaCl was added to equal 1/6 of the total supernatant volume. This solution was placed on ice for 45 minutes, then centrifuged at 14,000 rpm for 10 min at 4 °C. The supernatant was removed and the pellet was resuspended in 200 µL of TBS. This suspension was centrifuged for 1 min at 14,000 rpm. The supernatant was transferred to a new 1.7 mL Eppendorf tube. Another 10 µL was saved as the amplified titering in order to count colonies at a later date (titering).

Phage Titering. To start 5-10 mL of Lysogeny broth (LB) was inoculated with ER2738 from a plate. The LB was shaken 4-8 hours until mid-log phase (OD_{600} ≈ 0.5). Top Agar (10 g Bacto-Tryptone, 5 g yeast extract, 5 g NaCl, 7 g Bacto-Agar) was melted in a microwave. Next, 3 mL of Top Agar was dispensed per titer experiment, into a sterile culture tube. The culture tubes were maintained at 45 °C until needed. LB/isopropyl-β-D-thiogalactosidase (IPTG)/5-bromo-4-chloro-3-indolyl-β-D-galactosidase (Xgal) (1 L LB, 15 g/L agar, 1 ml IPTG/Xgal stock (1.25 g IPTG, 1 g Xgal in 25 mL DMF)) plates were warmed to 37 °C.

Dilutions of phage were prepared ranging from 10 to 10^3-fold dilutions in LB. Amplified phage culture supernatants were diluted 10^8-10^{11} fold while unamplified phage were diluted from 10-10^4-fold. When LB inoculated with ER2738 reached mid-log phase, 200 μL of the LB was

dispensed into each of 1.7 mL Eppendorf tubes (one tube for each dilution) followed by 10 μL of the phage dilution. The Eppendorf tube was vortexed quickly then incubated at room temperature for 5 min. The infected cells were pipetted into the culture tubes containing Top Agar and immediately poured onto the prewarmed LB/IPTG/Xgal plates. The plates were allowed to cool for 5 min then incubated overnight at 37 °C. The next day plaques were counted to determine plaque forming units (pfu).

Plaques were amplified for sequencing by diluting an overnight culture of ER2738 1:100 in LB. 1 mL of diluted culture was dispensed into culture tubes (one for each clone). Using a pipet tip passed through a Bunsen burner, a blue plaque was taken up from the titering plate and transferred into a culture tube. The tubes were incubated at 37 °C with shaking for 4.5-5 hr. The cultures were transferred to 1.7 mL Eppendorf tubes and centrifuged at 14,000 rpm for 30 seconds. The supernatant was transferred to a new 1.7 mL Eppendorf tube and was again centrifuged at 14,000 rpm. The top 80% of the supernatant was again transferred and sent for sequencing.

Sequencing. Sequencing was performed by Retrogen, Inc (San Diego, CA USA) using the -96 gIII sequencing primer. Returned sequences were then analyzed using 4peaks (Amsterdam, Netherlands) and those deemed to be complete were saved. Sequences were then synthesized by GenScript (Piscataway, NJ USA) to yield 30-38 mg of peptide (> 95%). Other control peptides were synthesized by GenScript as well.

Peptide MIO Formation. These peptides were tested for MIO activity by taking 10 μL of the peptide and incubating in 30 μL 0.05 M Tris (pH 6.8). To this solution, 30 μL 30 mM $FeCl_3$ was added to the 1.7 mL Eppendorf tube as was 30 μL 15 mM $FeCl_2$ and 10 μL 30 mM Tris (6.8). The

reaction was continued with the addition of50 μL of 50 mM NaOH. This solution was drop casted onto pre-glow discharged 200 mesh carbon-coated Cu grids. Transmission electron micrographs were taken on a JEOL JEM-1400 at 100 kV.

3.6.2. USAGE OF FTSZ AS A MODEL SYSTEM FOR CLONABLE TAGS

FtsZ expression and purification. Sequences were added to the N-terminus of FtsZ. The sequence of FtsZ was taken from information provided to us by the Feldheim group at the University of Colorado at Boulder. Codon optimization and vector insertion into pJExpress414-T7-amp-high was done by DNA 2.0. Vectors were transformed into C41(DE3) Chemically Competent *E. Coli* (Lucigen, Middleton WI USA) by adding 10 µL of plasmid to 30 μL of C41(DE3) *E. coli*, this was gently mixed by flicking the bottom of the culture tube. The competent cell/plasmid mixture was cooled on ice for 30 min. Cells were heat shocked by placing culture tube in a 42 °C water bath for 45 s. The tubes were cooled on ice for 2 min followed by addition of 300 μL of LB and incubated with shaking for 45 min. at 37 °C. The solution was plated onto standard LB agar/Ampicillin (amp, 100 μg/mL) plates.

Next, 3 mL LB was pipeted into a culture tube. Single colonies were picked from LB/amp plates using a sterile pipet tip, then added to the culture tube. The culture tube was incubated with shaking at 37 °C until OD_{600} = 0.3. 50 μL of the inoculated LB was added to 50 mL fresh LB in a 125 mL Erlenmeyer flask. The flask was incubated with shaking at 37 °C until OD_{600} = 0.4, at which point 1 mL 1 mM IPTG was added to induce protein expression. After a 4 hr induction, solution was centrifuged at 4,000 rpm at 4 °C for 10 min. The supernatant was discarded and the pellet was resuspended in 20 mM Tris (pH 6.8) and placed in a -20 °C for at least two hours. The frozen cell pellet was thawed, 0.1 g lysozyme was added to the cell pellet and sonicated in a

FisherScientific Sonic Dismembrator at 30% amplitude, 30 s on, 1 min. off, for a total of 10 minutes of sonication time. The lysed cells were centrifuged at 4,000 rpm at 4 °C for 10 min. Supernatant was collected and purified using a HisTrap HP 5 mL column on an ÄKTApurifier; the detector was set at 254 nm. Fractions were collected and protein was concentrated by trichloroacetic acid (TCA) precipitation. Fractions were run on a 12% polyacrylamide gel. Further protein expression and purification was performed by Colorado State University's Protein Expression Facility.

FtsZ was polymerized by incubating FtsZ at 30 °C in the polymerization buffer. The polymerization buffer consistes of 50 mM MOPS (pH 6.0), 10 mM MgCl2 and 200 mM KCl. GTP was added last to a final GTP concentration of 1 mM. 4 µL of this solution was pipeted onto a 200 mesh C coated Cu grid that was previously glow discharged. The solution was wicked away and then 4 µL of 1% (w/v) $U(OAc)_2$ was pipeted onto the grid and wicked off.

3.6.3. PROGRESS TOWARDS CLONABLE INORGANIC NANOPARTICLES

Cell lysate preparation. *P. moraviensis* Stanleyae cells were grown for 24 h at 30 °C in 2,800-mL Fernbach flasks containing 1 L of LB-Miller medium supplemented with 10 mM Na_2SeO_3. Cells were harvested via centrifugation at 10,000 x g for 20 minutes and the pellet resuspended in 15 ml of ice-cold 25 mM Tris and 192 mM glycine buffer (pH 8.3) supplemented with 1 mM 4-(2-aminoethyl) benzenesulfonyl fluoride hydrochloride (AEBSF) and 0.02% 3-[(3-cholamidopropyl) dimethylammonio]-1-propanesulfonate hydrate (CHAPS). Then, cells were treated with 0.2 mg mL-1 lysozyme (Sigma-Aldrich, St. Louis) for 20 min in a 100 rpm shaking incubator at 30°C. Following lysozyme treatment, the cells were homogenized via a French pressure cell operated at 120 MPa. The procedure was repeated twice and this final homogenate

was spun at 22,500 x g for 60 min at 4°C to remove unbroken cells and cell debris. These procedures were modified from Hunter.[185]

Scanning Electron Microscopy *P. moraviensis* Stanleyae cells were grown for 24 h at 30 °C in a 125 mL Erlenmeyer flask containing 50 mL LB medium (Teknova) supplemented with 10 mM $HNaSeO_3$ (Alfa Aesar, 98+%). Cells were harvested via centrifugation at 4,000 rpm (3,220 rcf) for 20 minutes at 4 °C. Cells were then washed in 20 mM Tris (pH 7.4) (Fisher) three times followed by resuspension in 1 mL of fixing fixative solution (2% glutaraldehyde (25%, Sigma-Aldrich) and 2.5% formaldehyde); the fixing solution was allowed to react for 6 h at 4 °C. Post-fixation, the fixing solution was removed by centrifugation and the pellet was washed five times in 20 mM Tris (pH 7.4). The cells were then resuspended in 1 mL 20 mM Tris (pH 7.4). Aliquots (2 µL) were mounted on 400 mesh Cu grids with a 50 nm C coating. Dry-mounted cells on TEM grids were loaded onto a STEM holder. STEM images were taken on a JEOL JSM-6500-F Scanning Electron Microscope at an accelerating voltage of 30 kV.

Energy Dispersive X-Ray Spectroscopy. EDS was performed on *P. moreviensis* Stanleyae cells in the SEM as described above. EDS was collected on a Noran System 7 X-ray Microanalysis detector with a time interval of 1 s.

Dry-mount cellular TEM. *P. moraviensis* Stanleyae cells were grown for 24 h at 30 °C in a 125 mL Erlenmeyer flask containing 50 mL LB medium (Teknova) supplemented with 10 mM $HNaSeO_3$ (Alfa Aesar, 98+%). Cells were harvested via centrifugation at 4,000 rpm (3,220 rcf) for 20 minutes at 4 °C. Cells were then washed in 20 mM Tris (pH 7.4) (Fisher) three times followed by resuspension in 1 mL of fixing fixative solution (2% glutaraldehyde (25%, Sigma-Aldrich) and 2.5% formaldehyde); the fixing solution was allowed to react for 6 h at 4 °C. Post-fixation, the

fixing solution was removed by centrifugation and the pellet was washed five times in 20 mM Tris (pH 7.4). The cells were then resuspended in 1 mL 20 mM Tris (pH 7.4). Aliquots (2 µL) were mounted on 400 mesh Cu grids with a 50 nm C coating. TEM images were taken on a JEOL JEM-1400 Transmission Electron Microscope at an accelerating voltage of 100 kV.

3D Electron Microscopy.

For cells harvested at 6, 9, and 12 hours post selenium inoculation: a single colony was picked from an LB agar plate of *P. moraviensis* Stanleyae and placed into 3 ml of LB culture media and incubated aerated at 160 RPM, overnight at 28° C. The cells were harvested and rinsed 2 times with sterile phosphate-buffered saline (PBS) and then resuspended into 200 mL of fresh LB media. Half of the flasks were given a 10 mM final concentration of $HNaSeO_3$, the other half an equivalent amount of media as control. The cultures were shaken at 160 RPM at 28 °C and samples were collected 6, 9, and 12 hours post Se inoculation. They were high pressure frozen using a Wohlwend Compact 02 (Technotrade) high pressure freezer into aluminum planchettes. Samples were freeze-substituted in 0.2% osmium tetroxide, 0.1% uranyl acetate, and 5% water in acetone using the fast-freeze substitution method[186] over 3 hours. Samples were rinsed in acetone and embedded in epon (EMS) over several days. Next, 200 nm sections were cut using an Ultracut UCT (Leica) microtome with a diamond knife (Diatome) and placed on formvar-coated copper slot grids. Sections were post-stained with 2% aqueous uranyl acetate and lead citrate. 15 nm gold fiducials were added. Dual-axis tilt-series were acquired using SerialEM[112] on a Tecnai TF20 (FEI) transmission electron microscope from +/-60, 1 degree intervals on an Ultrascan digital camera (Gatan) at a pixel size of 0.91 nm. Tomogram sections were reconstructed using IMOD.[106] A total of 23 tomogram sections (TS) were collected which are detailed below.

+6 hours control: 3 TS

+6 hours Se: 3 TS

+9 hours control: 3 TS

+9 hours Se: 3 TS

+12 hours control: 3 TS

+12 hours Se: 3 TS

36 hours control, dried: 1 TS

36 hours Se, dried: 1 TS

36 hours Se, resin: 1 TS

Cells harvested at 36 hours post Se inoculation: Cells were grown as previously described in the dry-mount cellular TEM methods. Differences in the procedure were that the cells were grown for 36 hours and the media was changed every 12 hours. Media was exchanged by centrifuging cells at 4,000 rpm at 4 °C for five minutes. The supernatant was poured out and new LB was added and the cells were then resuspended and allowed to continue growing. Cells were fixed at 36 hours as described in the dry-mount cellular TEM methods. Chemically fixed cells were rinsed 2 times in dH20 and then went through a graduated dehydration series into 100% acetone. They were infiltrated with epon (EMS) over several days. 300 nm sections were cut using an Ultracut UCT (Leica) microtome with a diamond knife (Diatome) and placed on formvar-coated copper slot grids. Samples did not undergo post-stain. 10 nm fiducials were added. Single-axis tilt-series were acquired using SerialEM4 on a Tecnai TF30 (FEI) transmission electron microscope from +/-

60, 1 degree intervals on an Ultrascan digital camera (Gatan) at a pixel size of 1.02 nm. Tomograms were reconstructed and modeled using IMOD.[106]

Segmentation. Reconstructions were sectioned using IMOD.[106] The outer cell walls were segmented every 5 tomographic slices on the XY plane. An isosurface was generated and the threshold lowered to determine a cutoff value for imodauto to differentiate cellular background from SeNP. Imodauto was set at a threshold of 1 (out of 255), which generated a model with both the gold fiducials and the SeNPs. The models were merged and the outline of the cell was meshed to generate the image.

Native Polyacrylamide Gels. Native polyacrylamide gels were used to check for selenite reduction capabilities utilizing the procedure described by Hunter.[145] Briefly, cell lysate was purified via HIC column then separated on a 8% non-denaturing polyacrylamide electrophoresis gel (Invitrogen, Carlsbad, CA) using a Novex® Tris-Glycine Native Running Buffer (Invitrogen). Following electrophoresis, gels were placed into zip-lock bags filled with Ar and assayed for selenite reduction capability. Assay was performed by incubation of the gel in a solution of 50 mM HEPES (pH 7.5), 200 mM Na2SeO3 and 1mM NADPH. Bands that turned red were excised for further study.

Protein MS/MS

SDS-PAGE and In-Gel Trypsin Digestion for LC-MS/MS: Bands of interest were excised from the gel and processed for in-gel trypsin digestion and LC-MS/MS as previously described.[187] Briefly, the gel pieces were washed with 200 µL of LC-MS Grade Water (Optima LC-MS, Fisher Scientific) for 30s and destained with 2 x 200 µL of 50% Acetonitrile (ACN; Optima LC-MS Grade)/50 mM ammonium bicarbonate at 60oC, with intermittent mixing. The pieces were dehydrated with

100% ACN and dried via vacuum centrifugation in a SpeedVac for 5 min. Proteins were reduced and alkylated, in-gel with 25 mM DTT in 50 mM ammonium bicarbonate (60°C for 20 min) and 55 mM IAA in 50 mM ammonium bicarbonate at room temperature in the dark for 20 min. Gel pieces were then washed with Optima water and dried. The dried gel pieces were rehydrated in 20 µL 12 ng/µL MS-grade Trypsin (ThermoPierce, San Jose, CA) /0.01% ProteaseMAX surfactant/50 mM ammonium bicarbonate mixture for 10 min at room temperature, overlaid with 30 µL 0.01% ProteaseMAX surfactant/50 mM ammonium bicarbonate and incubated at 50 °C for 1 h. Extracted peptides were transferred and the digestion halted by addition of 10% trifluoro-acetic acid to a final concentration of 0.5%. Peptide extracts were dehydrated and stored at −20 °C prior to analysis by LC-MS/MS.

Peptides were purified and concentrated using an on-line enrichment column (Thermo Scientific 5 mm, 100 mm ID x 2 cm C18 column). Subsequent chromatographic separation was performed on a reverse phase nanospray column (Thermo Scientific EASYnano-LC, 3 mm, 75 mm ID x 100 mm C18 column) using a 30 minute linear gradient from 10%-30% buffer B (100% ACN, 0.1% formic acid) at a flow rate of 400 nanoliters/min. Peptides were eluted directly into the mass spectrometer (Thermo Scientific Orbitrap Velos). The instrument was operated in Orbitrap-LTQ mode where precursor measurements were acquired in the Orbitrap (60,000 resolution) and MS/MS spectra (top 20) were acquired in the LTQ ion trap with a normalized collision energy of 35kV. Mass spectra were collected over a m/z range of 400-2000 Da using a dynamic exclusion limit of 2 MS/MS spectra of a given peptide mass for 30 s (exclusion duration of 90 s). Compound lists of the resulting spectra were generated using Xcalibur 2.2 software (Thermo Scientific) with a S/N threshold of 1.5 and 1 scan/group.

Glutathione Reductase Transmission Electron Microscopy. Glutathione reductase Se nanoparticles were made by mixing 25 µL(66 µg) of glutathione reductase (from S. cerevisiae) with 500 µL 100 mM selenite (HNaSeO3), 100 µL 10mM NADPH and 275 µL 10x PBS (pH 7.4). The solution was allowed to mix for an hour, at which point the solution turned red. The samples were centrifuged and the pellet washed with 1x PBS (pH 7.4). Particles were then mounted onto 400 mesh Cu grids with a 50 nm C coating (Electron Microscopy Sciences). TEM images were taken on a JEOL JEM-1400 Transmission Electron Microscope at an accelerating voltage of 100 kV.

Selenite/Tellurite assays. Samples (1 ml) were made using a constant NADPH concentration (0.36 mM) in PBS. Varying selenite/tellurite concentrations were used (1 mM to 1 M). All blanks contained the same content as the reactions except NADPH. 5 µL (13 µg) of glutathione reductase was added to the reaction and A340 measurements were obtained every 2 seconds for the first 10 minutes, every 10 seconds for the next 20 minutes, followed by every minute for the next 30 minutes. The decrease in absorbance at 340 nm was used to analyze the initial reaction rate.

Protein Concentration Assay. Four 315 uL samples were created in 1x PBS, 10mM selenite, and equal amounts of Baker's yeast glutathione reductase from Sigma Aldrich. The samples had varying NADPH concentrations from 0 to 6mM and were allowed to react for approximately 20 hours. Once the reaction was completed the samples were centrifuged at 14000 rpm for 30 minutes to remove any synthesized nanoparticles. The supernatants were collected and a Bradford assay was performed in triplicate on the four samples in a 1:9 ratio of sample to reagent. The nanoparticle pellets were then washed with water two times to remove

any free protein, followed by redispersion of the pellets in .005% SDS. These samples were then run through the assay in the same ratio also in triplicate. Two standard curves were made, one using GSHR in 1x PBS and one using GSHR in .005% SDS.

SDS Gel Assay. 315 uL samples were created in 1x PBS, six in 4mM NADPH and a control with no NADPH. The six samples contained a range of selenite from 0 to 10mM while the control contained no selenite. An equal amount of Baker's yeast glutathione reductase from Sigma Aldrich was added to each sample and allowed to react for approximately 20 hours. The samples were spun down at 14000 rpm for 30 minutes to remove any synthesized nanoparticles. Following this, a 4-15% SDS gel from Bio-Rad was set up with each well containing 25 uL of a solution made from 25uL sample in 5 uL of SDS loading dye (Bio-Rad). The gel was run at 110 V for 75 minutes. After staining with Coomassie Brilliant Blue G-250 followed by de-staining, the gel was imaged with a Bio-Rad GelDoc XR. It should also be noted that another set of samples were created which contained 1/3 of the protein as the SDS samples. Three samples were created under the exact same conditions as stated before apart from the difference in added enzyme. The samples consisted of a control of GSHR in 1x PBS, and two samples containing 4mM NADPH. One of the cofactor samples contained no selenite and the other with a final concentration of 10mM. A 6% native gel was casted and six wells were loaded with 25uL of a solution made from 25uL sample and 5 uL SDS loading dye. The first three wells were filled with samples containing the lowered amount of added enzyme, while the last three wells contained samples with the added enzyme mentioned in the beginning of this section. This gel was run at 110 V for 1 hour and was stained with Coomassie Brilliant Blue G-250 following destaining and imaged with the same Bio-Rad GelDoc XR.

Crystallographic Information File Au_{102}(*p*-MBA)$_{40}$(*p*-BBT)$_4$
Full CIF can be found: http://pubs.acs.org/doi/abs/10.1021/ja3032339

```
data_ch1x4_15_xprep_actual_r14_acta

_audit_creation_method            SHELXL-97
_chemical_name_systematic
;
 ?
;
_chemical_name_common             Br_exchanged_Au102
_chemical_melting_point           ?
_chemical_formula_moiety          ?
_chemical_formula_sum
 'C308 H488 Au102 Br O99 S44'
_chemical_formula_weight          27356.12

loop_
 _atom_type_symbol
 _atom_type_description
 _atom_type_scat_dispersion_real
 _atom_type_scat_dispersion_imag
 _atom_type_scat_source
 'C'  'C'   0.0033   0.0000
 'International Tables Vol C Tables 4.2.6.8 and 6.1.1.4'
 'H'  'H'   0.0000   0.0000
 'International Tables Vol C Tables 4.2.6.8 and 6.1.1.4'
 'O'  'O'   0.0106   0.0000
 'International Tables Vol C Tables 4.2.6.8 and 6.1.1.4'
 'S'  'S'   0.1246   0.0000
 'International Tables Vol C Tables 4.2.6.8 and 6.1.1.4'
 'Au'  'Au'  -2.0133   0.0000
 'International Tables Vol C Tables 4.2.6.8 and 6.1.1.4'
 'Br'  'Br'  -0.2901   0.0000
 'International Tables Vol C Tables 4.2.6.8 and 6.1.1.4'

_symmetry_cell_setting            Monoclinic
_symmetry_space_group_name_H-M    C2/c

loop_
 _symmetry_equiv_pos_as_xyz
 'x, y, z'
 '-x, y, -z+1/2'
 'x+1/2, y+1/2, z'
 '-x+1/2, y+1/2, -z+1/2'
 '-x, -y, -z'
```

```
 'x, -y, z-1/2'
 '-x+1/2, -y+1/2, -z'
 'x+1/2, -y+1/2, z-1/2'

_cell_length_a                    30.300(6)
_cell_length_b                    57.100(11)
_cell_length_c                    38.200(8)
_cell_angle_alpha                 90.00
_cell_angle_beta                  109.30(3)
_cell_angle_gamma                 90.00
_cell_volume                      62377(22)
_cell_formula_units_Z             4
_cell_measurement_temperature     100(2)
_cell_measurement_reflns_used     2
_cell_measurement_theta_min       0
_cell_measurement_theta_max       90

_exptl_crystal_description        Rod-like
_exptl_crystal_colour             Black
_exptl_crystal_size_max           .05
_exptl_crystal_size_mid           .01
_exptl_crystal_size_min           .01
_exptl_crystal_density_meas       ?
_exptl_crystal_density_diffrn     2.913
_exptl_crystal_density_method     'not measured'
_exptl_crystal_F_000              47700
_exptl_absorpt_coefficient_mu     24.134
_exptl_absorpt_correction_type    ?
_exptl_absorpt_correction_T_min   ?
_exptl_absorpt_correction_T_max   ?
_exptl_absorpt_process_details    ?

_exptl_special_details
;
 ?
;

_diffrn_ambient_temperature       100(2)
_diffrn_radiation_wavelength      0.82700
_diffrn_radiation_type            Synchrotron
_diffrn_radiation_source          'fine-focus sealed tube'
_diffrn_radiation_monochromator   Rosenbaum-Rock_Si(111)
_diffrn_measurement_device_type   NOIR-1_MBC
_diffrn_measurement_method        omega/2theta
_diffrn_detector_area_resol_mean  165.76
_diffrn_standards_number          N/A
_diffrn_standards_interval_count  N/A
_diffrn_standards_interval_time   N/A
_diffrn_standards_decay_%         N/A
_diffrn_reflns_number             35852
_diffrn_reflns_av_R_equivalents   0.1267
_diffrn_reflns_av_sigmaI/netI     0.0976
```

```
_diffrn_reflns_limit_h_min        -20
_diffrn_reflns_limit_h_max        20
_diffrn_reflns_limit_k_min        -36
_diffrn_reflns_limit_k_max        38
_diffrn_reflns_limit_l_min        -25
_diffrn_reflns_limit_l_max        25
_diffrn_reflns_theta_min          1.28
_diffrn_reflns_theta_max          16.00
_reflns_number_total              9650
_reflns_number_gt                 5512
_reflns_threshold_expression      >2sigma(I)

_computing_data_collection        ?
_computing_cell_refinement        ?
_computing_data_reduction         ?
_computing_structure_solution     'SHELXS-97 (Sheldrick, 1990)'
_computing_structure_refinement   'SHELXL-97 (Sheldrick, 1997)'
_computing_molecular_graphics     ?
_computing_publication_material   ?

_refine_special_details
;
 Refinement of F^2^ against ALL reflections.  The weighted R-factor wR
and
 goodness of fit S are based on F^2^, conventional R-factors R are
based
 on F, with F set to zero for negative F^2^. The threshold expression
of
 F^2^ > 2sigma(F^2^) is used only for calculating R-factors(gt) etc.
and is
 not relevant to the choice of reflections for refinement.  R-factors
based
 on F^2^ are statistically about twice as large as those based on F,
and R-
 factors based on ALL data will be even larger.
;

_refine_ls_structure_factor_coef  Fsqd
_refine_ls_matrix_type            full
_refine_ls_weighting_scheme       calc
_refine_ls_weighting_details
 'calc w=1/[\s^2^(Fo^2^)+(0.2000P)^2^+0.1000P] where
P=(Fo^2^+2Fc^2^)/3'
_atom_sites_solution_primary      direct
_atom_sites_solution_secondary    difmap
_atom_sites_solution_hydrogens    geom
_refine_ls_hydrogen_treatment     mixed
_refine_ls_extinction_method      none
_refine_ls_extinction_coef        ?
_refine_ls_number_reflns          9650
_refine_ls_number_parameters      1473
_refine_ls_number_restraints      9537
```

```
_refine_ls_R_factor_all          0.1472
_refine_ls_R_factor_gt           0.0840
_refine_ls_wR_factor_ref         0.3042
_refine_ls_wR_factor_gt          0.2596
_refine_ls_goodness_of_fit_ref   1.080
_refine_ls_restrained_S_all      0.745
_refine_ls_shift/su_max          1.707
_refine_ls_shift/su_mean         0.002
```

CIF $Au_{25}(PET)_{16}(p\text{-}BBT)_2$

Full CIF can be found at http://pubs.acs.org/doi/abs/10.1021/ic5010819

```
data_XPREP_2-3_1_r37

_audit_creation_method           SHELXL-2013
_chemical_name_systematic
?
_chemical_name_common            ?
_chemical_melting_point          ?
_chemical_formula_moiety
 'C140 Au25 S18 Br2'
_chemical_formula_sum
 'C154 Au25 Br2 S18'
_chemical_formula_weight         7510.60

loop_
 _atom_type_symbol
 _atom_type_description
 _atom_type_scat_dispersion_real
 _atom_type_scat_dispersion_imag
 _atom_type_scat_source
 'C'  'C'   0.0033   0.0016
 'International Tables Vol C Tables 4.2.6.8 and 6.1.1.4'
 'S'  'S'   0.1900   0.2300
 'International Tables Vol C Tables 4.2.6.8 and 6.1.1.4'
 'Au'  'Au'  -8.5800   9.1800
 'International Tables Vol C Tables 4.2.6.8 and 6.1.1.4'
 'Br'  'Br'  -0.2901   2.4595
 'International Tables Vol C Tables 4.2.6.8 and 6.1.1.4'

_space_group_crystal_system      triclinic
_space_group_IT_number           2
_space_group_name_H-M_alt        'P -1'
_space_group_name_Hall           '-P 1'

_shelx_space_group_comment
;
The symmetry employed for this shelxl refinement is uniquely defined
by the following loop, which should always be used as a source of
symmetry information in preference to the above space-group names.
```

```
They are only intended as comments.
;

loop_
 _space_group_symop_operation_xyz
 'x, y, z'
 '-x, -y, -z'

_cell_length_a                    15.971(3)
_cell_length_b                    17.565(4)
_cell_length_c                    17.879(4)
_cell_angle_alpha                 65.34(3)
_cell_angle_beta                  65.20(3)
_cell_angle_gamma                 81.89(3)
_cell_volume                      4134.3(19)
_cell_formula_units_Z             1
_cell_measurement_temperature     77(2)
_cell_measurement_reflns_used     6250
_cell_measurement_theta_min       0
_cell_measurement_theta_max       90

_exptl_crystal_description        square
_exptl_crystal_colour             black
_exptl_crystal_density_meas       ?
_exptl_crystal_density_method     ?
_exptl_crystal_density_diffrn     3.017
_exptl_crystal_F_000              3257
_exptl_transmission_factor_min    ?
_exptl_transmission_factor_max    ?
_exptl_crystal_size_max           ?
_exptl_crystal_size_mid           ?
_exptl_crystal_size_min           ?
_exptl_absorpt_coefficient_mu     22.830
_shelx_estimated_absorpt_T_min    ?
_shelx_estimated_absorpt_T_max    ?
_exptl_absorpt_correction_type    ?
_exptl_absorpt_correction_T_min   ?
_exptl_absorpt_correction_T_max   ?
_exptl_absorpt_process_details    ?

_exptl_special_details
?

_diffrn_ambient_temperature       77(2)
_diffrn_radiation_wavelength      0.918
_diffrn_radiation_type            synchrotron
_diffrn_source                    synchrotron
_diffrn_measurement_device_type   ?
_diffrn_measurement_method        ?
_diffrn_detector_area_resol_mean  ?
_diffrn_reflns_number             6123
_diffrn_reflns_av_unetI/netI      0.1053
```

```
_diffrn_reflns_av_R_equivalents   0.0693
_diffrn_reflns_limit_h_min        -11
_diffrn_reflns_limit_h_max        11
_diffrn_reflns_limit_k_min        -12
_diffrn_reflns_limit_k_max        12
_diffrn_reflns_limit_l_min        -13
_diffrn_reflns_limit_l_max        13
_diffrn_reflns_theta_min          1.649
_diffrn_reflns_theta_max          20.019
_diffrn_reflns_theta_full         33.422
_diffrn_measured_fraction_theta_max   0.893
_diffrn_measured_fraction_theta_full  0.214
_diffrn_reflns_Laue_measured_fraction_max    0.893
_diffrn_reflns_Laue_measured_fraction_full   0.214
_diffrn_reflns_point_group_measured_fraction_max   0.893
_diffrn_reflns_point_group_measured_fraction_full  0.214
_reflns_number_total              3044
_reflns_number_gt                 2902
_reflns_threshold_expression      'I > 2\s(I)'
_reflns_Friedel_coverage          0.000
_reflns_Friedel_fraction_max      .
_reflns_Friedel_fraction_full     .

_reflns_special_details
;
 Reflections were merged by SHELXL according to the crystal
 class for the calculation of statistics and refinement.

 _reflns_Friedel_fraction is defined as the number of unique
 Friedel pairs measured divided by the number that would be
 possible theoretically, ignoring centric projections and
 systematic absences.
;

_computing_data_collection        ?
_computing_cell_refinement        ?
_computing_data_reduction         XDS
_computing_structure_solution     SHELXTL
_computing_structure_refinement   'SHELXL-2013 (Sheldrick, 2013)'
_computing_molecular_graphics     ?
_computing_publication_material   ?

_refine_special_details
?
_refine_ls_structure_factor_coef  Fsqd
_refine_ls_matrix_type            full
_refine_ls_weighting_scheme       calc
_refine_ls_weighting_details
'w=1/[\s^2^(Fo^2^)+(0.1236P)^2^+133.6728P] where P=(Fo^2^+2Fc^2^)/3'
_atom_sites_solution_primary      ?
_atom_sites_solution_secondary    ?
_atom_sites_solution_hydrogens    .
```

```
_refine_ls_hydrogen_treatment     undef
_refine_ls_extinction_method      none
_refine_ls_extinction_coef        .
_refine_ls_number_reflns          3044
_refine_ls_number_parameters      922
_refine_ls_number_restraints      1815
_refine_ls_R_factor_all           0.0706
_refine_ls_R_factor_gt            0.0693
_refine_ls_wR_factor_ref          0.1902
_refine_ls_wR_factor_gt           0.1887
_refine_ls_goodness_of_fit_ref    1.114
_refine_ls_restrained_S_all       0.900
_refine_ls_shift/su_max           3.098
_refine_ls_shift/su_mean          0.081
```

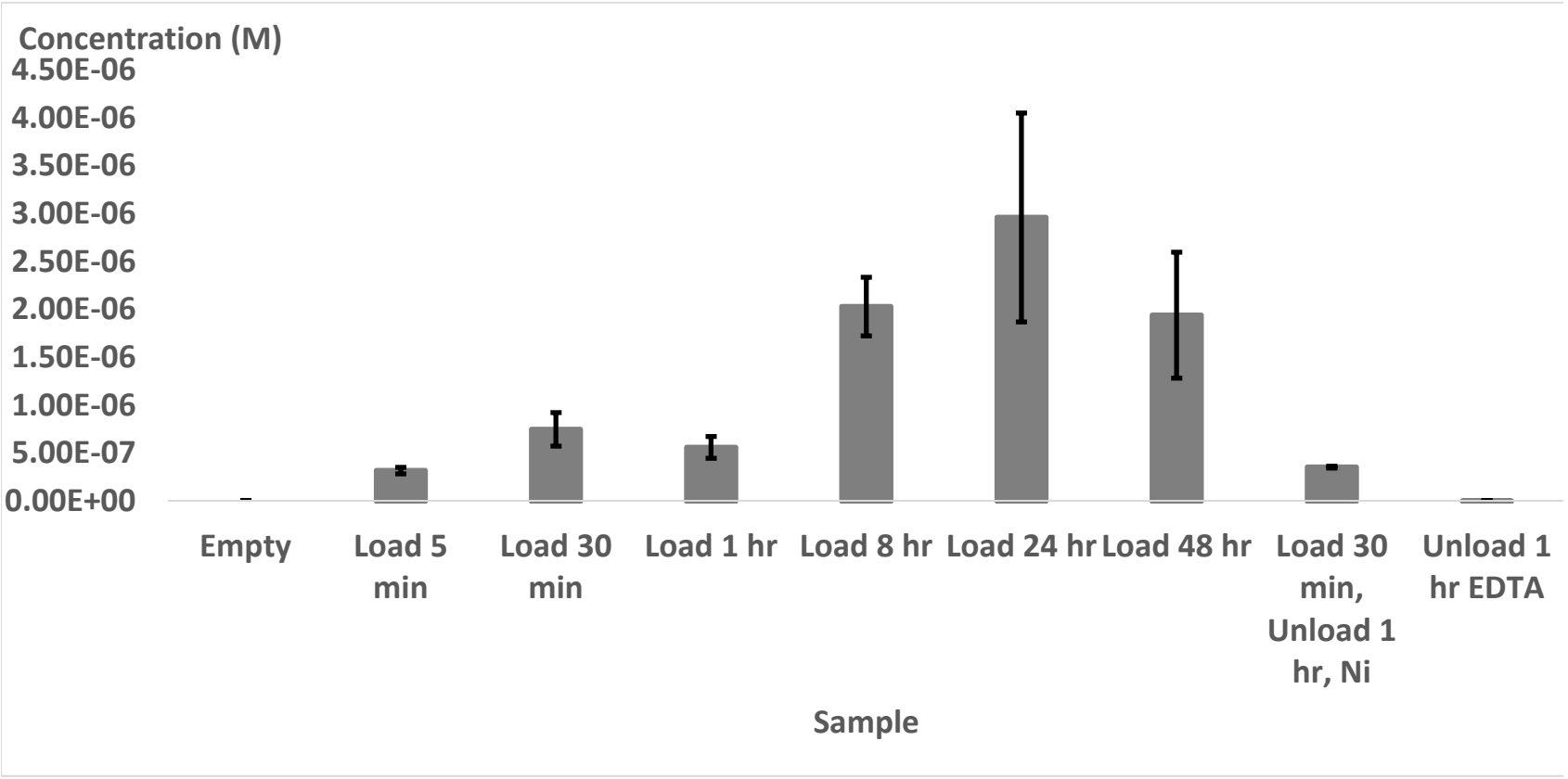

Figure 4.1. Concentration of gold found in protein crystals under different conditions.

Table 4.1. Table of Proteins Identified from HIC and MALDI-MS

Identified Proteins (113)	Accession Number	Molecular Weight	# Unique Peptides					Percent Coverage				
			A	B	C	D	E	A	B	C	D	E
Ferritin and Dps [Pseudomonas fluorescens Pf0-1]	gi|77460635	18 kDa	4	2	10	4	9	32%	13%	74%	32%	59%
4-aminobutyrate aminotransferase [Pseudomonas fluorescens Pf0-1]	gi|77456416	45 kDa	2	23	10	18	5	8.70%	72%	37%	59%	24%
arginine deiminase [Pseudomonas fluorescens Pf0-1]	gi|77460607	46 kDa	4	15	5	15	3	14%	38%	22%	39%	12%
electron transfer flavoprotein subunit beta [Pseudomonas syringae pv. Syringae B728a]	gi|66045414 (+1)	26 kDa	7	8	4	13	2	39%	36%	29%	61%	18%
GMP synthase [Pseudomonas fluorescens Pf0-1]	gi|77460808	58 kDa	0	16	3	14	2	0	43%	10%	42%	8.20%
serine hydroxymethyltransferase [Pseudomonas protegens Pf-5]	gi|70732651	45 kDa	0	6	2	11	2	0	17%	8.40%	32%	8.40%
electron transfer flavoprotein subunit alpha and beta [Pseudomonas fluorescens Pf0-1]	gi|77460337	31 kDa	0	7	2	8	0	0	39%	11%	42%	0
glutaminyl-tRNA synthetase [Pseudomonas fluorescens Pf0-1]	gi|77459861	65 kDa	0	9	0	6	0	0	19%	0	15%	0
phosphoenolpyruvate carboxykinase [Pseudomonas fluorescens Pf0-1]	gi|77456496	55 kDa	0	10	4	15	0	0	27%	11%	35%	0

isocitrate dehydrogenase [Pseudomonas fluorescens SBW25]	gi|229591243	45 kDa	0	13	2	5	0	0	33%	5.70%	17%	0
phosphopyruvate hydratase [Pseudomonas fluorescens Pf0-1]	gi|77457348	46 kDa	3	5	5	11	2	14%	19%	25%	43%	11%
elongation factor Tu [Pseudomonas putida KT2440]	gi|26987193	43 kDa	2	5	0	0	0	7.80%	17%	0	0	0
phosphoglycerate kinase [Pseudomonas fluorescens Pf0-1]	gi|77461486	40 kDa	0	4	0	9	0	0	14%	0	30%	0
tryptophan 2-monooxygenase [Pseudomonas fluorescens Pf0-1]	gi|77461375	62 kDa	0	4	0	4	0	0	11%	0	11%	0
acetyl-CoA synthetase [Pseudomonas fluorescens Pf0-1]	gi|77461035	72 kDa	0	6	0	6	0	0	13%	0	13%	0
thiol peroxidase (atypical 2-Cys peroxiredoxin) [Pseudomonas fluorescens Pf0-1]	gi|77458745	18 kDa	0	5	0	6	0	0	51%	0	64%	0
aminotransferase [Pseudomonas fluorescens Pf0-1]	gi|77461627	50 kDa	0	2	0	6	0	0	6.20%	0	23%	0
nucleoside diphosphate kinase [Pseudomonas putida KT2440]	gi|26987585 (+1)	15 kDa	3	0	0	2	0	34%	0	0	25%	0
NADH:99lavin oxidoreductase/NADH oxidase [Pseudomonas fluorescens Pf0-1]	gi|77457509	38 kDa	0	0	0	0	3	0	0	0	0	12%
anthranilate phosphoribosyltransferase [Pseudomonas fluorescens Pf0-1]	gi|77461335	37 kDa	0	0	0	6	2	0	0	0	31%	12%

glycerol kinase [Pseudomonas fluorescens Pf0-1]	gi|77460753	56 kDa	0	9	0	0	0	0	27%	0	0	0
ornithine carbamoyltransferase [Pseudomonas fluorescens Pf0-1]	gi|77460608	38 kDa	3	0	0	0	0	15%	0	0	0	0
fumarylacetoacetate hydrolase [Pseudomonas fluorescens Pf0-1]	gi|77457138	47 kDa	0	3	0	4	0	0	7.10%	0	9.70%	0
elongation factor G [Pseudomonas fluorescens Pf0-1]	gi|77461303	77 kDa	0	7	0	0	0	0	14%	0	0	0
glutathione reductase [Pseudomonas fluorescens Pf0-1]	gi|77459153	49 kDa	0	6	0	3	0	0	20%	0	8.80%	0
fumarase [Pseudomonas fluorescens Pf0-1]	gi|77460673	55 kDa	0	2	0	3	0	0	7.30%	0	14%	0
50S ribosomal protein L15 [Pseudomonas fluorescens Pf0-1]	gi|77461281	15 kDa	0	3	0	3	0	0	30%	0	30%	0
glutamate-1-semialdehyde aminotransferase [Pseudomonas fluorescens Pf0-1]	gi|77461168	45 kDa	0	0	0	0	5	0	0	0	0	22%
GMP synthase [Pseudomonas protegens Pf-5]	gi|70732263	58 kDa	0	3	0	2	0	0	42%	0	37%	0
fumarylacetoacetate (FAA) hydrolase [Pseudomonas fluorescens Pf0-1]	gi|77461606	24 kDa	0	0	0	2	0	0	0	0	17%	0
FAD dependent oxidoreductase [Pseudomonas fluorescens Pf0-1]	gi|77460953	36 kDa	0	0	2	2	2	0	0	8.80%	8.80%	8.80%

UDP-glucose pyrophosphorylase [Pseudomonas fluorescens]	gi|238069189	31 kDa	0	0	0	5	0	0	0	0	42%	0
nitrite and sulfite reductase 4Fe-4S region [Pseudomonas fluorescens Pf0-1]	gi|77459334	62 kDa	0	2	0	0	0	0	3.60%	0	0	0
ribosomal subunit interface protein [Pseudomonas fluorescens Pf0-1]	gi|77457149	15 kDa	0	0	2	0	0	0	0	21%	0	0
glutathione S-transferase-like protein [Pseudomonas fluorescens Pf0-1]	gi|77460647	23 kDa	0	2	0	3	0	0	11%	0	15%	0
2-dehydro-3-deoxyphosphooctonate aldolase [Pseudomonas fluorescens Pf0-1]	gi|77457347	31 kDa	0	0	0	2	0	0	0	0	9.30%	0
branched-chain amino acid aminotransferase [Pseudomonas fluorescens Pf0-1]	gi|77459689	37 kDa	0	2	0	0	0	0	9.40%	0	0	0
indole-3-glycerol-phosphate synthase [Pseudomonas fluorescens Pf0-1]	gi|77461334	30 kDa	2	0	0	0	2	8.30%	0	0	0	10%
acyl-CoA dehydrogenase [Pseudomonas fluorescens Pf0-1]	gi|77459092	41 kDa	0	4	0	0	0	0	18%	0	0	0
hypothetical protein PFL_0947 [Pseudomonas protegens Pf-5]	gi|70728329	11 kDa	0	0	0	0	2	0	0	0	0	26%
glutaminyl-tRNA synthetase [Pseudomonas protegens Pf-5]	gi|70731272	65 kDa	0	2	0	2	0	0	22%	0	19%	0

TatD-like deoxyribonuclease [Pseudomonas fluorescens Pf0-1]	gi|77460370	29 kDa	3	0	0	0	0	20%	0	0	0	0
translation initiation factor IF-3 [Pseudomonas fluorescens Pf0-1]	gi|77458159	20 kDa	0	2	0	0	0	0	18%	0	0	0
30S ribosomal protein S6 [Pseudomonas mendocina ymp]	gi|146305680 (+3)	16 kDa	0	0	0	0	3	0	0	0	0	25%
5,10-methylenetetrahydrofolate reductase [Pseudomonas fluorescens Pf0-1]	gi|77461502	32 kDa	0	3	0	3	0	0	13%	0	12%	0
acetyl-CoA synthetase [Pseudomonas fluorescens SBW25]	gi|229592627	71 kDa	0	2	0	0	0	0	10%	0	0	0
isopropylmalate isomerase small subunit [Pseudomonas fluorescens SBW25]	gi|229591624	24 kDa	3	0	0	0	0	15%	0	0	0	0
bifunctional aconitate hydratase 2/2-methylisocitrate dehydratase [Pseudomonas fluorescens Pf0-1]	gi|255961273 (+1)	95 kDa	0	0	0	2	0	0	0	0	3.20%	0
3-ketoacyl-ACP reductase [Pseudomonas fluorescens Pf0-1]	gi|77460378	26 kDa	2	0	0	0	0	12%	0	0	0	0
urocanate hydratase [Pseudomonas fluorescens SBW25]	gi|229587922	61 kDa	0	0	0	4	0	0	0	0	9.50%	0
hydroxymethylglutaryl-CoA lyase [Pseudomonas fluorescens Pf0-1]	gi|77459876	31 kDa	3	0	0	0	0	13%	0	0	0	0

imidazole glycerol phosphate synthase subunit HisH [Pseudomonas fluorescens Pf0-1]	gi|77456552	23 kDa	2	0	0	0	0	9.00%	0	0	0	0
N-formylglutamate deformylase [Pseudomonas fluorescens Pf0-1]	gi|77456596	30 kDa	2	0	0	0	0	7.90%	0	0	0	0
glycine cleavage T protein [Pseudomonas fluorescens Pf0-1]	gi|77457584	34 kDa	0	2	0	0	0	0	3.80%	0	0	0
hypothetical protein Pfl01_4410 [Pseudomonas fluorescens Pf0-1]	gi|77460631	27 kDa	0	0	2	0	2	0	0	11%	0	11%
6-phosphogluconolactonase [Pseudomonas fluorescens Pf0-1]	gi|77460583	25 kDa	0	2	0	0	0	0	11%	0	0	0
transcriptional repressor for ferric uptake [Pseudomonas entomophila L48]	gi|104780009 (+4)	15 kDa	2	0	0	0	0	18%	0	0	0	0
phosphoribosylamine—glycine ligase [Pseudomonas syringae pv. Syringae B728a]	gi|66047634	46 kDa	4	0	0	0	0	13%	0	0	0	0
ACP S-malonyltransferase [Pseudomonas fluorescens Pf0-1]	gi|77460379	32 kDa	2	0	0	0	0	10%	0	0	0	0
histidyl-tRNA synthetase [Pseudomonas fluorescens Pf0-1]	gi|77460821	48 kDa	0	2	0	0	0	0	6.50%	0	0	0
3-isopropylmalate dehydrogenase [Pseudomonas fluorescens Pf0-1]	gi|77458119	39 kDa	0	0	0	3	0	0	0	0	10.00%	0
putative ornithine decarboxylase [Pseudomonas fluorescens SBW25]	gi|229588356	44 kDa	0	0	0	2	0	0	0	0	6.70%	0

glycerol kinase [Pseudomonas fluorescens SBW25]	gi|229588682 (+1)	56 kDa	0	2	0	0	0	0	28%	0	0	0
scaffold protein [Pseudomonas fluorescens Pf0-1]	gi|77460832	14 kDa	2	0	0	0	0	27%	0	0	0	0
DNA polymerase III subunit beta [Pseudomonas fluorescens Pf0-1]	gi|77456230	40 kDa	0	0	0	2	0	0	0	0	7.60%	0
END OF FILE												

CHAPTER 5. REFERENCES

(1) Austrian, R. *Bacteriol. Rev.* **1960**, *24* (3), 261.
(2) Latt, S. A.; Stetten, G.; Juergens, L. A.; Willard, H. F.; Scher, C. D. *J. Histochem. Cytochem.* **1975**, *23* (7), 493.
(3) Latt, S. A.; Stetten, G. *J. Histochem. Cytochem.* **1976**, *24* (1), 24.
(4) Lipscomb, E. A.; Sarmiere, P. D.; Freeman, R. S. *J. Biol. Chem.* **2001**, *276* (7), 5085.
(5) Phillips, G. J. *FEMS Microbiol. Lett.* **2001**, *204* (1), 9.
(6) Tsien, R. Y. *Annu. Rev. Biochem.* **1998**, *67* (1), 509.
(7) Lakadamyali, M.; Rust, M. J.; Babcock, H. P.; Zhuang, X. *Proc. Natl. Acad. Sci.* **2003**, *100* (16), 9280.
(8) Kouros-Mehr, H.; Bechis, S. K.; Slorach, E. M.; Littlepage, L. E.; Egeblad, M.; Ewald, A. J.; Pai, S.-Y.; Ho, I.-C.; Werb, Z. *Cancer Cell* **2008**, *13* (2), 141.
(9) Fakhrudin, N.; Ladurner, A.; Atanasov, A. G.; Heiss, E. H.; Baumgartner, L.; Markt, P.; Schuster, D.; Ellmerer, E. P.; Wolber, G.; Rollinger, J. M.; Stuppner, H.; Dirsch, V. M. *Mol. Pharmacol.* **2010**, *77* (4), 559.
(10) Mastronarde, D. N. *J. Struct. Biol.* **1997**, *120* (3), 343.
(11) Jensen, G. J.; Kornberg, R. D. *Proc. Natl. Acad. Sci.* **1998**, *95* (16), 9262.
(12) Jensen, G. J.; Briegel, A. *Curr. Opin. Struct. Biol.* **2007**, *17* (2), 260.
(13) Azubel, M.; Koivisto, J.; Malola, S.; Bushnell, D.; Hura, G. L.; Koh, A. L.; Tsunoyama, H.; Tsukuda, T.; Pettersson, M.; Häkkinen, H.; Kornberg, R. D. *Science* **2014**, *345* (6199), 909.
(14) Liao, M.; Cao, E.; Julius, D.; Cheng, Y. *Nature* **2013**, *504* (7478), 107.
(15) Bartesaghi, A.; Merk, A.; Banerjee, S.; Matthies, D.; Wu, X.; Milne, J. L. S.; Subramaniam, S. *Science* **2015**.
(16) Horne, R. W.; Wildy, P. *J. Microsc.* **1979**, *117* (1), 103.
(17) Gregori, L.; Hainfeld, J. F.; Simon, M. N.; Goldgaber, D. *J. Biol. Chem.* **1997**, *272* (1), 58.
(18) Hainfeld, J. F.; Furuya, F. R. *J. Histochem. Cytochem.* **1992**, *40* (2), 177.
(19) Takizawa, T.; Robinson, J. M. *J. Histochem. Cytochem.* **1994**, *42* (12), 1615.
(20) Tschopp, J.; Podack, E. R.; Müller-Eberhard, H. J. *Proc. Natl. Acad. Sci.* **1982**, *79* (23), 7474.
(21) Jadzinsky, P. D.; Calero, G.; Ackerson, C. J.; Bushnell, D. A.; Kornberg, R. D. *Science* **2007**, *318* (5849), 430.
(22) Hostetler, M. J.; Templeton, A. C.; Murray, R. W. *Langmuir* **1999**, *15* (11), 3782.
(23) Guo, R.; Song, Y.; Wang, G.; Murray, R. W. *J. Am. Chem. Soc.* **2005**, *127* (8), 2752.
(24) Donkers, R. L.; Song, Y.; Murray, R. W. *Langmuir* **2004**, *20* (11), 4703.
(25) Sehgal, D.; Vijay, I. K. *Anal. Biochem.* **1994**, *218* (1), 87.
(26) Du Roure, O.; Debiemme-Chouvy, C.; Malthête, J.; Silberzan, P. *Langmuir* **2003**, *19* (10), 4138.
(27) Ackerson, C. J.; Powell, R. D.; Hainfeld, J. F. *Methods Enzymol.* **2010**, *481*, 195.
(28) Hengen, P. N. *Trends Biochem. Sci.* **1995**, *20* (7), 285.
(29) Zhao, C.; Hellman, L. M.; Zhan, X.; Bowman, W. S.; Whiteheart, S. W.; Fried, M. G. *Anal. Biochem.* **2010**, *399* (2), 237.

(30) Hochuli, E.; Bannwarth, W.; Döbeli, H.; Gentz, R.; Stüber, D. *Nat. Biotechnol.* **1988**, *6* (11), 1321.
(31) Zhu, J.; Waengler, C.; Lennox, R. B.; Schirrmacher, R. *Langmuir* **2012**, *28* (13), 5508.
(32) Schafer, F. Q.; Buettner, G. R. *Free Radic. Biol. Med.* **2001**, *30* (11), 1191.
(33) DeRosier, D. In *Methods in Enzymology*; Elsevier, 2010; Vol. 481, pp 1–24.
(34) He, Y.; Jensen, G. J.; Bjorkman, P. J. *Microsc. Microanal.* **2009**, *15* (03), 183.
(35) Wang, Q.; Mercogliano, C. P.; Löwe, J. *Structure* **2011**, *19* (2), 147.
(36) Xie, J.; Zheng, Y.; Ying, J. Y. *J. Am. Chem. Soc.* **2009**, *131* (3), 888.
(37) Carter, C. J.; Ackerson, C. J.; Feldheim, D. L. *ACS Nano* **2010**, *4* (7), 3883.
(38) Mercogliano, C. P.; DeRosier, D. J. *J. Struct. Biol.* **2007**, *160* (1), 70.
(39) Nishino, Y.; Yasunaga, T.; Miyazawa, A. *J. Electron Microsc. (Tokyo)* **2007**, *56* (3), 93.
(40) Morphew, M. K.; O'Toole, E. T.; Page, C. L.; Pagratis, M.; Meehl, J.; Giddings, T.; Gardner, J. M.; Ackerson, C.; Jaspersen, S. L.; Winey, M.; Hoenger, A.; Mcintosh, J. R. *J. Microsc.* **2015**, n/a.
(41) Shu, X.; Lev-Ram, V.; Deerinck, T. J.; Qi, Y.; Ramko, E. B.; Davidson, M. W.; Jin, Y.; Ellisman, M. H.; Tsien, R. Y. *PLoS Biol* **2011**, *9* (4), e1001041.
(42) Whaley, S. R.; English, D. S.; Hu, E. L.; Barbara, P. F.; Belcher, A. M. *Nature* **2000**, *405* (6787), 665.
(43) Brown, S. *Proc. Natl. Acad. Sci.* **1992**, *89* (18), 8651.
(44) Brown, S. *Nat. Biotechnol.* **1997**, *15* (3), 269.
(45) Naik, R. R.; Jones, S. E.; Murray, C. J.; McAuliffe, J. C.; Vaia, R. A.; Stone, M. O. *Adv. Funct. Mater.* **2004**, *14* (1), 25.
(46) Flynn, C. E.; Mao, C.; Hayhurst, A.; Williams, J. L.; Georgiou, G.; Iverson, B.; Belcher, A. M. *J. Mater. Chem.* **2003**, *13* (10), 2414.
(47) Dickerson, M. B.; Jones, S. E.; Cai, Y.; Ahmad, G.; Naik, R. R.; Kröger, N.; Sandhage, K. H. *Chem. Mater.* **2008**, *20* (4), 1578.
(48) Sano, K.-I.; Shiba, K. *J. Am. Chem. Soc.* **2003**, *125* (47), 14234.
(49) Umetsu, M.; Mizuta, M.; Tsumoto, K.; Ohara, S.; Takami, S.; Watanabe, H.; Kumagai, I.; Adschiri, T. *Adv. Mater.* **2005**, *17* (21), 2571.
(50) Reiss, B. D.; Mao, C.; Solis, D. J.; Ryan, K. S.; Thomson, T.; Belcher, A. M. *Nano Lett.* **2004**, *4* (6), 1127.
(51) Chen, C.-L.; Zhang, P.; Rosi, N. L. *J. Am. Chem. Soc.* **2008**, *130* (41), 13555.
(52) Hwang, L.; Zhao, G.; Zhang, P.; Rosi, N. L. *Small* **2011**, *7* (14), 1939.
(53) Niihori, Y.; Matsuzaki, M.; Pradeep, T.; Negishi, Y. *J. Am. Chem. Soc.* **2013**, *135* (13), 4946.
(54) Niihori, Y.; Kurashige, W.; Matsuzaki, M.; Negishi, Y. *Nanoscale* **2012**, *5* (2), 508.
(55) Shichibu, Y.; Negishi, Y.; Tsukuda, T.; Teranishi, T. *J. Am. Chem. Soc.* **2005**, *127* (39), 13464.
(56) Knoppe, S.; Dharmaratne, A. C.; Schreiner, E.; Dass, A.; Bürgi, T. *J. Am. Chem. Soc.* **2010**, *132* (47), 16783.
(57) Harkness, K. M.; Cliffel, D. E.; McLean, J. A. *Analyst* **2010**, *135* (5), 868.
(58) Woehrle, G. H.; Brown, L. O.; Hutchison, J. E. *J. Am. Chem. Soc.* **2005**, *127* (7), 2172.
(59) Song, Y.; Murray, R. W. *J. Am. Chem. Soc.* **2002**, *124* (24), 7096.
(60) Song, Y.; Huang, T.; Murray, R. W. *J. Am. Chem. Soc.* **2003**, *125* (38), 11694.
(61) Heaven, M. W.; Dass, A.; White, P. S.; Holt, K. M.; Murray, R. W. *J. Am. Chem. Soc.* **2008**, *130* (12), 3754.

(62) Dass, A.; Theivendran, S.; Nimmala, P. R.; Kumara, C.; Jupally, V. R.; Fortunelli, A.; Sementa, L.; Barcaro, G.; Zuo, X.; Noll, B. C. *J. Am. Chem. Soc.* **2015**, *137* (14), 4610.
(63) Qian, H.; Eckenhoff, W. T.; Zhu, Y.; Pintauer, T.; Jin, R. *J. Am. Chem. Soc.* **2010**, *132* (24), 8280.
(64) Yang, S.; Chai, J.; Song, Y.; Kang, X.; Sheng, H.; Chong, H.; Zhu, M. *J. Am. Chem. Soc.* **2015**, *137* (32), 10033.
(65) Nimmala, P. R.; Knoppe, S.; Jupally, V. R.; Delcamp, J. H.; Aikens, C. M.; Dass, A. *J. Phys. Chem. B* **2014**, *118* (49), 14157.
(66) Wong, O. A.; Hansen, R. J.; Ni, T. W.; Heinecke, C. L.; Compel, W. S.; Gustafson, D. L.; Ackerson, C. J. *Nanoscale* **2013**, *5* (21), 10525.
(67) Heinecke, C. L.; Ni, T. W.; Malola, S.; Mäkinen, V.; Wong, O. A.; Häkkinen, H.; Ackerson, C. J. *J. Am. Chem. Soc.* **2012**, *134* (32), 13316.
(68) Ni, T. W.; Tofanelli, M. A.; Phillips, B. D.; Ackerson, C. J. *Inorg. Chem.* **2014**, *53* (13), 6500.
(69) Lee, B.; Richards, F. M. *J. Mol. Biol.* **1971**, *55* (3), 379.
(70) Zhu, M.; Aikens, C. M.; Hollander, F. J.; Schatz, G. C.; Jin, R. *J. Am. Chem. Soc.* **2008**, *130* (18), 5883.
(71) Yoon, B.; Häkkinen, H.; Landman, U. *J. Phys. Chem. A* **2003**, *107* (20), 4066.
(72) Ionita, P.; Caragheorgheopol, A.; Gilbert, B. C.; Chechik, V. *J. Am. Chem. Soc.* **2002**, *124* (31), 9048.
(73) Lucarini, M.; Franchi, P.; Pedulli, G. F.; Pengo, P.; Scrimin, P.; Pasquato, L. *J. Am. Chem. Soc.* **2004**, *126* (30), 9326.
(74) Wong, O. A.; Heinecke, C. L.; Simone, A. R.; Whetten, R. L.; Ackerson, C. J. *Nanoscale* **2012**, *4* (14), 4099.
(75) DeVries, G. A.; Brunnbauer, M.; Hu, Y.; Jackson, A. M.; Long, B.; Neltner, B. T.; Uzun, O.; Wunsch, B. H.; Stellacci, F. *Science* **2007**, *315* (5810), 358.
(76) Rapino, S.; Zerbetto, F. *Small* **2007**, *3* (3), 386.
(77) Song, Y.; Wang, S.; Zhang, J.; Kang, X.; Chen, S.; Li, P.; Sheng, H.; Zhu, M. *J. Am. Chem. Soc.* **2014**, *136* (8), 2963.
(78) Song, Y.; Zhong, J.; Yang, S.; Wang, S.; Cao, T.; Zhang, J.; Li, P.; Hu, D.; Pei, Y.; Zhu, M. *Nanoscale* **2014**, *6* (22), 13977.
(79) Dainese, T.; Antonello, S.; Gascón, J. A.; Pan, F.; Perera, N. V.; Ruzzi, M.; Venzo, A.; Zoleo, A.; Rissanen, K.; Maran, F. *ACS Nano* **2014**, *8* (4), 3904.
(80) Kabsch, W. *Acta Crystallogr. D Biol. Crystallogr.* **2010**, *66* (Pt 2), 125.
(81) Sheldrick, G. M. *Acta Crystallogr. A* **2008**, *64* (1), 112.
(82) Delano, W. The PyMOL Molecular Graphics System http://www.pymol.org (accessed Nov 8, 2015).
(83) Macrae, C. F.; Edgington, P. R.; McCabe, P.; Pidcock, E.; Shields, G. P.; Taylor, R.; Towler, M.; van de Streek, J. *J. Appl. Crystallogr.* **2006**, *39* (3), 453.
(84) Zhu, M.; Qian, H.; Meng, X.; Jin, S.; Wu, Z.; Jin, R. *Nano Lett.* **2011**, *11* (9), 3963.
(85) Knoppe, S.; Bürgi, T. *Acc. Chem. Res.* **2014**, *47* (4), 1318.
(86) Knoppe, S.; Kothalawala, N.; Jupally, V. R.; Dass, A.; Bürgi, T. *Chem. Commun.* **2012**, *48* (38), 4630.
(87) Tofanelli, M. A.; Ackerson, C. J. *J. Am. Chem. Soc.* **2012**, *134* (41), 16937.
(88) Sakamoto, M.; Tanaka, D.; Teranishi, T. *Chem Sci* **2013**, *4* (2), 824.

(89) Patskovsky, Y.; Ramagopal, U.; Almo, S. C. *Be Publ.* **2005**, null.
(90) Wu, Z.; Jin, R. *Nano Lett.* **2010**, *10* (7), 2568.
(91) Wu, Z.; Suhan, J.; Jin, R. *J. Mater. Chem.* **2009**, *19* (5), 622.
(92) Wu, Z.; Gayathri, C.; Gil, R. R.; Jin, R. *J. Am. Chem. Soc.* **2009**, *131* (18), 6535.
(93) Negishi, Y.; Nobusada, K.; Tsukuda, T. *J. Am. Chem. Soc.* **2005**, *127* (14), 5261.
(94) Negishi, Y.; Takasugi, Y.; Sato, S.; Yao, H.; Kimura, K.; Tsukuda, T. *J. Am. Chem. Soc.* **2004**, *126* (21), 6518.
(95) Shen, C.; Hui, C.; Yang, T.; Xiao, C.; Tian, J.; Bao, L.; Chen, S.; Ding, H.; Gao, H. *Chem. Mater.* **2008**, *20* (22), 6939.
(96) Mock, J. J.; Hill, R. T.; Degiron, A.; Zauscher, S.; Chilkoti, A.; Smith, D. R. *Nano Lett.* **2008**, *8* (8), 2245.
(97) Ghosh, S. K.; Pal, T. *Chem. Rev.* **2007**, *107* (11), 4797.
(98) Rechberger, W.; Hohenau, A.; Leitner, A.; Krenn, J. R.; Lamprecht, B.; Aussenegg, F. R. *Opt. Commun.* **2003**, *220* (1-3), 137.
(99) Bogatyrev, V. A.; Dykman, L. A.; Khlebtsov, B. N.; Khlebtsov, N. G. *Opt. Spectrosc.* **2014**, *96* (1), 128.
(100) Doane, T. L.; Chuang, C.-H.; Hill, R. J.; Burda, C. *Acc. Chem. Res.* **2012**, *45* (3), 317.
(101) Laaksonen, T.; Ahonen, P.; Johans, C.; Kontturi, K. *ChemPhysChem* **2006**, *7* (10), 2143.
(102) Brown, L. O.; Hutchison, J. E. *J. Am. Chem. Soc.* **1999**, *121* (4), 882.
(103) Schneider, C. A.; Rasband, W. S.; Eliceiri, K. W. *Nat. Methods* **2012**, *9* (7), 671.
(104) Park, S.; Hamad-Schifferli, K. *J. Phys. Chem. C* **2008**, *112* (20), 7611.
(105) Stevenson, H. P.; Makhov, A. M.; Calero, M.; Edwards, A. L.; Zeldin, O. B.; Mathews, I. I.; Lin, G.; Barnes, C. O.; Santamaria, H.; Ross, T. M.; Soltis, S. M.; Khosla, C.; Nagarajan, V.; Conway, J. F.; Cohen, A. E.; Calero, G. *Proc. Natl. Acad. Sci.* **2014**, *111* (23), 8470.
(106) Kremer, J. R.; Mastronarde, D. N.; McIntosh, J. R. *J. Struct. Biol.* **1996**, *116* (1), 71.
(107) Tran, N. T.; Powell, D. R.; Dahl, L. F. *Angew. Chem. Int. Ed.* **2000**, *39* (22), 4121.
(108) Mortensen, J. J.; Hansen, L. B.; Jacobsen, K. W. *Phys. Rev. B* **2005**, *71* (3), 035109.
(109) Enkovaara, J.; Rostgaard, C.; Mortensen, J. J.; Chen, J.; Dułak, M.; Ferrighi, L.; Gavnholt, J.; Glinsvad, C.; Haikola, V.; Hansen, H. A.; Kristoffersen, H. H.; Kuisma, M.; Larsen, A. H.; Lehtovaara, L.; Ljungberg, M.; Lopez-Acevedo, O.; Moses, P. G.; J Ojanen; Olsen, T.; Petzold, V.; Romero, N. A.; Stausholm-Møller, J.; Strange, M.; Tritsaris, G. A.; Vanin, M.; Walter, M.; B Hammer; Häkkinen, H.; Madsen, G. K. H.; Nieminen, R. M.; Nørskov, J. K.; Puska, M.; Rantala, T. T.; Schiøtz, J.; Thygesen, K. S.; Jacobsen, K. W. *J. Phys. Condens. Matter* **2010**, *22* (25), 253202.
(110) Perdew, J. P.; Burke, K.; Ernzerhof, M. *Phys. Rev. Lett.* **1996**, *77* (18), 3865.
(111) Zhu, M.; Eckenhoff, W. T.; Pintauer, T.; Jin, R. *J. Phys. Chem. C* **2008**, *112* (37), 14221.
(112) Mastronarde, D. N. *J. Struct. Biol.* **2005**, *152* (1), 36.
(113) Giepmans, B. N. G.; Adams, S. R.; Ellisman, M. H.; Tsien, R. Y. *Science* **2006**, *312* (5771), 217.
(114) Theil, E. C. *Annu. Rev. Biochem.* **1987**, *56* (1), 289.
(115) Mercogliano, C. P.; DeRosier, D. J. *J. Mol. Biol.* **2006**, *355* (2), 211.
(116) Diestra, E.; Fontana, J.; Guichard, P.; Marco, S.; Risco, C. *J. Struct. Biol.* **2009**, *165* (3), 157.
(117) Baksi, A.; Xavier, P. L.; Chaudhari, K.; Goswami, N.; Pal, S. K.; Pradeep, T. *Nanoscale* **2013**, *5* (5), 2009.

(118) Xavier, P. L.; Chaudhari, K.; Baksi, A.; Pradeep, T. *Nano Rev.* **2012**, *3*.
(119) Chaudhari, K.; Xavier, P. L.; Pradeep, T. *ACS Nano* **2011**, *5* (11), 8816.
(120) Ahsan Habib, M. T. *Bull. Chem. Soc. Jpn. - BULL CHEM SOC JPN* **2005**, *78* (2), 262.
(121) Xie, J.; Lee, J. Y.; Wang, D. I. C. *Chem. Mater.* **2007**, *19* (11), 2823.
(122) Turkevich, J.; Stevenson, P. C.; Hillier, J. *Discuss. Faraday Soc.* **1951**, *11* (0), 55.
(123) Frens, G. *Nature* **1973**, *241* (105), 20.
(124) de la Fuente, J. M.; Penadés, S. *Biochim. Biophys. Acta* **2006**, *1760* (4), 636.
(125) Haizhen Huang, X. Y. *Carbohydr. Res.* **2004**, *339* (15), 2627.
(126) Amemiya, Y.; Arakaki, A.; Staniland, S. S.; Tanaka, T.; Matsunaga, T. *Biomaterials* **2007**, *28* (35), 5381.
(127) Kolinko, I.; Lohße, A.; Borg, S.; Raschdorf, O.; Jogler, C.; Tu, Q.; Pósfai, M.; Tompa, É.; Plitzko, J. M.; Brachmann, A.; Wanner, G.; Müller, R.; Zhang, Y.; Schüler, D. *Nat. Nanotechnol.* **2014**, *9* (3), 193.
(128) Richards, C. I.; Choi, S.; Hsiang, J.-C.; Antoku, Y.; Vosch, T.; Bongiorno, A.; Tzeng, Y.-L.; Dickson, R. M. *J. Am. Chem. Soc.* **2008**, *130* (15), 5038.
(129) Guo, W.; Yuan, J.; Dong, Q.; Wang, E. *J. Am. Chem. Soc.* **2010**, *132* (3), 932.
(130) Díez, I.; Ras, R. H. A. *Nanoscale* **2011**, *3* (5), 1963.
(131) Gugliotti, L. A.; Feldheim, D. L.; Eaton, B. E. *Science* **2004**, *304* (5672), 850.
(132) Gugliotti, L. A.; Feldheim, D. L.; Eaton, B. E. *J. Am. Chem. Soc.* **2005**, *127* (50), 17814.
(133) Naik, R. R.; Stringer, S. J.; Agarwal, G.; Jones, S. E.; Stone, M. O. *Nat. Mater.* **2002**, *1* (3), 169.
(134) Slocik, J. M.; Stone, M. O.; Naik, R. R. *Small* **2005**, *1* (11), 1048.
(135) Diamanti, S.; Elsen, A.; Naik, R.; Vaia, R. *J. Phys. Chem. C* **2009**, *113* (23), 9993.
(136) Yu, J.; Becker, M. L.; Carri, G. A. *Langmuir* **2012**, *28* (2), 1408.
(137) Tomczak, M. M.; Slocik, J. M.; Stone, M. O.; Naik, R. R. *Biochem. Soc. Trans.* **2007**, *35* (3), 512.
(138) Chen, C.-L.; Rosi, N. L. *Angew. Chem. Int. Ed.* **2010**, *49* (11), 1924.
(139) Cha, J. N.; Shimizu, K.; Zhou, Y.; Christiansen, S. C.; Chmelka, B. F.; Stucky, G. D.; Morse, D. E. *Proc. Natl. Acad. Sci.* **1999**, *96* (2), 361.
(140) Curnow, P.; Bessette, P. H.; Kisailus, D.; Murr, M. M.; Daugherty, P. S.; Morse, D. E. *J. Am. Chem. Soc.* **2005**, *127* (45), 15749.
(141) Smith, G. P.; Baustian, K. J.; Ackerson, C. J.; Feldheim, D. L. *J. Mater. Chem.* **2009**, *19* (44), 8299.
(142) Scott, D.; Toney, M.; Muzikár, M. *J. Am. Chem. Soc.* **2008**, *130* (3), 865.
(143) Silver, S.; Phung, L. T. *J. Ind. Microbiol. Biotechnol.* **2005**, *32* (11-12), 587.
(144) Lenz, M.; Kolvenbach, B.; Gygax, B.; Moes, S.; Corvini, P. F. X. *Appl. Environ. Microbiol.* **2011**, *77* (13), 4676.
(145) Hunter, W. J. *Curr. Microbiol.* **2014**, *69* (1), 69.
(146) Kessi, J. *Microbiology* **2006**, *152* (3), 731.
(147) Bozzi, M.; Mignogna, G.; Stefanini, S.; Barra, D.; Longhi, C.; Valenti, P.; Chiancone, E. *J. Biol. Chem.* **1997**, *272* (6), 3259.
(148) Kröger, N.; Dickerson, M. B.; Ahmad, G.; Cai, Y.; Haluska, M. S.; Sandhage, K. H.; Poulsen, N.; Sheppard, V. C. *Angew. Chem. Int. Ed.* **2006**, *45* (43), 7239.

(149) Ni, T. W.; Staicu, L. C.; Nemeth, R. S.; Schwartz, C. L.; Crawford, D.; Seligman, J. D.; Hunter, W. J.; Pilon-Smits, E. A. H.; Ackerson, C. J. *Nanoscale* **2015**.
(150) Vayssières, L.; Chanéac, C.; Tronc, E.; Jolivet, J. P. *J. Colloid Interface Sci.* **1998**, *205* (2), 205.
(151) Espinosa, A.; Serrano, A.; Llavona, A.; Jimenez de la Morena, J.; Abuin, M.; Figuerola, A.; Pellegrino, T.; Fernández, J. F.; Garcia-Hernandez, M.; Castro, G. R.; Garcia, M. A. *Meas. Sci. Technol.* **2012**, *23* (1), 015602.
(152) Tan, Y. N.; Lee, J. Y.; Wang, D. I. C. *J. Am. Chem. Soc.* **2010**, *132* (16), 5677.
(153) Korkmaz Zirpel, N.; Arslan, T.; Lee, H. *J. Colloid Interface Sci.* **2015**, *454*, 80.
(154) Coppage, R.; Slocik, J. M.; Sethi, M.; Pacardo, D. B.; Naik, R. R.; Knecht, M. R. *Angew. Chem. Int. Ed.* **2010**, *49* (22), 3767.
(155) Li, Y.; Tang, Z.; Prasad, P. N.; Knecht, M. R.; Swihart, M. T. *Nanoscale* **2014**, *6* (6), 3165.
(156) Carter, C. J.; Dolska, M.; Owczarek, A.; Ackerson, C. J.; Eaton, B. E.; Feldheim, D. L. *J. Mater. Chem.* **2009**, *19* (44), 8320.
(157) Schwertmann, U.; Friedl, J.; Stanjek, H. *J. Colloid Interface Sci.* **1999**, *209* (1), 215.
(158) Arakaki, A.; Masuda, F.; Amemiya, Y.; Tanaka, T.; Matsunaga, T. *J. Colloid Interface Sci.* **2010**, *343* (1), 65.
(159) Tanaka, M.; Mazuyama, E.; Arakaki, A.; Matsunaga, T. *J. Biol. Chem.* **2011**, *286* (8), 6386.
(160) Dumon-Seignovert, L.; Cariot, G.; Vuillard, L. *Protein Expr. Purif.* **2004**, *37* (1), 203.
(161) Staicu, L. c.; Ackerson, C. j.; Cornelis, P.; Ye, L.; Berendsen, R. l.; Hunter, W. j.; Noblitt, S. d.; Henry, C. s.; Cappa, J. j.; Montenieri, R. l.; Wong, A. o.; Musilova, L.; Sura-de Jong, M.; van Hullebusch, E. d.; Lens, P. n. l.; Reynolds, R. j. b.; Pilon-Smits, E. a. h. *J. Appl. Microbiol.* **2015**, *119* (2), 400.
(162) Hunter, W. J.; Manter, D. K. *Curr. Microbiol.* **2010**, *62* (2), 565.
(163) McIntosh, R.; Nicastro, D.; Mastronarde, D. *Trends Cell Biol.* **2005**, *15* (1), 43.
(164) Robinson, C. V.; Sali, A.; Baumeister, W. *Nature* **2007**, *450* (7172), 973.
(165) McDonald, K.; Morphew, M. K. *Microsc. Res. Tech.* **1993**, *24* (6), 465.
(166) Giddings, T. H. *J. Microsc.* **2003**, *212* (Pt 1), 53.
(167) Iancu, C. V.; Tivol, W. F.; Schooler, J. B.; Dias, D. P.; Henderson, G. P.; Murphy, G. E.; Wright, E. R.; Li, Z.; Yu, Z.; Briegel, A.; Gan, L.; He, Y.; Jensen, G. J. *Nat. Protoc.* **2007**, *1* (6), 2813.
(168) Frangakis, A. S.; Böhm, J.; Förster, F.; Nickell, S.; Nicastro, D.; Typke, D.; Hegerl, R.; Baumeister, W. *Proc. Natl. Acad. Sci.* **2002**, *99* (22), 14153.
(169) Nickell, S.; Kofler, C.; Leis, A. P.; Baumeister, W. *Nat. Rev. Mol. Cell Biol.* **2006**, *7* (3), 225.
(170) Komeili, A.; Li, Z.; Newman, D. K.; Jensen, G. J. *Science* **2006**, *311* (5758), 242.
(171) Butler, C. S.; Debieux, C. M.; Dridge, E. J.; Splatt, P.; Wright, M. *Biochem. Soc. Trans.* **2012**, *40* (6), 1239.
(172) Basaglia, M.; Toffanin, A.; Baldan, E.; Bottegal, M.; Shapleigh, J. P.; Casella, S. *FEMS Microbiol. Lett.* **2007**, *269* (1), 124.
(173) Garbisu, C.; Ishii, T.; Leighton, T.; Buchanan, B. B. *Chem. Geol.* **1996**, *132* (1–4), 199.
(174) Jornstedt, M. B.; Kumar, S.; Holmgren, A. Enzymology, B.-M. in, Ed.; Biothiols Part B: Glutathione and Thioredoxin: Thiols in Signal Transduction and Gene Regulation; Academic Press, 1995; Vol. 252, pp 209–219.
(175) Lu, J.; Xie, Y.; Xu, F.; Zhu, L. *J. Mater. Chem.* **2002**, *12* (9), 2755.

(176) Margolin, W. *J. Bacteriol.* **2012**, *194* (23), 6369.
(177) Swulius, M. T.; Jensen, G. J. *J. Bacteriol.* **2012**, *194* (23), 6382.
(178) Corbett, J. D. *Chem. Rev.* **1985**, *85* (5), 383.
(179) Scopigno, T.; Steurer, W.; Yannopoulos, S. N.; Chrissanthopoulos, A.; Krisch, M.; Ruocco, G.; Wagner, T. *Nat. Commun.* **2011**, *2*, 195.
(180) Kumar, S.; Björnstedt, M.; Holmgren, A. *Eur. J. Biochem.* **1992**, *207* (2), 435.
(181) Björnstedt, M.; Kumar, S.; Holmgren, A. *J. Biol. Chem.* **1992**, *267* (12), 8030.
(182) Kakhlon, O.; Cabantchik, Z. I. *Free Radic. Biol. Med.* **2002**, *33* (8), 1037.
(183) Fenton, H. J. H. *J. Chem. Soc. Trans.* **1894**, *65* (0), 899.
(184) Goldstein, S.; Meyerstein, D.; Czapski, G. *Free Radic. Biol. Med.* **1993**, *15* (4), 435.
(185) Hunter, W. J.; Manter, D. K. *Curr. Microbiol.* **2008**, *57* (1), 83.
(186) McDonald, K. L.; Webb, R. I. *J. Microsc.* **2011**, *243* (3), 227.
(187) Saveliev, S. V.; Woodroofe, C. C.; Sabat, G.; Adams, C. M.; Klaubert, D.; Wood, K.; Urh, M. *Anal. Chem.* **2013**, *85* (2), 907.